CHARACTERIZING AND MODELING MAGNETIC FLUX TRANSPORT IN THE SUN'S PHOTOSPHERE AND DETERMINING ITS IMPACT ON THE SUNSPOT CYCLE

By

Lisa A. Upton

Dissertation

Submitted to the Faculty of the

Graduate School of Vanderbilt University

in partial fulfillment of the requirements

for the degree of

DOCTOR OF PHILOSOPHY

in

PHYSICS

May, 2014

Nashville, TN

Approved:

David A. Weintraub, Ph.D.

Kelly Holley-Bockelmann, Ph.D.

David Hathaway, Ph.D.

Robert O'Dell, Ph.D.

Erin Rericha, Ph.D.

DEDICATION

To my son Kai

and

To my husband Chad

I love you both with all my heart!

ACKNOWLEDGMENTS

I am exceedingly grateful to all the students and teachers at the University of Memphis, the University of Hawaii Hilo, the University of Alabama Huntsville (theCSPAR group in particular), and Vanderbilt University. The countless people at these institutions have shaped me, molded me, and educated me along the way.

I would like to thank NASA and specifically the Living With a Star Program for providing me with a salary and paying my tuition so that I could continue my journey on this often daunting task of obtaining a Ph.D. I would also like to thank the solar physics group at NASA MSFC for being my friends and colleagues and for providing guidance throughout the last few years of this journey.

To all of my committee members, thank you for pushing me to see the bigger picture and for reminding me to always remember that the Sun is a Star. I also want to thank you for helping me to craft a dissertation that I can take pride in.

To my advisor and mentor Dr. David H. Hathaway of NASA MSFC, thank you for everything you have taught me. You are the epitome of what every student hopes to have in a mentor. You have been my friend and colleague and you have given me immeasurable professional support. It has truly been a pleasure to work with you.

I would also like to thank my family. To my son Kai, you are my pride and joy and you never fail to make me smile. To my mother Linda, thank you for being my role model and inspiring me to pursue my dreams. You have taught me to be strong, to find happiness in life, and to always try to be a *good liver*. To my sisters Laura and Linda, thank you for all your love and encouragement. I finally get to be *Dr. Lisa*, yea!!!

Finally, to my wonderful husband Chad, words could never express how much you mean to me. You have have given me a wealth of love and support. You are my best friend and the love of my life. Thank you for everything.

EXECUTIVE SUMMARY

The characterization and modeling of magnetic flux transport within the surface layers of the Sun are vital to explaining the sunspot cycle. The Sun's polar fields at solar cycle minimum are the seeds of the next solar cycle: weak polar fields produce weak cycles. Magnetic flux transport is key to the buildup of the polar fields and the subsequent magnetic reversals that are essential to modulating the sunspot cycle. The primary goals of this dissertation are threefold:

1. Make precise measurements of the Sun's axisymmetric flows (i.e., differential rotation and meridional flow).

2. Create a realistic surface flux transport model that reproduces the magnetic field evolution at the surface by incorporating the observed flows.

3. Investigate the role of flux transport in modulating the polar fields, and thereby the solar activity cycle.

This work has been done in collaboration with Dr. David H. Hathaway of NASA Marshall Space Flight Center.

In Chapter 1, I provide an introduction to the Sun as a star. I begin with a discussion on stellar structure and evolution. I then discuss the techniques and instruments that have been used to study the Sun. I conclude Chapter 1 with a section on magnetic activity cycles on the Sun and in other stars.

Magnetic flux on the Sun is transported by supergranular flows and the axisymmetric flows of differential rotation (DR) and meridional flow (MF). In Chapter 2, I introduce these flows. I then show a derivation of the Surface Flux Transport equation starting from Maxwell's equations and Ohm's Law. I conclude this chapter with an introduction to prior Surface Flux Transport models.

In Chapter 3, I discuss a cross-correlation technique that we have used on magnetograms (maps of the magnetic field strengths over the surface of the Sun) to characterize the DR and MF and their

variations from 1996 to present. Results show that while variability in DR is negligible, the MF varies in two fundamental ways: over the course of a solar cycle and from one cycle to the next. The MF is faster at solar cycle minimum and slower at maximum. Furthermore, the MF speeds that preceded the Solar Cycle 23/24 minimum were $\sim$ 20% faster than the MF speeds that preceded the prior minimum. This faster MF may have led to weaker polar field strengths and thus the subsequent extended solar minimum and an unusually weak Cycle 24. Chapter 3 also features an in-depth discussion a convective flow model developed by Dr. David Hathaway. Though this was not created as part of this dissertation, it constitutes a major component of the surface flux transport model.

To understand the impact flux transport on the evolution of the polar fields, I have conducted experiments using a surface magnetic flux transport model, introduced in Chapter 4, that we have developed. This model advects the magnetic flux emerging in active regions (sunspots) using detailed observations of the near-surface flows that transport the magnetic elements. These flows include the axisymmetric differential rotation and meridional flow and the non-axisymmetric cellular convective flows (supergranules), all of which vary in time in the model as indicated by direct observations. At each time step, magnetic maps of the entire Sun are created. These maps are used to create plots of the Sun's axial dipole moment, a measure of the polar field.

Also in Chapter 4, I illustrate how this model is used to create a baseline. In this regime, the model assimilates (i.e. continually adds in data weighted by its noise level) magnetic data from magnetograms at all available latitudes. This ensures that it accurately represents the magnetic fields observed on the surface of the Sun. This baseline is used to illustrate the difference in the timing of the polar field reversals based on four different definitions of polar fields. Advantages and disadvantages of each of these definitions are discussed.

In Chapter 5, I discuss how the model is used in a predictive or simulation regime. I have tested the predictability of this model using a baseline map as an initial condition, but with daily sunspot area data used to give the sources of new magnetic flux. I found that the strength of the polar fields at cycle minimum and the polar field reversals at cycle maximum can be reliably predicted up to 3

years in advance. I have included a prediction for the Cycle 24 polar field reversal.

In Chapter 6, I use the predictive model in three simulations to determine the impact of MF variations on the sunspot cycle. The first simulation included a MF that is constant, the second one included a MF that has the observed variations in time, and a third included a MF in which the observed variations were amplified. Comparisons of the strength of the polar fields produced with the baseline and the simulations are exceedingly well matched for the first few years, but then produce polar fields that are too strong. These results indicate excess flux is being added to the model. The results of the simulations with variable MF provide evidence that polar counter-cells are not present in the Sun's MF. Though an average Joys Law tilt was used consistently in the simulations, leading polarity poleward streams were still present in the magnetic butterfly diagrams, indicating that these poleward streams are not strictly due to variations in Joys Law tilt. Finally, the variations in the MF over Cycle 23 have a significant impact ($\sim$ 20%) on the polar fields. Rather than producing weaker polar fields as expected, these variations produced stronger polar fields. These results indicate weak Solar Cycle 24 is due to the weak amplitude of Cycle 23 and *not* the variations observed in the MF. However, the variation in the MF may still provide a feedback mechanism for regulating the solar cycle and possibly recovering from a Maunder-type minimum.

I summarize the major conclusions of this dissertation in Chapter 7.

TABLE OF CONTENTS

LIST OF FIGURES

CHAPTER 1

INTRODUCTION

The Sun provides Earth with warmth, light, and the energy that fuels our entire ecosystem. As the largest body in the solar system, the Sun is the focal point and guides the planets in their orbits. It is no surprise that it has been worshiped by cultures throughout history, yet there is still much that is not known about the Sun. Once thought to be constant and unchanging, it is only in modern times that is has become evident that the Sun is in fact extremely dynamic. Since the invention of the telescope, knowledge of the Sun has grown at an extraordinary rate. Each discovery brings new ideas and often conflict. Even now, our understanding of the Sun is constantly being redefined as each new discovery is made. For these reasons, the Sun is an exciting and challenging area of study.

1.1 The Sun as a Star

Perhaps one of the most important discoveries about the Sun was the realization that the Sun is in fact a star. This was not intuitive because the Sun appears so much brighter than all of the stars we see in the night sky, however the reason for this difference in the apparent brightness is distance. The flux density is given by the following equation:

$$F = \frac{L}{4\pi R^2} \tag{1.1}$$

where F is the flux density (i.e., apparent brightness), L is the luminosity (i.e., intrinsic brightness), and R is the distance to the star. While the Sun is a mere 8 light minutes from the Earth, the next closest star is 4.3 light years away (Kutner, 2003). The majority of the brightest stars in our night sky are even further, being tens or hundreds of light years away.

Stars like the Sun, our star, will have an average lifetime of ten billion years. The Sun is

currently in the middle of that lifetime. Examining the birth, life and death of other stars provides insight into where the Sun came from and what it's ultimate fate will be. Alternatively, the Sun provides an opportunity to look deeper into the details of the inner workings of a star, which has proven to be very complex. This highlights the importance of not only studying the Sun as it relates to our solar system, but of viewing the Sun as a window into the lives of the myriad of other stars in the universe.

1.1.1 Stellar Evolution

Stellar evolution begins with an enormous cloud consisting of hydrogen gas mixed with other trace elements. If the cloud is sufficiently dense, the force of gravity will cause this cloud to contract and a proto-star will form. The proto-star continues to contract and its temperature rises until it reaches hydrostatic equilibrium (i.e., the point when the outward gas pressure matches the inward pull of gravity). At this stage, the proto-star becomes a star known as a *T-Tauri star*. The infant star then begins it's decent down the Hyashi track. During this short phase of it's life the star is fully convective and its core temperature continues to rise. With a sufficient mass (M $\gtrsim 0.08 M_{\odot}$, where $M_{\odot}$ is the mass of the Sun), the star will compress until its core temperature becomes hot enough ($\sim 10^7 K$) to begin the nuclear fusion of hydrogen. With this ignition of nuclear fusion, the star graduates to adulthood: the *Main Sequence*. This is the phase of the star's life where the nuclear fusion of hydrogen into helium occurs in the core.

The Hertzsprung-Russell (HR) diagram, shown in Figure 1.1, best characterizes the life cycle of a star. The H-R diagram was conceived of in the early 1900s by Ejnar Hertzprung and Henry Norris Russell (Prialnik, 2009). Separately, both astronomers had the idea to plot the surface temperature (sometime called the effective temperature) of the stars versus their luminosities. The majority of stars ($\sim$ 99.9%) occupy the Main Sequence region of the HR diagram. The duration of this process is dependent on how much hydrogen is present and how quickly the nuclear fusion progresses. More massive stars contain more hydrogen, and thus their gravitational contraction is also greater. This increased gravitational contraction results in the star becoming much hotter and

thereby an increased rate of nuclear fusion. The net result is that the more massive a star is, the shorter the star's lifetime will be. However, generally more than 80% of a star's lifetime is spent in this phase of it's life.

The ultimate fate of the star will depend on the star's mass. As the hydrogen in the core of most stars is exhausted, hydrogen will begin burning in the outer layers, or the envelope. The envelope will expand and cool forming a red giant. The hydrogen burning in the shell will continue to deposit helium on the core, which will contract further. If the star is not massive enough $(0.08M_{\odot} \lesssim M \lesssim 1M_{\odot})$ to reach a core temperature that ignites helium ($\sim 10^8 K$), only a gradually cooling degenerate helium core, known as a *white dwarf*, will remain. These stars exist in the bottom left of the HR diagram. This will be the fate of our star, the Sun.

Stars with sufficient mass $(0.7M_{\odot} \lesssim M \lesssim 2M_{\odot})$ will begin nuclear fusion of the helium in the core. This is often an explosive event, occurring when the core has reached $\sim 0.5M_{\odot}$ in what is known as the *helium flash*. This process occurs very quickly and though the core expands even further and it's temperatures will drop, the outer shells will contract. The cooling results in a decreased luminosity, while the contracting outer layer cause an increase in the effective temperature. Together these processes form the horizontal branch of the HR digram, between the red giants and the main sequence. Many of the stars in the horizontal branch will become RR Lyrae variable stars with pulsations driven by the Kappa mechanism. This mechanism is due to an instability in the radiative envelope. Normally, compression will cause the temperature and density to rise resulting in a lowering of the opacity. This lowering of opacity will allow more effective radiative transport and the temperature will stabilize, reaching equilibrium. However, RR Lyrae stars are thought to have a significant amount of partially ionized helium in their envelopes. This changes the way in which the opacity responds to an increase in temperature: rather than lowering, the opacity increases. The heat, unable to escape, causes a buildup in pressure until the envelope rapidly expands and the cycle is repeated. The time frame for these pulsations is on the scale of hours.

Larger stars, between $2M_{\odot} \lesssim M \lesssim 10M_{\odot}$, have a more extended helium burning phase, sometimes referred to as the *helium main sequence*. Though helium burning is the primary energy

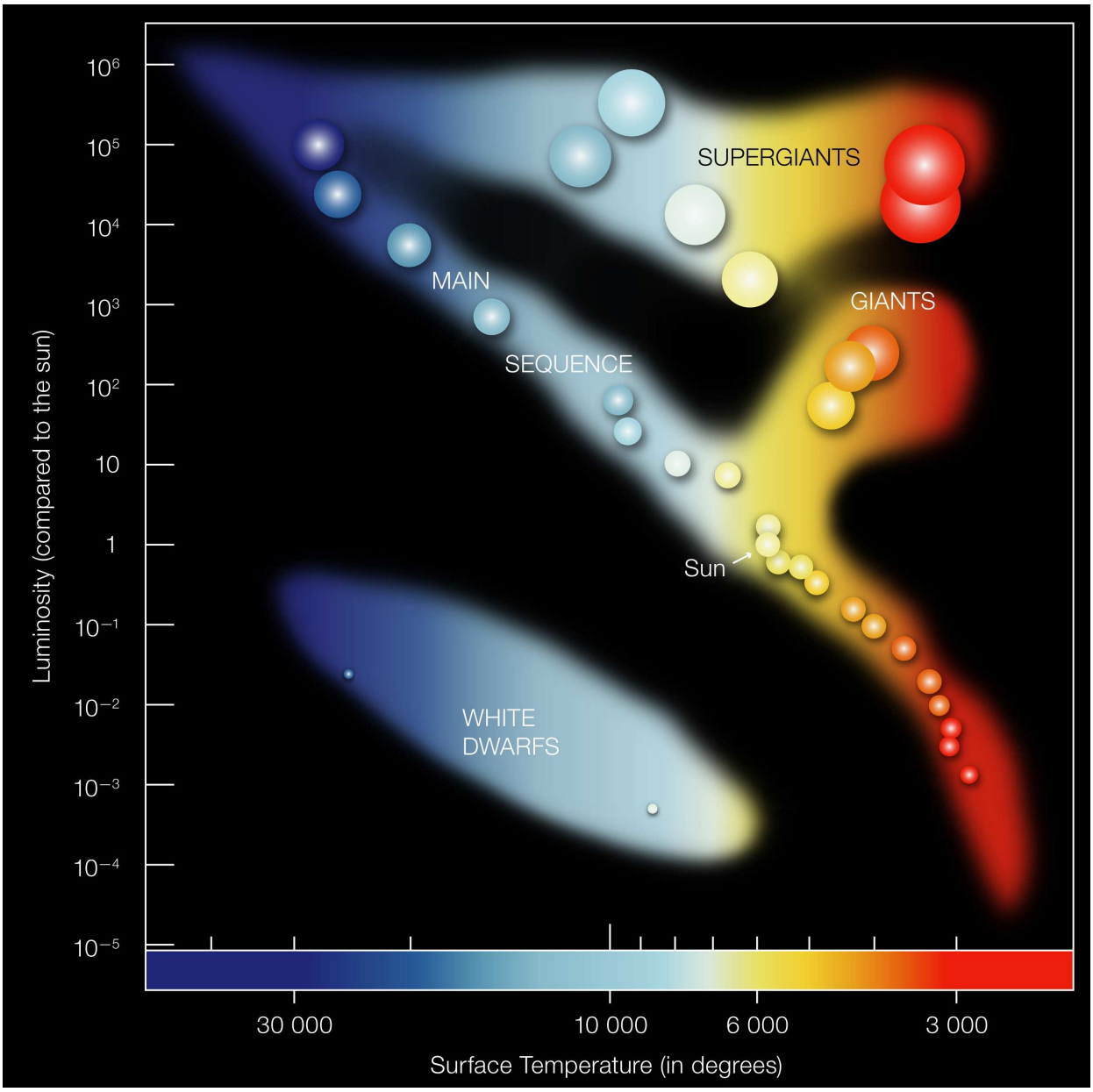

Figure 1.1: The Hertzprung-Russell Diagram. This diagram is a plot of stellar temperature vs. luminosity. The hydrogen burning life of the star is spent in the main sequence. Once the hydrogen has been depleted, the star will expand into a giant or fade into a white dwarf. The luminosity of a star is related to it's mass and lifetime. Stars in the top left of the main sequence will have masses of $(10M_{\odot} \lesssim M \lesssim 60M_{\odot})$ and lifetimes on the order of 10^7 years whereas stars on the bottom right will have masses of $(0.1M_{\odot} \lesssim M \lesssim 0.3M_{\odot})$ and have lifetimes on the order of 10^{12} years. (Credit: ESO, freely licensed by Creative Commons Attribution 3.0 Unported license.)

source for stars in this phase, hydrogen burning via the CNO cycle will also occur in a shell. These stars can also develop a Kappa mechanism instability. However, instead of lasting hours, these pulsations last days or months. These stars, known as *Cepheid variables*, are commonly used as a standard candle because their pulsation period is directly related to their luminosity. Using the luminosity in Equation (1.1), the distances to a Cepheid can be calculated with a high degree of accuracy. This is often how the distances to other galaxies are measured.

Once the helium in the core is depleted, the carbon and oxygen remaining in the core will begin to contract. During this phase, the asymptotic giant branch, the envelope will expand again and cool forming a supergiant. These stars will have two different burning shells in their envelopes: fusion precesses will alternate between a hydrogen burning outer shell and a helium burning inner shell. These stars have very fast stellar winds and subsequently have a high mass loss rate. These winds will cause the outer layers to slough off leaving behind a degenerate carbon and oxygen core and eventually forming a planetary nebula surrounding a white dwarf.

In much larger stars, $M \gtrsim 10 M_{\odot}$, fusion of heavier elements may occur in the core. Carbon, oxygen, and silicon fuse until an iron core remains (fusion of iron and heavier elements costs energy, rather than producing it). In these stars, the iron core will become so massive that it will approach the Chandrasekhar limit, or about $1.4\, M_{\odot}$). Once this limit has been reached, the electron degeneracy pressure can no longer support the core and it will collapse. This process causes an explosion known as a *supernova*, leaving behind a neutron star, or in more extreme cases a black hole may be formed. The energy released from this explosion is thought to be responsible for the creation of elements heavier than iron.

Amid the darkness of a dying star, there is light to be found. As with most things in nature, the cycle of life continues. The material that was expelled from a supernova will create new metal rich molecular clouds. Like the stars they were born from, this material in turn will begin to collapse and the next generation of stars will be formed. They will be denser, will reach higher temperatures, and will generally have shorter lifetimes, but it is in this way that the galaxy will continue to evolve.

1.1.2 Stellar Structure: The Role of Heat Transport

The center of each star is the core, where nuclear fusion takes place and energy is generated. At the surface of the star, the *photosphere*, the optical depth rapidly falls off and the photons and heat are easily radiated away. Between the core and the photosphere, the structure of a star is determined by the most efficient form of heat transport available in each layer. Typically heat transfer will occur via radiative transport. However if the temperature gradient is sufficiently large (usually due to high energy production or a high opacity), convection will occur. In convection, rising mass (i.e., plasma) expands and cools adiabatically but still finds itself hotter and less dense than its surroundings - so it continues to rise. Conversely, sinking mass contracts and heats adiabatically but still finding itself cooler than its surroundings - so it continues to sink. These rising and sinking motions coexist in the form of a circulating cellular structure, producing turbulent boiling motions. The radiative/convective balance has important ramifications in all phases of stellar evolution (e.g. RR Lyrae and Cepheid variables) however, this section will focus on it's role during the main sequence phase of a star's life.

The balance between being radiatively stable and convectively unstable is known as the Schwarzschild Stability Criterion (Schwarzschild, 1906). This criterion says that in order to remain stable the following relation must be maintained:

$$\left(\frac{dT}{dr}\right)_{radiative} < \left(\frac{dT}{dr}\right)_{adiabatic} \tag{1.2}$$

where $\left(\frac{dT}{dr}\right)_{radiative}$ is the temperature gradient for a star in radiative equilibrium and $\left(\frac{dT}{dr}\right)_{adiabatic}$ is the adiabatic temperature gradient. Consider a parcel of plasma with a temperature T_i and density ρ_i that begins to rise up. As it rises, the parcel will expand and cool adiabatically, reaching a temperature T_f and density ρ_f. If the Schwarzschild Stability Criterion is met, the parcel's density will exceed the density of the external plasma ($\rho_f > \rho_{ext}$) and it will fall back down. However if the stability criterion is not met, the temperature of the parcel will fall, but not as fast as the external plasma. The density will decrease, but more quickly than the external plasma. In this

case, the density of the external plasma will always exceed the density of the parcel ($\rho_{ext} > \rho_f$) and the parcel will continue to rise, thus producing convection.

The internal structure of stars consists of some combination of radiative and convective zones. This is illustrated in Figure 1.2. The smallest stars, M stars, have a very steep temperature gradient between their nuclear core and their photosphere: these stars are fully convective. As stars increase in mass, they are able to establish a small radiative zone. As the mass of the star increases, the radiative zone grows and the convective zone shrinks.

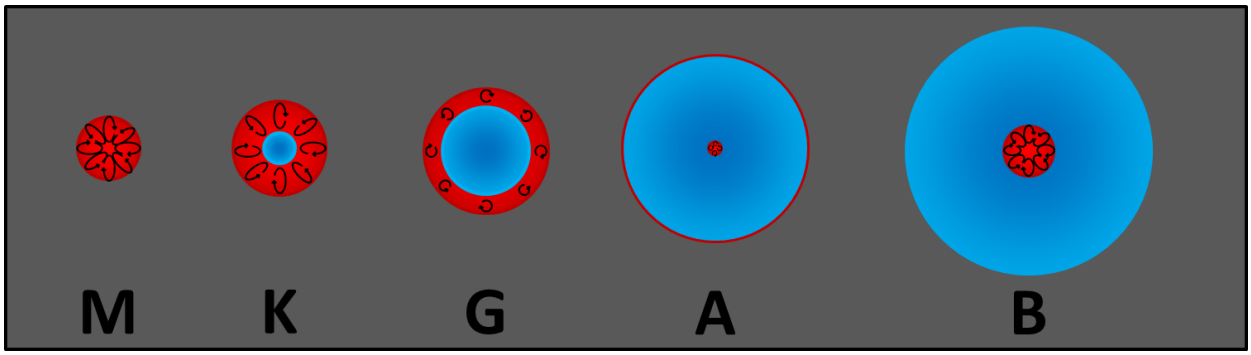

Figure 1.2: Stellar Interiors. This image illustrates the radiative (blue) and convective (red) configurations of stars of different sizes.

Convection in the Sun, a G star, occurs in the outer 30% of the interior. This creates cellular structures that come in a range of different sizes with different properties. These will be discussed in greater detail in Section 2.1.1.

More massive stars, e.g. A stars, will have only a very thin convective envelope. However, these stars have sufficient mass to begin the CNO cycle in their nuclear cores. The rate of energy production in the core becomes dependent on depth, producing another very steep temperature gradient and a convective core. For the largest stars, O and B stars, the convective envelope disappears completely while the convective core grows larger.

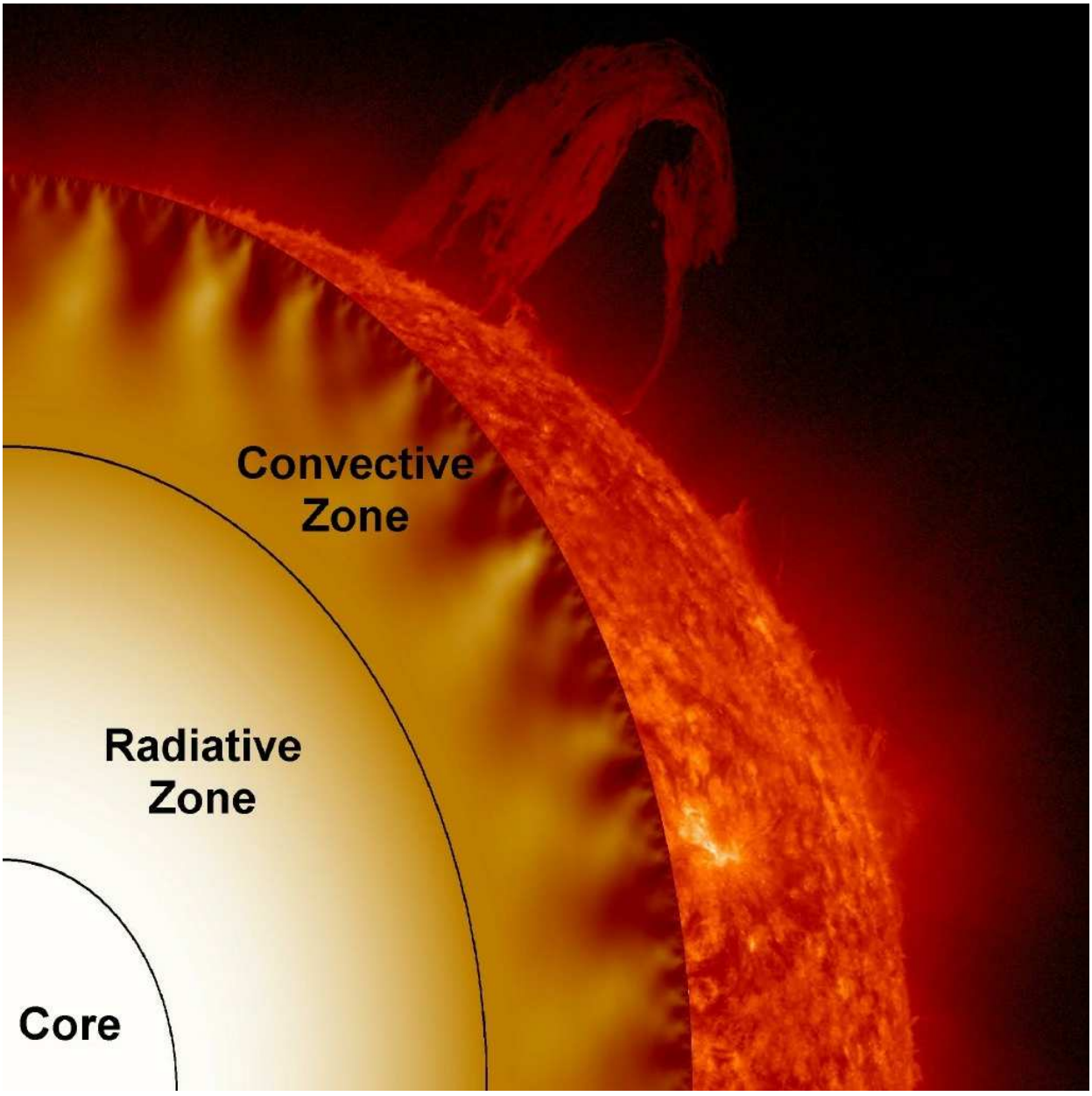

Figure 1.3: Solar Interior. Solar interior: core, radiative zone, convection zone. Credit: David Hathaway NASA/MSFC.

1.2 The Star in Our Backyard

As the star closest to us, the Sun provides the opportunity to observe a star in great detail. How do we study the Sun? The answer lies in the difference between night and day - light! In the late 1600's, Newton discovered that a prism could be used to split visible light into its component colors, producing a spectrum as a function of wavelength. In 1814, Josef von Fraunhofer used a prism to create images of the visible spectrum of sunlight and found that several black lines marred the spectrum. These lines, now known as *Fraunhofer lines*, were found to be caused by the absorption of photons by a cool gas surrounding the hotter light emitting gas (Golub & Pasachoff, 2001). The placement of these lines is dependent on the chemical composition of the surrounding gas. By examining the patterns of the Fraunhofer lines, astronomers have been able to determine the chemical makeup of the Sun: composed primarily of hydrogen and helium. The study of this spectrum, i.e., spectroscopy, has proven to be one of the most valuable techniques for studying the Sun.

In the 1890's, George Ellery Hale created a new instrument known as a *spectroheliograph* to image Sun in different wavelengths. This device uses a diffraction grating to split the solar spectrum to create an image of the Sun at a single wavelength. By looking at the Sun in different wavelengths, he was able to observe different features on the Sun. Nearly two decades later, he made a revolutionary discovery about the Sun when he observed the Zeeman effect (line splitting due to the polarization effect of the magnetic field) in sunspots (Hale, 1908): sunspots are magnetic in nature! A few years later, Hale suggested that not only were sunspots magnetic, but that the Sun as whole had a magnetic field (Hale, 1913).

The magnetic nature of the Sun led Harold D. Babcock and his son, Horace W. Babcock, to the develop the magnetograph in 1952 (Babcock & Babcock, 1952). The magnetograph is a device that uses the Zeeman effect to create maps of the magnetic field strengths over the surface of the Sun, these maps are known as *magnetograms*. Using the first magnetograph, they confirmed that Sun did indeed possess a weak dipolar magnetic field. Their magnetograph included a component

referred to as a Doppler compensating plate. This component was designed to remove the Doppler signal (frequency shift of wavelengths) due to rotational motion of the Sun. In 1953, Horace W. Babcock described how this component may be used as a separate instrument all together to measure the Sun's radial velocity (Babcock, 1953). Images made with this instrument are called *dopplergrams*.

Most of the light from the Sun comes from the photosphere, but a small portion, about one millionth (Phillips, 1992), is actually produced in the corona. This region of the Sun is so faint, that it can only be observed when the light from the photosphere is obscured, for instance by an eclipse. Eclipses occur when the moon's path passes between the Earth and the Sun, causing a shadow on the surface of the Earth. In most cases the moon will block only a portion of the Sun, however if the placement of the Earth, Moon, and Sun is just right, a small portion of the Earth will be able to witness a total solar eclipse. In a total solar eclipse, totality occurs when the moon passes directly in front of the Sun causing the entire Sun, with the exception of the far-reaching corona, to be blocked by the moon. When this dramatic event occurs, only the Sun's corona is visible. Solar physicists recognized that totality provided a unique opportunity to observe the corona. By using a spectrograph at the time of totality, the spectrum of the light specifically emitted by the corona could be observed. In fact, it was by this method that helium was first discovered (Golub & Pasachoff, 1997). Eclipses were so effective for studying the corona that they led to the invention of a new instrument: the coronagraph (a spectrograph that includes an occulting disk designed to mimic a solar eclipse). While the coronagraph has become an essential tool for solar physics, eclipses are more effective at occulting the Sun and are still studied by solar physicists (Golub & Pasachoff, 2001).

In addition to visible light, the Sun should produce neutrinos through nuclear fusion. These particles are extremely hard to detect because they primarily only interact with matter via the weak nuclear force (Golub & Pasachoff, 2001). In the late 1960's, experiments designed to take advantage of the most probable neutrino interactions were developed to detect neutrinos. The first of these experiments was the Homestake experiment, followed by the Kamiokande, Super-

K, and BOREXINO experiments. However, these experiments were only able to detect the more uncommon high-energy neutrinos. The SAGE and GALLEX experiments were designed to be able to detect neutrinos created by proton-proton reactions, most commonly produced in the Sun. Up to this point, neutrino detectors were only able to detect a fraction of the expected number of neutrinos - a discrepancy referred to as the neutrino problem. However, the Sudbury Neutrino Observatory was recently designed to detect all types of neutrinos. They were able to verify that neutrinos have mass and can change type. They found that the missing neutrinos from previous experiments had changed to types that could not be detected in those experiments. This has led to changes in our current understanding of solar physics as well as nuclear physics.

Another recently developed method of studying the Sun is *helioseismology*. Seismologists study the movement of waves through various media, and likewise helioseismologists use dopplergrams to study how waves move inside the Sun, allowing solar physicists to learn about the solar interior. Several characteristics of the Sun, such as temperature, composition, density, and the motion of the plasma, affect the propagation of the waves and can be determined using helioseismology. Helioseismology has shown that the waves moving inside the Sun produce specific modes of oscillation. Careful analysis of these modes of oscillation can be used to determine how plasma moves inside the Sun. One of the most significant results so far has shown that the axisymmetric motion of the Sun's plasma vary with depth. In addition, it has shown how the speed of sound in the plasma varies in an around a sunspot. Perhaps most significantly, helioseismology can be used to produce maps of active regions on the opposite side of the Sun, a critical tool for the field of space weather prediction.

Observatories designed for studying the Sun have been built all over the world. The largest and most well known of the traditional optical observatories that study the Sun include Mount Wilson Observatories, Mauna Loa Solar Observatories , Big Bear Solar Observatories, Swedish Solar Observatories, Kitt Peak National Observatory, and the Sacramento Peak Observatory. Radio telescopes used to study the Sun include Nancay Radioheliograph in France, Nobeyama Radio Observatory in Japan, and the Very Large Array in New Mexico. In addition to these already

active telescopes, there is a collaborative effort to build a very large (400cm) solar telescope on Haleakala in Maui. Currently under construction, the Advanced Technology Solar Telescope is expecting to receive first light in 2018. Once complete, the large aperture combined with adaptive optics is expected to provide images of the Sun with a resolution on the order of one tenth of an arc second, the highest resolution of any solar telescope.

The spectrum of visible light makes up only a tiny portion of the electromagnetic spectrum. The ultraviolet, x-ray, and infrared portions of the spectrum are blocked by the Earth's atmosphere, therefore early observations of the Sun were limited to the visible portion of the spectrum. As the technology advanced, astronomers were no longer limited to ground based telescopes - the instruments could now be put into space. Without the interference of the Earth's atmosphere, whole new areas of the spectrum could be observed . Furthermore, with the proper orbital placement, observations were no longer restricted to the day, allowing for observations for extended periods of time. Over the last several decades, many instruments have been sent into space to study the Sun. These instruments have brought new discoveries as well as new questions.

Space-based study of the Sun began with the development of rockets carrying instruments, launched high into the atmosphere to take measurements. After a short period of observation, these instruments would fall back to Earth, where they would be found and (if not destroyed in the fall) the data could be analyzed. In the 1960's NASA began launching satellites called Orbiting Solar Observatories to study UV and X-Ray emissions from orbit. NASA's manned mission, Skylab, was launched in 1973 and a new age of solar observation began. New solar structures were revealed and the true nature of the Sun had begun unfolding. Through most of the 1980's, the Solar Maximum Mission (SMM) continued to provide details of these newly discovered structures. The Ulysses Mission was launched in 1990 as a collaborative effort between the European Space Agency (ESA) and NASA. It used Jupiter's gravity to slingshot over the solar poles.

In the last twenty years more sophisticated instruments have been developed and put into space. The Solar and Heliospheric Observatory (SOHO), another ESA/NASA collaborative effort, was launched in 1995 and is now stationed in orbit around the Sun at the L1 point. SOHO

houses twelve instruments: Coronal Diagnostic Spectrometer (CDS), Charge ELement and Isotope Analysis System (CELIAS), Comprehensive SupraThermal and Energetic Particle analyzer collaboration (COSTEP), Extreme ultraviolet Imaging Telescope (EIT), Energetic and Relativistic Nuclei and Electron experiment (ERNE), Global Oscillations at Low Frequencies (GOLF), Large Angle and Spectrometric Coronagraph (LASCO), Michelson Doppler Imager (MDI), Solar Ultraviolet Measurement of Emitted Radiation (SUMER), Solar Wind ANisotropies (SWAN), UltraViolet Coronagraph Spectrometer (UVCS), and Variability of solar IRradiance and Gravity Oscillations (VIRGO). On June 24th of 1998, SOHO lost it's pointing on the Sun and the following day communications with the satellite was lost as well (Vandenbussche, 1999). A recovery team was created, and the following month the Arecibo radio telescope and the Deep Space Network were used to obtain telemetry on the elusive satellite. Over the next couple of months the team was able to perform a series of maneuvers to regain SOHO's pointing on the Sun. October of 1998 was spent recovering the instruments, only to have the satellites remaining gyro fail the following December. Fortunately, in February of 1999 ESA was able to implement a modified control system that did not require gyros. This time period, in which SOHO was not functioning properly, has been referred to as the "SOHO summer Vacation." While many of SOHO's instruments have recently been decommissioned, they have been used to study many aspects of the Sun, including the Solar Interior, the Inner and Outer Corona, and the Solar Wind.

In the spring of 2010, the Solar Dynamics Observatory (SDO) was launched. SDO is the first mission operated by NASA's Living With a Star (LWS) program and is in a geosynchronous orbit around the Earth that allows for nearly continuous (with the exception of brief eclipses) observation of the Sun. SDO houses three instruments: the Atmospheric Imaging Assembly (AIA), the Extreme Ultraviolet Variability Experiment (EVE), and the Helioseismic and Magnetic Imager (HMI). AIA is a set of four telescopes that create images of the Sun in visible, ultraviolet, and extreme ultraviolet (EUV) wavelengths with the primary goal of learning how solar storms form on the surface and propagate through the corona. The EVE instrument tracks EUV variability. HMI creates high resolution (4096x4096) full Sun dopplergrams and magnetograms at a very high

cadence of 45 seconds. This instrument is used to study the motion of magnetic fields and acoustic waves (e.g helioseismology) across the surface of the Sun.

The observables for the research conducted in this dissertation are obtained from the SOHO/MDI and SDO/HMI instruments (Scherrer et al., 1995, 2012). The MDI instrument obtained full-disk magnetograms with a resolution of 1024x1024 and at a cadence of 96 minutes. This instrument was in operation from May 1996 to March of 2011, with an interruption during the "SOHO summer Vacation." HMI, the successor and more capable version of MDI, began obtaining full-disk magnetograms in April 2010. There is almost a full year of overlap (2010 April to 2011 March) in the observations of MDI and HMI. HMI magnetograms, with a size of 4096^2, have four times the spatial resolution of MDI full-disk magnetograms and are continuously available with a cadence of 45 seconds, rather than the 96 minutes of MDI. In addition to the better resolution and higher cadence, HMI also has a much better signal to noise ratio (this is particularly evident at the limb). Figure 1.4 shows a comparison of MDI to HMI data.

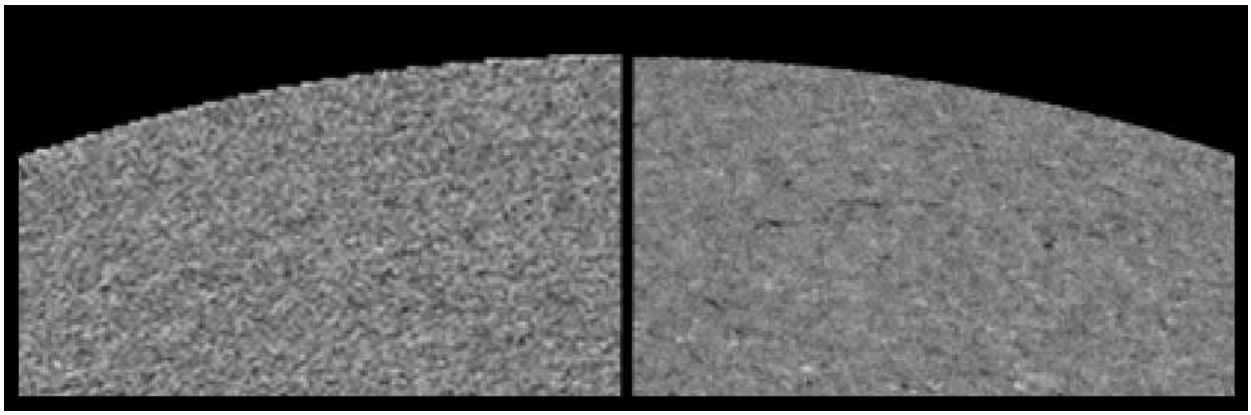

Figure 1.4: MDI versus HMI. MDI data (left) is compared to HMI data (right). HMI has four times the resolution and much less noise. This is particularly evident near the poles.

1.3 Magnetic Activity Cycles

1.3.1 The Solar Activity Cycle

Sunspots, dark regions appearing on the surface of the Sun, were the first features to be observed on the Sun. Sunspots are formed when magnetic field lines emerge through the photosphere (Figure 1.5) preventing heat transport by convection. In the 1800s astronomers realized that the sunspot number was cyclic, with a period averaging about 11 years. As new features of the Sun (solar flares, filaments, prominences, coronal loops and coronal mass ejections) were discovered, it was found that they too varied along with the frequency of sunspots. The sunspot number is now commonly accepted as a measure of solar activity. Solar activity itself has been linked to satellite failures, electrical power outages, and variations in Earths climate (Lean & Rind, 2008). The impact of solar activity on Earth and our technology has created a need for a better understanding of, and the ability to predict, solar activity.

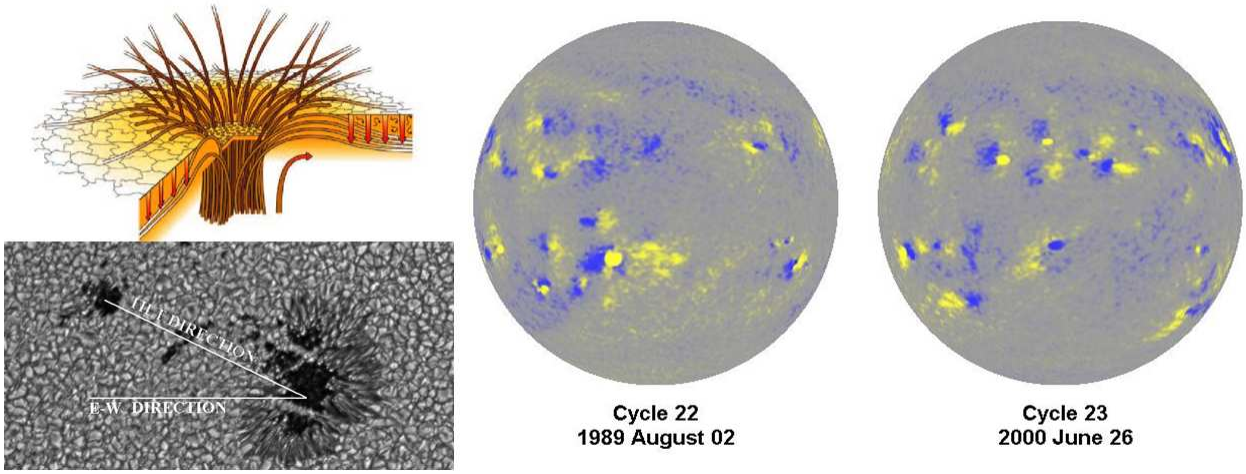

Figure 1.5: Sunspots. a) Sunspots are formed when magnetic field lines emerge through the photosphere. b) Sunspot groups possess a characteristic tilt, known as *Joys Law*. c) Sunspot groups have opposite polarity from north to south and polarity changes from cycle to cycle. This is known as *Hales Polarity Law*. Credit: David Hathaway, NASA/MSFC.

Observations of sunspots have revealed several characteristics that are important to understanding the physical mechanisms of the activity cycle. Sunspots were used to determine that the Sun rotates in 27 days (or 1 Carrington Rotation). Sunspots usually occur in groups known as *active regions*, which have a leading polarity where the magnetic field emerges and a following polarity where the magnetic field submerges. Active regions follow Joy's Law, which says that sunspot groups have a tilt that changes with latitude and is such that the leading spots are more equatorward than the following spots (shown in Figure 1.5b). Sunspots groups also have opposite polarity from north to south and this polarity changes from cycle to cycle. This effect is known as *Hale's Polarity Law* and is illustrated in Figure 1.5c.

Sunspot activity over the last four hundred years, plotted in Figure 1.6, has shown that the amplitude of the sunspot cycle varies from one cycle to the next. The average cycle has a peak sunspot number of about 100. At times, as in the period known as the *Maunder Minimum* between 1645 and 1715, solar activity can become so weak that it seems to disappear for several decades at a time. Figure 1.7 is a Magnetic Butterfly Diagram which illustrates how the distribution of magnetic flux changes over time. Sunspots appear in bands on either side of the equator. Cycles typically overlap by 2-3 years. At the beginning of each cycle, the active regions emerge at latitudes of about 30°. As the cycle progresses, the active regions emerge closer and closer to the equator, an effect known as *Spörer's Law*. Cancellation of polarity across the equator leaves behind an excess of following polarity that is transported to the poles. The north and south poles have opposite polarities that reverse from cycle to cycle. The timing of this polar field reversal is near the time of the solar cycle maximum.

Obtaining a good understanding of the solar cycle and its variability is the oldest and most significant problem in solar physics. Larmor (1919) suggested that induction by fluid (plasma) motion could self-generate magnetic fields. However, Cowling (1933) showed that axisymmetric motions could not self-generate magnetic fields (this is sometimes referred to as *Cowling's anti-dynamo theorem*). Elsasser (1946) and Bullard (1949) showed that non-axisymmetric motions could self-generate magnetic fields. Parker (1955) derived a set of dynamo equations in which

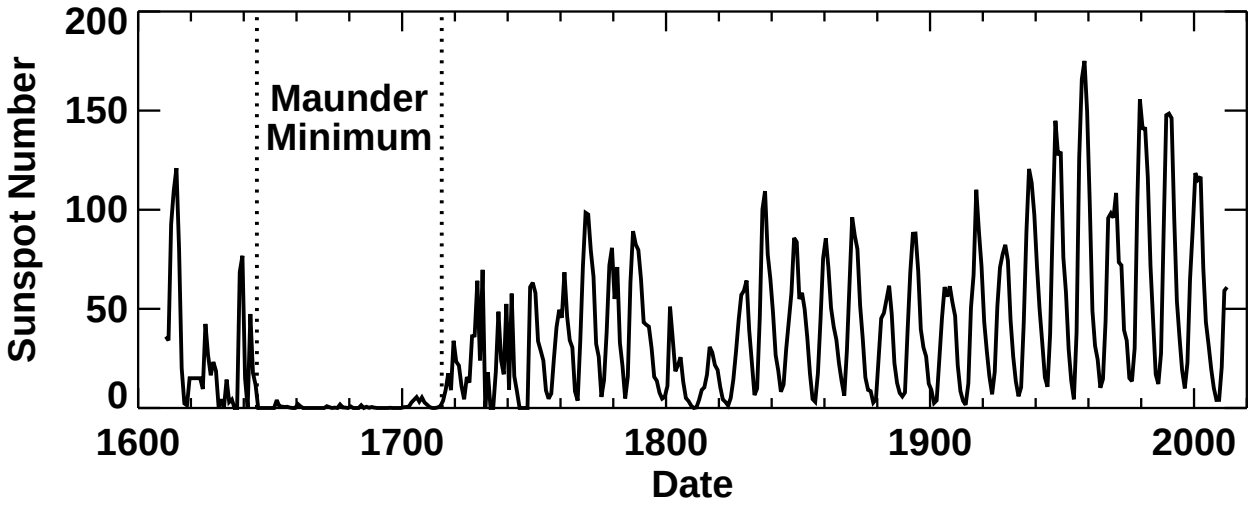

Figure 1.6: Sunspot Cycles. The amplitude of the sunspot cycles from 1600 to present varies substantially. This includes the Maunder Minimum, a period from 1645 to 1715 when the magnetic fields were too weak to produce sunspots. Credit: David Hathaway, NASA/MSFC.

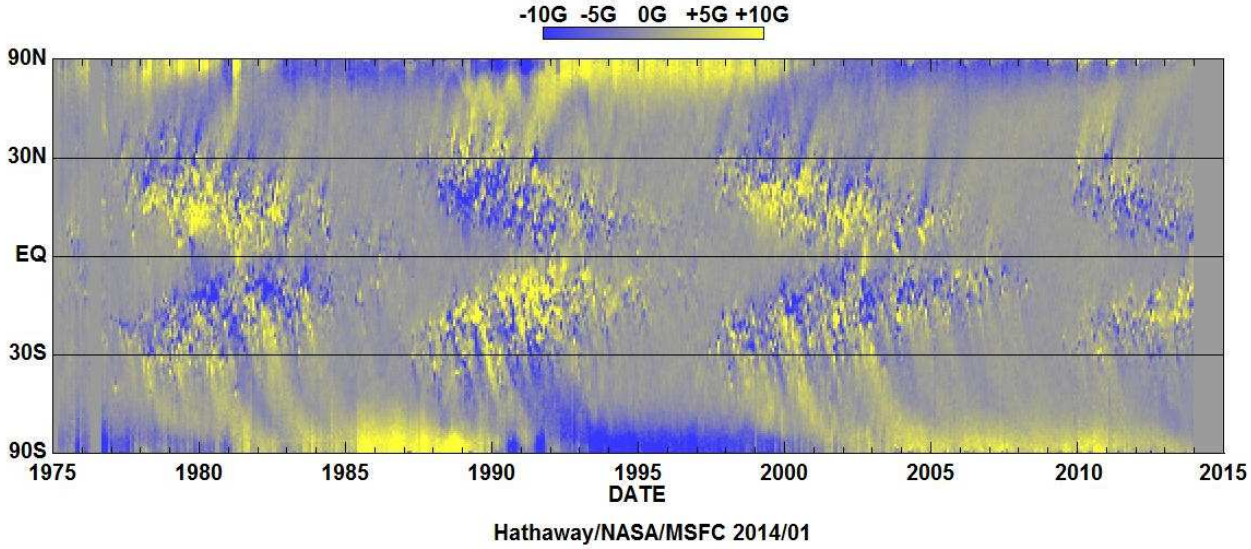

Figure 1.7: Magnetic Butterfly Diagram. This shows the distribution of the surface magnetic field (longitudinally averaged) over the last three and a half solar cycles. The poles have opposite polarities that switch from one cycle to the next near the time of solar maximum. Credit: David Hathaway, NASA/MSFC.

non-axisymmetric lifting and twisting of magnetic field by convective motions could generate an oscillating magnetic field.

H.W. Babcock (1961) proposed the first complete (but phenomenological rather than numerical) Dynamo Model to explain the magnetic properties that were observed on the Sun. This model, illustrated in Figure 1.8, progresses in four stages:

a. Solar Minimum. An axisymmetric dipole (poloidal) field exists. Field lines emerge at latitudes $\geq 55^\circ$ and thread through the convection zone to the opposite hemisphere.

b. Differential Rotation causes the submerged magnetic field to stretch in the toroidal direction (wrapping around the Sun). The field is strengthened by this stretching.

c. The toroidal field become buoyant and causes sunspots to emerge with Joy's Tilt and Hale's Polarity (polarity of leading spots matches the polarity of the polar field at minimum).

d. Magnetic flux is shredded off of the sunspots. The leading polarity fields cancel across the equator. The surface flows transport the following polarity to the poles. The following polarity cancels the old polar field and creates a new poloidal field with opposite polarity.

While Babcock's model is widely accepted as the underlying mechanism behind the solar cycle, the finer details are still not well understood.

Given this (and many more recent dynamo models), most solar physicists agree that the polar fields at solar minimum are the seeds to the next solar cycle. Indeed, observations have shown that the strength of the polar fields is a good indicator of the strength of the next cycle (Svalgaard et al., 2005; Muñoz-Jaramillo et al., 2012; Svalgaard & Kamide, 2013). Interestingly, the polar fields observed after the Cycle 23 maximum became about half as strong as observed for the previous two cycles, (Figure 1.9) This was followed by an extended Cycle 23/24 minimum and what is proving to be the weakest solar cycle in at least a hundred years. This has caused speculation that the Sun may be entering another Maunder Minimum. With such unusual solar conditions in our midst, solar physicists are becoming more motivated to determine exactly how magnetic flux is transported to the poles and how the polar fields are modulated.

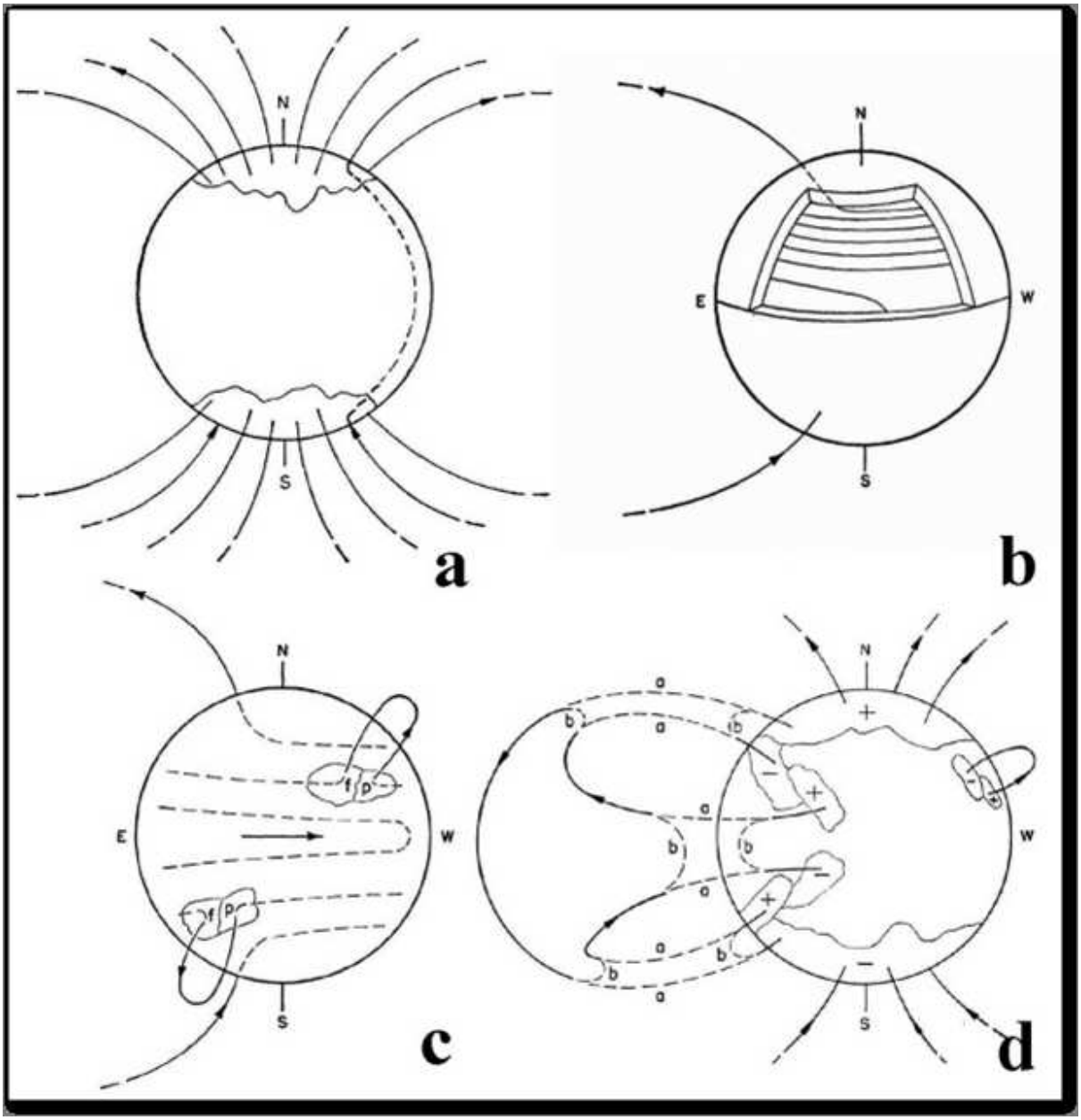

Figure 1.8: Babcock's Dynamo Model (1961). This image shows the stages of Babcocks Dynamo Model. (a) The Sun starts with a dipole poloidal field. (b) Differential rotation converts it to toroidal field. (c) The toroidal field gets stronger, becomes buoyant, and the fields then emerge with a slight tilt. (d) Cancellation occurs at low latitudes and the excess polarity is transported to the poles and reverses the poloidal field. Credit: Adapted from Babcock (1961) by David Hathaway, NASA/MSFC.

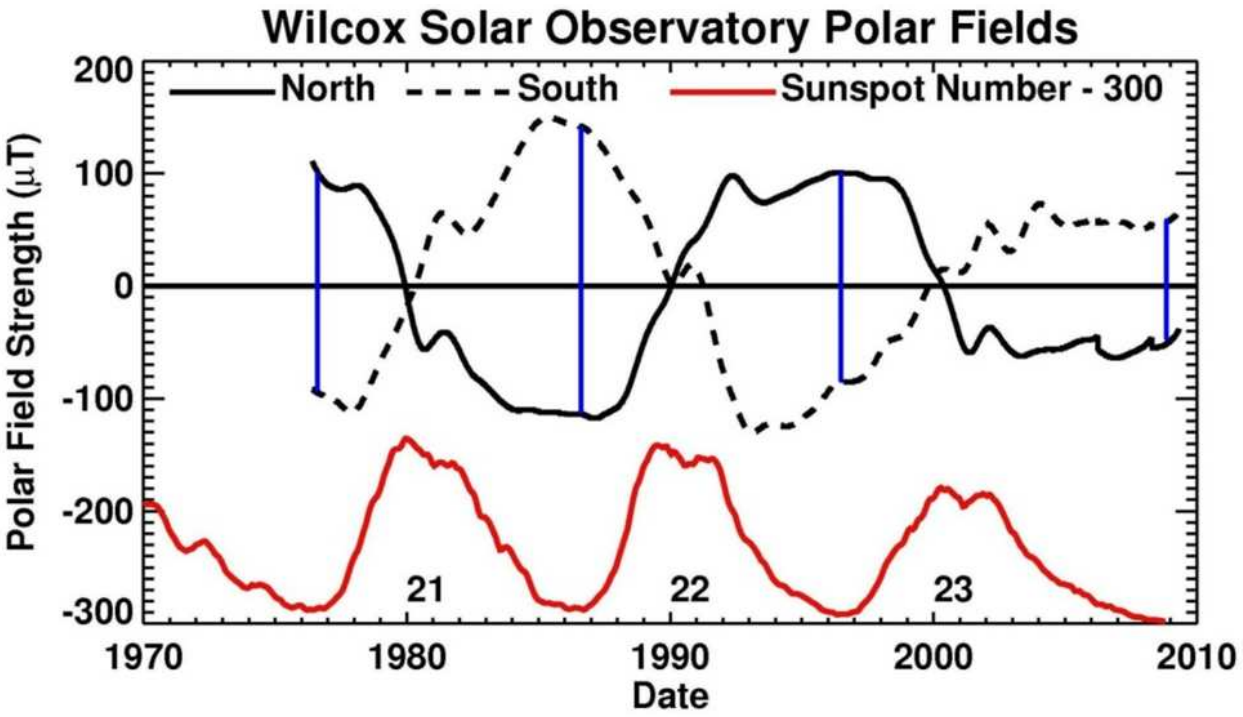

Figure 1.9: Polar Field Strengths. This image shows the variation in the strength of the polar fields over the last three solar cycles. Polar field strengths during the Cycle 23/24 minimum were much weaker (1/2) than for the prior two minima.

1.3.2 Stellar Activity Cycles

The solar activity cycle has led astrophysicists to look for similar magnetic variations in stars. They knew that the combined effects of convection and rotation could create stellar dynamos that produce activity cycles on stars. With this knowledge, the search for activity in other stars began with understanding rotation. Stellar rotation arises from random motions within the the hydrogen cloud that ultimately coalesces into a star. As the cloud contracts any net rotational motion is amplified by the conservation of angular momentum, causing the cloud to spin and flatten. The proto-star forms at the center and as it contracts further the rotation increases, giving rise to a rapidly rotating newborn star. Such rapid rotation, causes many stars to have an equatorial bulge.

Skumanich (1972) found that the rotation rate of young stars rapidly declines with age (i.e., *Main sequence spin-down*) such that

$$\Omega_e \propto t^{-1/2} \tag{1.3}$$

where Ω_e is the equatorial angular velocity and t is the age of the star. As a consequence, comparatively young O and B stars tend to have much faster ($\sim$ an order of magnitude) average rotation rates than long lived F and G stars. He also found that this same time dependence existed for Ca II H and K emission, which is an indicator of magnetic activity in the lower atmospheres of stars (Frazier, 1970). This led to the idea that young stars (younger than 100,000 years of age) experience *magnetic braking*, in which strong stellar winds of young stars expel matter. This matter is then captured by the extended magnetic fields of the star where they are carried away from the star, resulting in a loss of rotation rate by conservation of angular momentum.

Wilson (1978) and Baliunas et al. (1995) monitored the H and K Ca II emissions of F, G, and M stars from 1966 to 1993. Wilson (1978) found that most F and G stars exhibit fluctuations in magnetic activity and suggested that these fluctuations might be due to cyclic magnetic behavior similar to the Sun's magnetic activity cycle (described in Section 1.3.1). Baliunas et al. (1995) found that stellar activity cycles were related to the age of the stars. Young fast rotating stars are very magnetically active, but do not present smooth cyclic variation. Adolescent stars ($\sim$1-2 Gyr for 1 $M_\odot$) with moderate rotation rates have moderate cyclic activity and sometimes have periods of smooth cyclic variation. Older, slow rotating stars have weaker magnetic activity and intermittent cycles. Astrophysicists now believe that as the star ages its rotation rate slows, causing a decrease in stellar activity. Our Sun, with an activity cycle of its own, is an essential tool to understanding the dynamo processes that go on inside a star

Coming full circle, we find that solar and stellar physics are deeply entwined. The sheer number and variety of stars provide the statistics needed to paint a picture of the lives of these celestial objects whose lifetimes seem eternal when compared to our own. Conversely, the Sun provides

fine detail needed to unravel the physical processes taking place within stars so distant that they appear as little more than a point of light.

CHAPTER 2

FLUX TRANSPORT OF THE SUN

The magnetic fields at the surface of the Sun provide the inner boundary condition for the heliosphere. As such, motions of magnetic flux near the solar surface are crucial to studies involving the heliospheric magnetic field configuration, active region evolution, the buildup of polar fields, and subsequent magnetic reversals. Furthermore, surface magnetic flux transport is vital to dynamo models used to explain the sunspot cycle itself. In this chapter, I will introduce the flows that transport magnetic flux on the Sun (Section 2.1) and previous models that have used these flows to investigate the solar dynamo and the solar activity cycle (Section 2.2).

2.1 Solar Flux Transport Flows

Motions of magnetic flux on the surface of the Sun are characterized by three primary modes of transport: supergranular flows, differential rotation, and meridional flow. Supergranular flows are cause by convection in the Sun. These turbulent flows are the most complex of the surface flows, acting on multiple scales and in all directions. Both differential rotation and meridional flow are axisymmetric. Differential rotation describes the longitudinal motion, while meridional flow describes the latitudinal motion. Differential rotation produces a relative longitudinal velocity of 200-250 m s^{-1} at the surface of the Sun. Supergranular flows produce cellular velocities on the order of 500 m s^{-1}. However, meridional flow speeds are only on the order of 10-20 m s^{-1}.

2.1.1 Supergranulation

Convection is a product of the large temperature gradient in the Sun's convection zone. This temperature gradient causes the plasma to rise and fall like boiling water. The size of these convective cells (shown in 2.1) span two to three orders of magnitude: from *granules* with diameters of $\sim$1000 km, to *supergranules* with diameters of $\sim$30,000 km, and to *giant cells* with diameters of $\sim$200,000

km. These cells also have a range of lifetimes. Granules have lifetimes of only ∼10 minutes, while supergranules have lifetimes of many hours. The flows within these cells varies as well. Granules have internal velocities of ∼3000 m s^{-1}, whereas supergranules have internal velocities of ∼500 m s^{-1}.

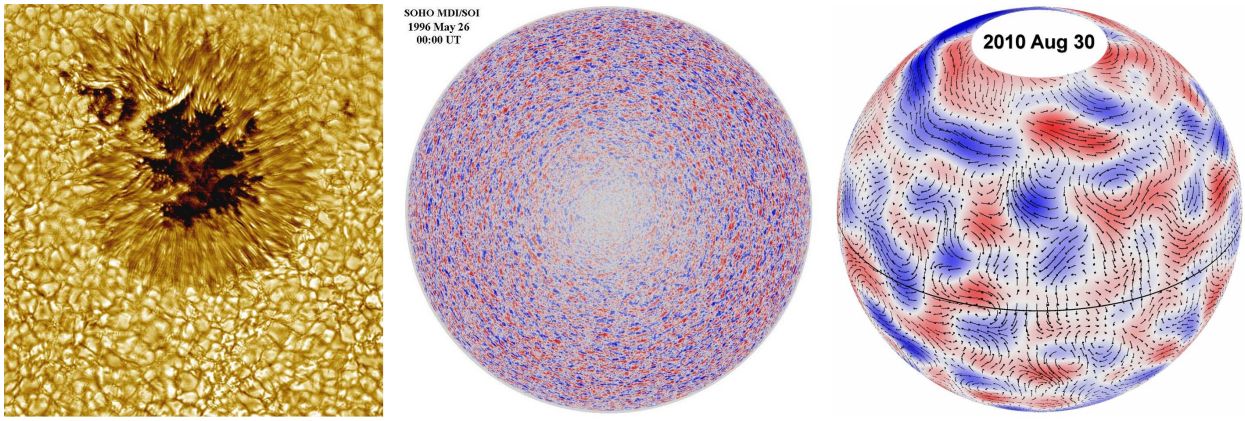

Figure 2.1: Convection Cells. Granules (left) have diameters of ∼1000 km, velocities of ∼3000 m s^{-1}, and lifetimes of ∼10 minutes. Supergranules (middle) have diameters of ∼30,000 km, velocities of ∼500 m s^{-1}, and lifetimes of about a day. Giant cells (right) have diameters of ∼200,000 km, velocities of ∼10 m s^{-1}, and lifetime of a couple month. Credit: David Hathaway NASA/MSFC.

As an aside, it should be noted that convective cells span the entire range of sizes between granules and giant cells. Granules and giant cells are distinct features because they represent the smallest and largest convective structures observed on the Sun. Both granules and supergranules are distinct because they produce the peaks in the distribution of convective cells as a function of size, i.e., these are the most prevalent convective structures. While some solar physicists refer to *mesogranule* structures between granules and supergranules, these structures occur at a dip in the power spectra. Furthermore, mesogranules have yet to exhibit any unique physical significance.

Granules are the smallest convective structures on the Sun. Sir William Herschel first noted

their existence in 1794 (Hoyt & Schatten, 1992). Granules exist at the top of the photosphere and represent the boundary between convective heat transport of the interior and radiative cooling of the optically thin atmosphere of the Sun.

Supergranules were discovered by Leighton et al. (1962), who had been investigating the Zeeman effect in solar spectral lines. The intense magnetic field in the Sun causes certain spectral lines to split with different polarization on the red and blue wings. They photographically combined spectroheliograms of the Sun from the red and blue wings of a spectral line, which produced velocity (Doppler) maps of the surface of the Sun. They compared velocity maps taken at different intervals with respect to one another and discovered oscillations on the surface of the Sun. These oscillations seemed to occur on a time scale of about five minutes. Ulrich (1970) attributed these oscillations to acoustic waves (seismic activity) in the Sun, thus producing the term helioseismology. We now know that the convective motions produce sound waves that interact with one another and reflect off the surface of the Sun. Interference causes waves to combine or cancel with one another, amplifying some modes and diminishing others. The peak of the resulting power spectrum occurs at 3mHz, corresponding to oscillations that have periods of five minutes, i.e., *5-minute oscillations*. (These features are sometime referred to as *p-modes* because pressure is the restoring force that drives the acoustic waves that cause these oscillations.)

Leighton et al. (1962) were able to remove the signal due to the 5-minute oscillations from the Doppler pattern (by adding together Doppler images taken several minutes apart) unveiling a new cellular pattern on the surface of the Sun. Though these supergranule cells were originally discovered by Hart (1954), who observed their motions as a noisy velocity fluctuation, it was not until the 5-minute oscillations were removed that the significance of these convective cells became evident.

It was clear from the initial discovery that supergranules play a crucial role in magnetic flux transport. Observations (Simon & Leighton, 1964) showed that as the plasma spreads out from the cell centers, small magnetic elements are transported to the boundaries of each convective cell, producing a cellular pattern, or *magnetic network* on the surface of the Sun. The magnetic ele-

ments remain trapped within the lanes in between supergranules, where they are shuffled around by the motion of the supergranules themselves. Leighton (1964) recognized that the evolution of supergranules produced a diffusive random-walk motion that could carry the following polarity magnetic elements poleward, leaving behind the leading polarity magnetic elements to cancel across the equator. He originally suggested this process alone might be sufficient to drive polar field reversals, claiming the random-walk motions could produce a diffusivity of $700 - 1540$ km s^{-1}. However, measurements of the diffusivity have found it to only be $70 - 250$ km s^{-1} (Hagenaar et al., 1999).

Following the discovery of supergranules, Simon & Weiss (1968) predicted that solar convection would create much larger convective cells, *giant cells*, that would extend to the base of the convection zone and form a larger network. These giant cells, with lifetimes on the order of months, would be heavily influenced by the Sun's rotation (Gilman, 1979). The giant cells were expected to transport angular momentum to the equator, driving the differential rotation of the Sun. In the decades that followed, observations hinted at the existence of these convective structures (Hathaway et al., 1996; Beck et al., 1998; Hathaway et al., 2000), but direct observations remained elusive until 2013 when they were observed by Hathaway et al. (2013).

2.1.2 Differential Rotation

Differential rotation was first noticed in 1610 by Christoph Scheiner by observing the motions of sunspots. He found that some sunspots were able to complete a full rotation in 25 days, while others took closer to 28 days. This inconsistency led him to the realization that the Sun experiences differential rotation, i.e the rate of rotation depends on latitude (see Figure 2.2). By the late 1850's, Richard C. Carrington had accurately tracked and recorded the motions of sunspots on the Sun (Carrington, 1859). (By doing so, he was able to determine that the rotational axis of the Sun was tilted by about 7.25° with respect to the ecliptic.) In order to create a standard of reference, Carrington calculated the average synodic (as viewed from the Earth orbiting the Sun) rotation rate of the Sun. A full rotation of the Sun (27.2753 days) is now know as a *Carrington Rotation*.

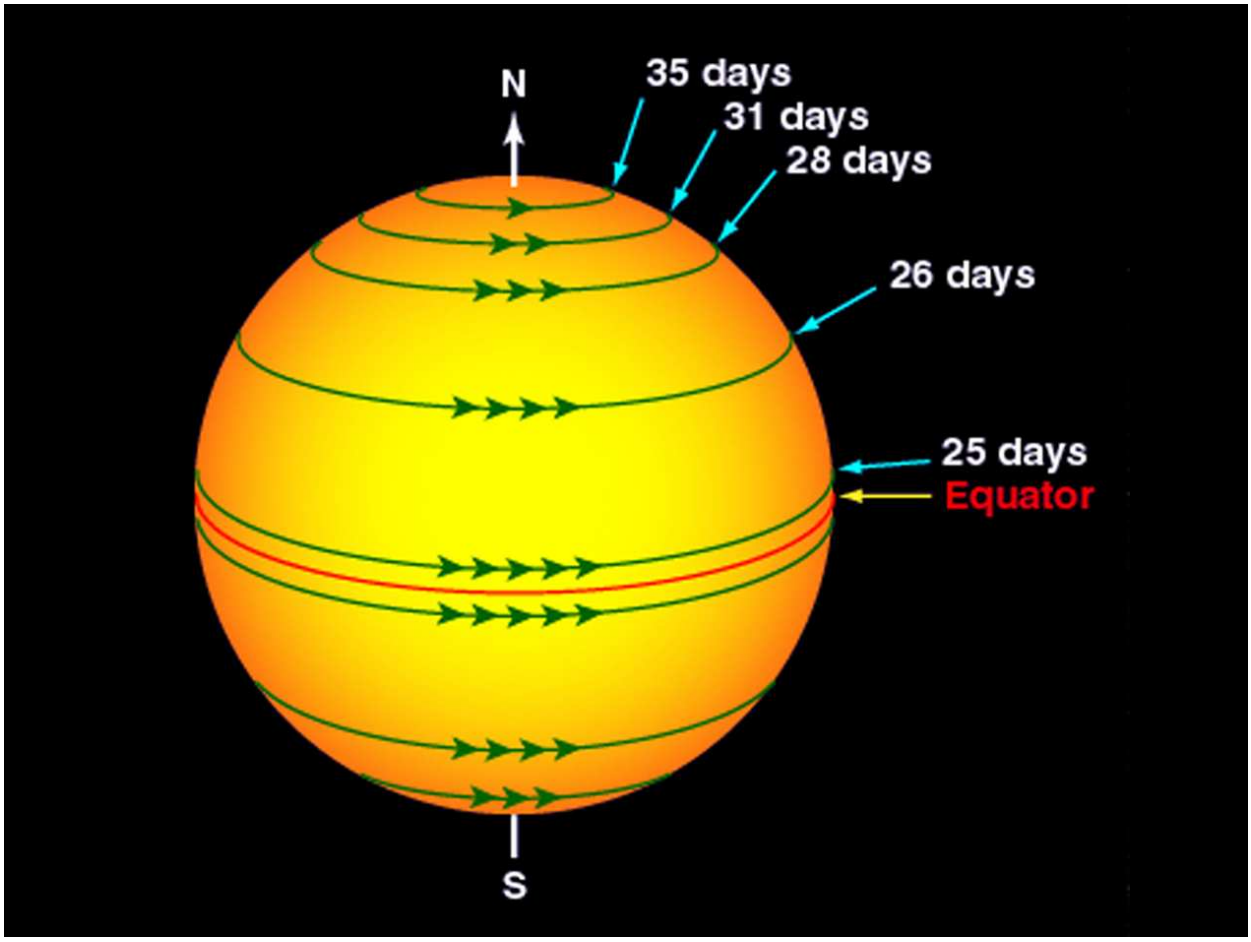

Figure 2.2: Surface Differential Rotation. The Sun is not a solid body and rotates at different rates depending on latitude and depth, i.e., differential rotation. The Sun undergoes one full rotation in about 25 days at the equator, but in about 36 days at the poles. Credit: NASA

A century after Carrington's observations, Newton & Nunn (1951) measured the rotation rate of sunspots from 1934 to 1944 (i.e., Sunspot Cycle 17) using the sunspot record of the Royal Greenwich Observatory. They characterized the sidereal rotation rate (ω)with the expression

$$\omega(\lambda) = A + B\sin^2\lambda \tag{2.1}$$

where λ is the latitude with $A = 14.38^\circ day^{-1}$ and $B = 2.96^\circ day^{-1}$. Their measurements were in agreement with those of Carrington. They also compared these results to measurements from the

prior five solar cycles (also based on the Royal Greenwich Observatory record) and found that the differential rotation did not vary (to within the limits of their error measurements) from one cycle to the next, nor over the solar cycle itself. They also noted that the differential rotation was symmetric across the equator, i.e., no hemispheric difference was apparent.

Later observations showed that there were changes in the differential rotation. Howard et al. (1984) measured sunspot position and areas from white light images of the Sun captured on photographic plates by the Mount Wilson Observatory from 1921 to 1982. They found that the rotation rate as measured by tracking sunspot groups was slower ($\sim$ 1%) than as by tracking individual spots. Furtheremore the rotation rate measured by tracking larger spots was slower ($\sim$ 2%) than as measured by tracking smaller spots. Hathaway & Wilson (1990) showed that these relationships translated into a small ($<$ 5%) solar cycle variation of the differential rotation as measured by the motion of sunspots as they transit the Sun.

Direct Doppler measurements of the differential rotation have revealed additional variation. Howard & Labonte (1980) measured the rotation rate using Doppler images from the Mount Wilson Observatory. While measurements made by tracking sunspots are restricted to *active latitudes* (i.e. the region below 40° in which active regions emerge), Doppler measurements can be made at all latitudes. They characterized the rotation rate for each Carrington Rotation with three coefficients $A, B,$ and C such that the rotation rate (ω) is given by

$$\omega(\lambda) = A + B\sin^2\lambda + C\sin^4\lambda \tag{2.2}$$

They calculated the average rotation rate and subtracted this from the rotation rate measured for each rotation. They then plotted the residual rotation as a function of time for the time period from January 1968 to December 1979. They found an oscillating pattern in the residual rotation rate which they referred to as *torsional oscillations*. The excess velocities (with magnitudes of $\sim$ 3m s^{-1}or $\sim$ 1% of the rotation rate) created a chevron-like pattern that alternates between slower and faster zones with a period of about 11 years. Zones started at high latitudes and drifted towards the

equator in about 22 years. For the last half of that period, the poleward boundary of these faster zones coincides with the latitudinal center of sunspot activity for each hemisphere. Furthermore, the exceess velocities paired with the Solar Cycle 21 were faster than those observed for weaker Solar Cycle 20.

In the last few decades, helioseismology has revealed a great deal about the internal structure of the Sun, including the variation of rotation through the convection zone. Thompson et al. (1996) applied helioseismology techniques to data obtained by the Global Oscillation Network Group (GONG). They determined that below the surface the rotation rate increases down to a depth of about $0.95R_{\odot}$ (this region is known as a *surface shear layer*). At a depth of about $0.7R_{\odot}$ (i.e the base of the convection zone), the rotation rates at different latitudes merge and the Sun rotates like a solid body interior to that depth. A second shear layer is present in this transitionary region (known as the *tachocline*). These results have been confirmed by (Schou et al., 1998) using helioseismology on MDI data. Current GONG measurements of the Sun's rotation rate in the interior are shown in Figure 2.3 and Figure 2.4. Finally, Howe et al. (2000) has shown that torsional oscillations extend deep into the convection zone.

2.1.3 Meridional Flow

Babcock (1961) hypothesized the existence of a meridional flow (a.k.a. meridional circulation) and suggested that it could cause magnetic fields to cancel across the equator and also transport the excess flux to the poles. Shortly after, Leighton (1964) discovered the existence of supergranules and suggested that the diffusive random walk motions of the supergranules were sufficient to transport magnetic flux to the poles. It was not until 1982 that Topka et al. (1982) were able to use observations of the motions of polar filaments to infer that a poleward meridional flow with velocities of $\sim$10 m s^{-1} did exist and that these motions could not be explained by diffusion.

Over the next decade and a half, new measurements of the meridional flow began to trickle in. Most measurements were made by using magnetograms to track the motions of different features on the Sun. Some tracked the motions of sunspots or active regions (Howard & Gilman, 1986).

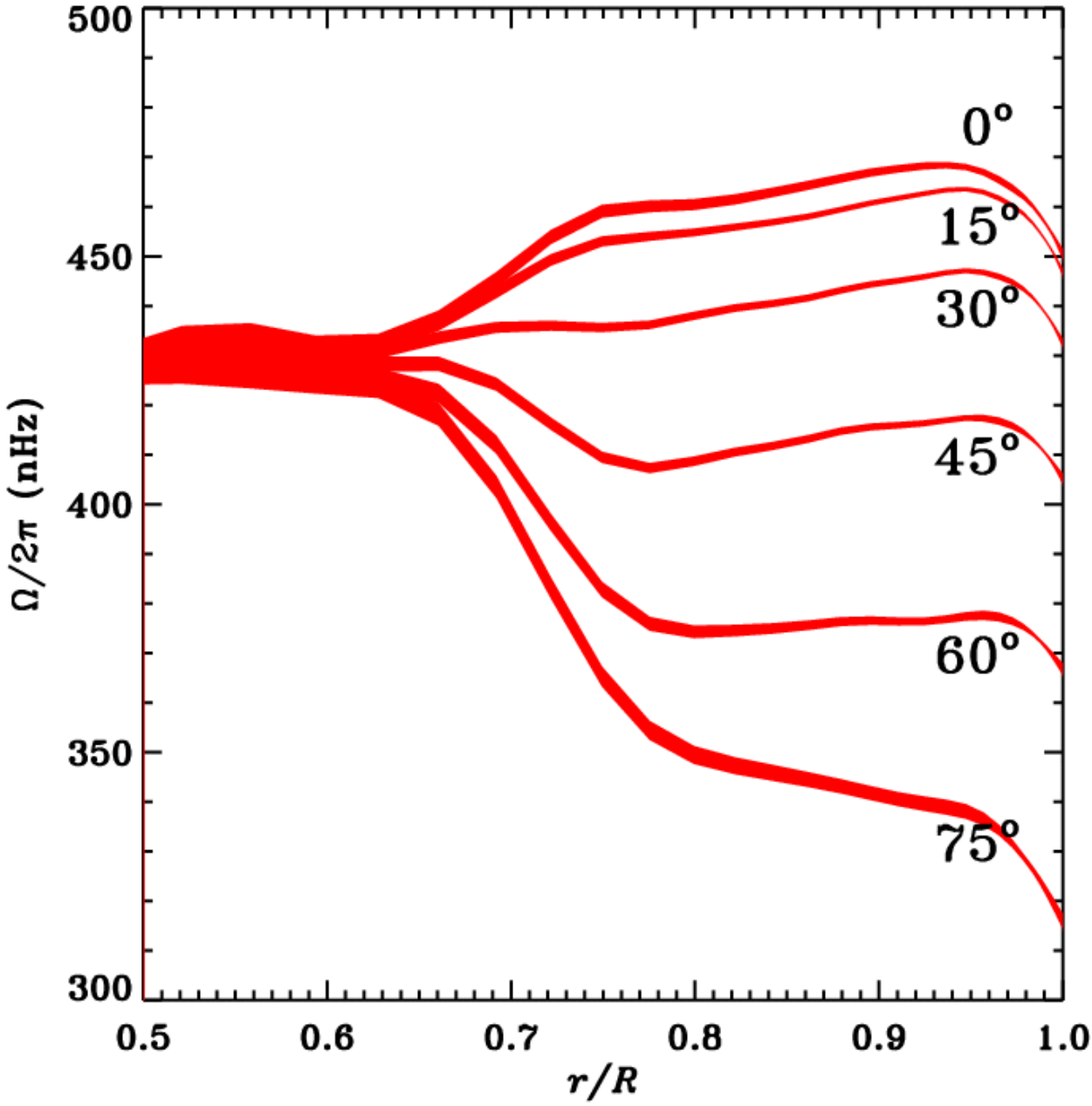

Figure 2.3: Plot of Differential Rotation. Differential rotation is shown as a function of depth. The rotation rate increases just below the surface. These rotation rates converge into solid body rotation at depth of about $0.7R_{\odot}$. Credit: GONG/NSO/AURA/NSF.

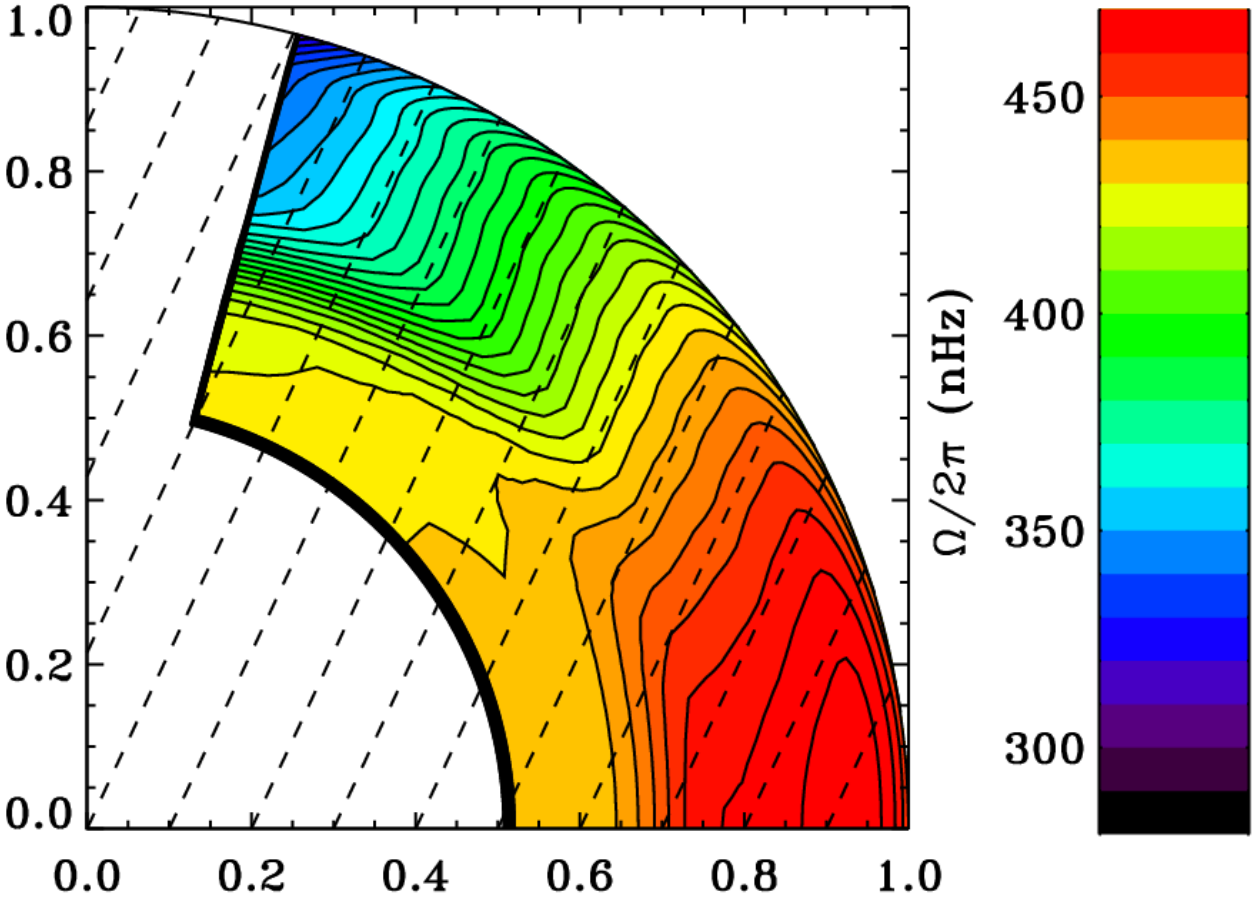

Figure 2.4: Differential Rotation Interior. Differential rotation of the interior is shown as a function of depth. Shear layers (indicated by converging contours) are seen at the surface and at the base of the convection zone. Credit: GONG/NSO/AURA/NSF.

Komm et al. (1993a) and Snodgrass & Dailey (1996) tracked the motions of small magnetic elements. Latushko (1994) tracked large scale patterns in the magnetic fields. Others used the Doppler signal to obtain flow velocities (Ulrich et al., 1988; Hathaway, 1996). However, these results often conflicted in not only the magnitude of the meridional flow, but also the direction.

Around the turn of the millennium, a consensus about the meridional flow began to appear. SOHO was launched in 1995 and housed twelve instruments for studying various aspects of the Sun, including MDI. MDI provided the highest time cadence magnetic data for its time. With better time cadence, measurements using feature tracking methods improved (Meunier, 1999). Further-

more, a new way to study the Sun was born: local helioseismology. While global helioseismology uses spherical harmonics to investigate global modes, local helioseismology examines the propagation of waves over small targeted regions. Local helioseismology, unlike global helioseismology, could be used to measure the meridional flow. Using local helioseismology, Schou & Bogart (1998)found a poleward meridional flow that peaked at 30° latitude with a velocity of 20 m s^{-1} that decreased with depth. Basu & Antia (2003) used local helioseismology to confirm that the amplitude and shape of the meridional flow changes over the course of a solar cycle.

The meridional circulation is now accepted to have a peak velocity between 10-20 m s^{-1} poleward at the surface. While there has been speculation that *counter-cells* (i.e., a cell of meridional circulation with equatorward flows at the surface) might exist at the poles, so far the evidence has been conflicting and their existence is still uncertain. For several decades now, the equatorward meridional return flow was thought to occur at the base of the convection zone. However, recent observations (Hathaway, 2012b; Zhao et al., 2013) have upended this notion, finding that the meridional return flow occurs at depths of around 60 Mm (i.e. 60 x 10^6 meters). This has created a major paradigm shift for dynamo modelers who have depended on the meridional flow to act as a conveyor belt of magnetic flux returning at the base of the convection zone ($\sim 0.7 R_\odot$, or a depth of $\sim$200Mm) to regulate the solar cycle.

Differential rotation and supergranular flows have velocities of hundreds of meters per second, however meridional flow speeds are only on the order of 10-20 m s^{-1}. This has made the meridional flow the most difficult surface flow to measure. While measurements are typically accurate to within 1-2 m s^{-1}, they vary significantly over the cycle and with the measurement technique being used. Each measurement technique is subject to its own limitations. Feature tracking measurements are limited to the latitudes in which the features exist. Doppler measurements are subject to errors if the convective blue shift is not correctly accounted for (Hathaway, 1996). Helioseismology can be used to find velocities for a range of depths, but their measurements have been confined to latitudes below 60° (Basu & Antia, 2010). Furthermore the velocities obtained with different methods are representative of the flows at the depths that the observables correspond to (illustrated

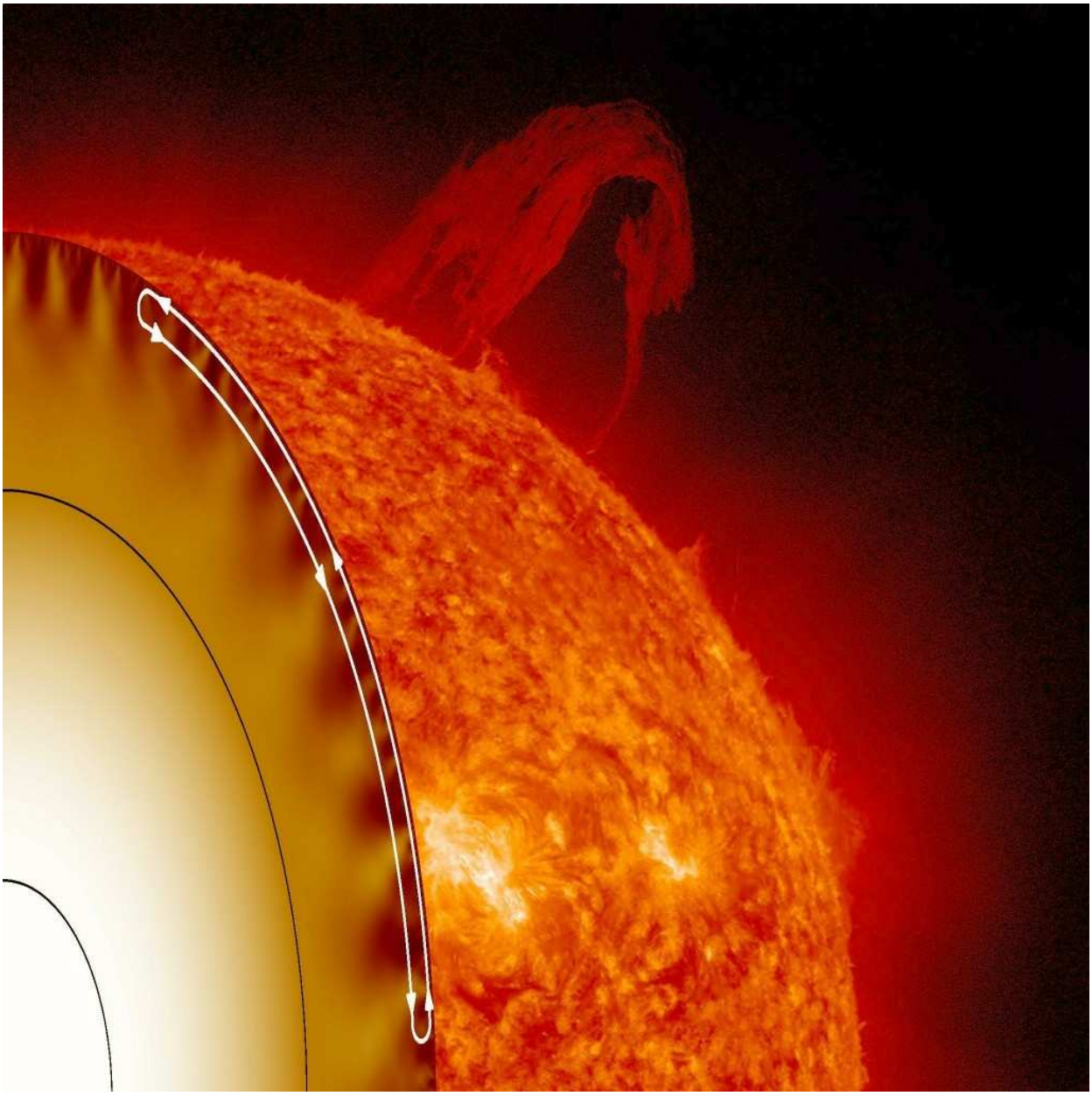

Figure 2.5: Shallow Meridional Flow. Recent observations have shown that the meridional return flow does not occur at the base of the convection zone (as was previously thought) but at a shallow depth of about 60 Mm. Credit: David Hathaway NASA/MSFC.

in Figure 2.6). For example, sunspots are rooted deep in the convection zone and so their velocities are more consistent with the flows of the plasma within the convection zone rather than flows at the surface. A major component of this dissertation (presented in Chapter 3) will be to characterize the meridional flow and its variability using feature tracking of small magnetic elements on MDI and HMI data from 1996 to present.

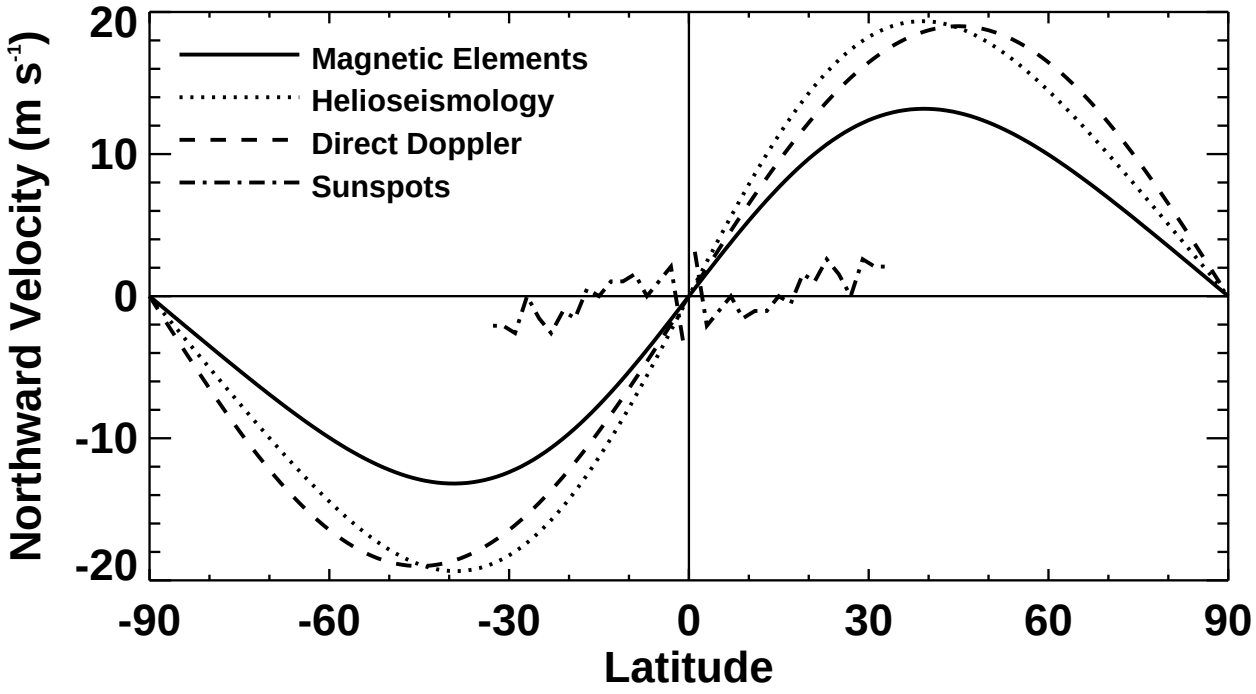

Figure 2.6: Meridional Flow Comparison. This plot compares the meridional flow as measured by different techniques. The solid line shows the flow as measured by feature tracking (Komm et al., 1993a). The dotted line shows the flow for 2008 as measured by helioseismology (Basu & Antia, 2010). The dashed line shows the flow for 1995 as measured by Direct Doppler (Hathaway, 1996). The dash-dot line shows the flow as measured by tracking sunspot motions (Tuominen & Kyrolainen, 1982).

2.2 Solar Flux Transport Models

Virtually all solar dynamo models can be broken into two fundamental processes (Parker, 1955; Babcock, 1961; Charbonneau, 2010):

1. The conversion of the Sun's poloidal magnetic field (at solar minimum) into toroidal field that creates sunspots.

2. The conversion of the toroidal magnetic field into poloidal magnetic field with the polarity opposite to the original poloidal field.

These models can be divided into two fundamental regimes: Dynamo models and the Surface Flux Transport models. The Dynamo models attempt to reproduce both of these processes. For example, Flux Transport Dynamo models (Dikpati & Charbonneau, 1999) portray the Sun as a conveyor belt of sunspot cycles. These type of models have been used for solar cycle prediction (Dikpati et al., 2006; Choudhuri et al., 2007). Surface Flux Transport models (DeVore et al., 1984; Wang et al., 1989; van Ballegooijen et al., 1998; Schrijver & Title, 2001) look exclusively at the second process, i.e, how magnetic flux moves at the surface as a function of latitude and longitude. These models create a picture of the flux over the entire surface of the Sun. They can be used to explain the polar field reversals and their predictions have served as the inner boundary condition for solar wind models as well as models used to make space weather predictions.

In Chapter 4, I introduce a new Surface Flux Transport model that will be used to investigate the role that flux transport plays in the Sun's activity cycle by modeling the second process (i.e. the conversion of the toroidal field into poloidal field with the opposite polarity). In this process, magnetic flux emerges in active regions with a characteristic tilt, i.e., Joy's Law tilt (Hale et al., 1919; Howard, 1991), and is then shredded off into the surrounding plasma. The lower latitude leading polarity flux cancels across the equator and the surface flows transport the higher latitude following polarity flux to the poles. The following polarity cancels with the original poloidal fields and creates new poloidal fields with opposite polarity. In this chapter, I will review the physics (Section 2.2.1) and history (Section 2.2.2) of Surface Flux Transport models.

2.2.1 Surface Flux Transport Equations

Magenetohydrodynamics (MHD), the basis of plasma physics, is a system of equations that combine fluid mechanics with Maxwell's equations in order to treat plasma as a conducting fluid. The equations of surface flux transport are borne out of MHD and the underlying assumptions therein. In this section, I discuss these assumptions and derive the surface flux transport equation beginning with Maxwell's equations

$$\nabla \times \mathbf{B} = \mu \mathbf{j} + \frac{1}{c^2}\frac{\partial \mathbf{E}}{\partial t} \tag{2.3}$$

$$\nabla \cdot \mathbf{B} = 0 \tag{2.4}$$

$$\nabla \times \mathbf{E} = -\frac{\partial \mathbf{B}}{\partial t} \tag{2.5}$$

$$\nabla \cdot \mathbf{E} = \frac{1}{\varepsilon}\rho \tag{2.6}$$

and Ohm's Law

$$\mathbf{j} = \sigma\left(\mathbf{E} + \mathbf{v} \times \mathbf{B}\right). \tag{2.7}$$

One of the governing assumptions of *ideal MHD*, is that the plasma is electrically neutral and perfectly conducting. Under this assumption displacement currents become negligible. Starting with equation (2.5) we have

$$\nabla \times \mathbf{E} = -\frac{\partial \mathbf{B}}{\partial t} \Rightarrow \frac{E}{L} \approx \frac{B}{\tau} \tag{2.8}$$

where τ is the characteristic time scale and L is the characteristic length scale. So

$$\frac{1}{c^2}\frac{\partial \mathbf{E}}{\partial t} \approx \frac{LB}{c^2\tau^2} \tag{2.9}$$

and with velocity of the plasma given by

$$v \propto \frac{L}{\tau} \tag{2.10}$$

we now have

$$\frac{1}{c^2}\frac{\partial \mathbf{E}}{\partial t} \approx \frac{v^2}{c^2}\frac{B}{L}. \tag{2.11}$$

Now

$$\nabla \times \mathbf{B} \propto \frac{B}{L}, \tag{2.12}$$

so if $\frac{v^2}{c^2} \ll 1$ we can neglect the last term in (2.3), i.e., the displacement currents. Therefore under ideal MHD, (2.3) becomes

$$\nabla \times \mathbf{B} = \mu \mathbf{j}. \tag{2.13}$$

Next we derive the induction equation (i.e., the time evolution of the magnetic field) ($\frac{\partial \mathbf{B}}{\partial t}$). We begin by putting Ohm's law (2.7) into equation (2.13) to get

$$\nabla \times \mathbf{B} = \mu\sigma\left(\mathbf{E} + \mathbf{v} \times \mathbf{B}\right) \tag{2.14}$$

and take the curl of both sides to get

$$\nabla \times \nabla \times \mathbf{B} = \mu\sigma\left(\nabla \times \mathbf{E} + \nabla \times \mathbf{v} \times \mathbf{B}\right) \tag{2.15}$$

which can be rewritten as

$$\nabla \times \mathbf{v} \times \mathbf{B} - \frac{1}{\mu\sigma}\nabla \times \nabla \times \mathbf{B} = -\nabla \times \mathbf{E} = \frac{\partial \mathbf{B}}{\partial t}. \tag{2.16}$$

Applying the following identity

$$\nabla \times \nabla \times \mathbf{B} = \nabla (\nabla \cdot \mathbf{B}) - \nabla^2 \mathbf{B} = -\nabla^2 \mathbf{B} \tag{2.17}$$

we can write $\frac{\partial \mathbf{B}}{\partial t}$ as

$$\frac{\partial \mathbf{B}}{\partial t} = \nabla \times \mathbf{v} \times \mathbf{B} - \eta \nabla^2 \mathbf{B} \tag{2.18}$$

where $\eta = \frac{1}{\sigma \mu}$. The first term on the right is the convective term and the last term is the diffusive term. The ratio of the magnitudes of these terms is known as the magnetic Reynolds number, R_m.

$$R_m = \frac{|\nabla \times \mathbf{v} \times \mathbf{B}|}{|\eta \nabla^2 \mathbf{B}|} = \frac{vL}{\eta}. \tag{2.19}$$

In the case of $R_m \ll 1$, diffusion dominates, and for $R_m \gg 1$, convection dominates. In the case where $R_m \gg 1$, the magnetic field is considered to be *frozen* into the plasma, i.e., the two are inseparable. In the Sun, molecular diffusion is on the order of 10^3 m^2 s^{-1} at the photosphere. Granules 2.1.1 have velocities of $\sim 10^3$ m s^{-1} and sizes of $\sim 10^6$ m . These values give a $R_m \approx 10^6$ for the Sun, i.e. $R_m \gg 1$ and the magnetic field are frozen into the plasma. Plasma beta, β is the ratio of the gas pressure to the magnetic pressure

$$\beta = \frac{P}{B^2/2\mu_0} = \frac{nkT}{B^2/2\mu_0}. \tag{2.20}$$

This ratio is a metric for determining whether the magnetic fields or the plasma governs the fluid motions. When $\beta \ll 1$, the magnetic fields move the plasmas and when $\beta \gg 1$, the plasmas move the magnetic fields.

We now move into *mean field MHD*, in which we derive the global induction equation, i.e., the *flux transport equation*. We decompose the magnetic field and the velocity into average components (the large scale magnetic field $\langle \mathbf{B} \rangle$ and the global flows $\langle \mathbf{v} \rangle$) and fluctuating components ($\delta \mathbf{B}$

and $\delta\mathbf{v}$) and put these into the induction equation (2.18) to obtain

$$\frac{\partial \langle \mathbf{B} \rangle}{\partial t} + \frac{\partial \delta \mathbf{B}}{\partial t} = \nabla \times \langle \mathbf{v} \rangle \times \langle \mathbf{B} \rangle + \nabla \times \langle \mathbf{v} \rangle \times \delta \mathbf{B} + \nabla \times \delta \mathbf{v} \times \langle \mathbf{B} \rangle + \nabla \times \delta \mathbf{v} \times \delta \mathbf{B} - \eta \nabla^2 \langle \mathbf{B} \rangle . \tag{2.21}$$

Taking the ensemble average ($\langle\rangle$) of the induction equation (2.18) gives

$$\frac{\partial \langle \mathbf{B} \rangle}{\partial t} = \nabla \times \langle \mathbf{v} \rangle \times \langle \mathbf{B} \rangle + \nabla \times \langle \delta \mathbf{v} \times \delta \mathbf{B} \rangle . \tag{2.22}$$

In the last term, $\langle \delta \mathbf{v} \times \delta \mathbf{B} \rangle$ is the *mean electromotive force*, is the workhorse of dynamo theory. If $\delta\mathbf{v}$ and $\delta\mathbf{B}$ are unrelated, this term goes to 0 and there is no dynamo. Next, we subtract equation (2.22) from equation (2.21) to arrive at

$$\frac{\partial \delta \mathbf{B}}{\partial t} = \nabla \times \langle \mathbf{v} \rangle \times \delta \mathbf{B} + \nabla \times \delta \mathbf{v} \times \langle \mathbf{B} \rangle + \nabla \times \delta \mathbf{v} \times \delta \mathbf{B}. \tag{2.23}$$

The magnetic fluctuations $\delta\mathbf{B}$ are assumed to be small compared to $\langle\mathbf{B}\rangle$, so the first and third terms on the right have side are neglected, giving the approximation

$$\delta \mathbf{B} \approx \tau \left(\nabla \times \delta \mathbf{v} \times \langle \mathbf{B} \rangle \right) . \tag{2.24}$$

Substituting this into the equation for the mean electromotive force, it can be shown (with some work and some assumptions) that

$$\nabla \times \langle \delta \mathbf{v} \times \delta \mathbf{B} \rangle \approx \tau \nabla \times \langle \delta \mathbf{v} \times \nabla \times (\delta \mathbf{v} \times \langle \mathbf{B} \rangle) \rangle = \eta_T \nabla^2 \langle \mathbf{B} \rangle \tag{2.25}$$

where $\eta_T \propto \tau |\delta v|^2$ is the *turbulent diffusivity*. In the case of granules

$$\eta_T = 6 \times 10^2 \text{ s} \cdot \left(3 \times 10^3 \text{ m s}^{-1} \right)^2 \approx 5 \times 10^9 \text{ m}^2 \text{s}^{-1} \tag{2.26}$$

The *mean field flux transport equation* can then be written as

$$\frac{\partial \langle \mathbf{B} \rangle}{\partial t} = \nabla \times \langle \mathbf{v} \rangle \times \langle \mathbf{B} \rangle + \eta_T \nabla^2 \langle \mathbf{B} \rangle . \tag{2.27}$$

For surface flux transport, we are only interested in the horizontal transport of the radial magnetic fields. We now write (2.27) as

$$\frac{\partial B_r}{\partial t} = \nabla \times \mathbf{v} \times B_r + \eta_T \nabla^2 B_r. \tag{2.28}$$

In spherical coordinates

$$\mathbf{v} \times B_r = -v_\theta B_r \hat{e_\phi} + v_\phi B_r \hat{e_\theta} \tag{2.29}$$

so, equation (2.28) becomes the *surface flux transport equation*

$$\frac{\partial B_r}{\partial t} = -\frac{1}{r \sin\theta} \frac{\partial}{\partial \theta} \left(v_\theta B_r \sin\theta \right) - \frac{1}{r \sin\theta} \frac{\partial}{\partial \phi} \left(v_\phi B_r \right) + \eta_T \nabla^2 B_r. \tag{2.30}$$

2.2.2 Surface Flux Transport Models

Babcock (1961) painted a picture of the solar dynamo based on his observations of the Sun (see Section 1.3.1). In this picture, he described the transport of higher latitude following polarity flux to the poles, and proposed a meridional flow (see section 2.1.3) as the transport mechanism. Leighton (1964), having discovered supergranules, suggested that the diffusive motion of supergranules was sufficient to account for the poleward transport. Mosher (1977) attempted to quantify the transport due to supergranular diffusion on the Sun, and found that it was too weak to account for the poleward transport. He suggested that both supergranular diffusion and meridional flow were needed.

DeVore et al. (1984) created the first Surface Flux Transport model of Sun. At the time of their work, the meridional flow was difficult to measure and measurements that did exist were

very uncertain. They hoped to use flux transport to help constrain this flow, whose existence was controversial at the time. They derived equation (2.28) from the MHD equations by assuming no sources, that the magnetic field is largely radial, and that the turbulent convective motions can be represented by a diffusivity coefficient. In their model, they investigated a large scale axisymmetric magnetic field $B(\theta,t)$ (rather than $B(\theta,\phi,t)$) that is not effected by the differential rotation. Their Surface Flux Transport equation was

$$\frac{\partial B_r}{\partial t} + \frac{1}{R\sin\theta}\frac{\partial}{\partial\theta}(B_r v(\theta)\sin(\theta)) = \frac{\eta}{R^2\sin\theta}\frac{\partial}{\partial\theta}\left(\sin\theta\frac{\partial B_r}{\partial\theta}\right) \tag{2.31}$$

where R is the radius of the Sun, θ is the angle from the pole and $v(\theta)$ is the meridional flow. Solving this equation analytically and numerically they found a meridional flow of the form

$$v(\theta) = -v_0\sin\theta\tanh(40\cos\theta) \tag{2.32}$$

where v_0 is a normalization factor, produced polar fields that best matched the observations.

Sheeley et al. (1985) modified equation (2.28) to create a Surface Flux Transport model that simulated flux transport on the entire surface of the Sun and included bipolar active region sources. Their flux transport equation was

$$\begin{aligned}\frac{\partial B}{\partial t} = &-\omega(\theta)\frac{\partial B}{\partial\phi} - \frac{1}{R\sin\theta}\frac{\partial}{\partial\theta}(Bv(\theta)\sin(\theta)) + \\ &\frac{\kappa}{R^2}\left[\frac{1}{\sin\theta}\frac{\partial}{\partial\theta}\left(\sin\theta\frac{\partial B}{\partial\theta}\right) + \frac{1}{\sin^2\theta}\frac{\partial^2 B}{\partial\phi^2}\right] + S(\theta,\phi,t)\end{aligned} \tag{2.33}$$

where ϕ is the longitude, $\omega(\theta)$ is the rotation, and $S(\theta,\phi,t)$ is the active region source term. They initialized the simulation with a National Solar Observatory *synoptic map*. This is a map of the Sun's magnetic surface constructed by splicing together the magnetic fields observed daily near the central meridian over the course of a Carrington rotation. The source term was simulated by adding in doublets based on the observations of $\sim$2500 bipolar active regions as seen in magnetograms taken at the National Solar Observatory at Kitt Peak. These doublets included observed latitudinal

and longitudinal separations. The magnitude of both polarities was assumed to be equal and opposite and was set based on the magnitude of the observed leading polarity spot. The diffusivity, rotation rate, and meridional flow were treated as adjustable parameters.

They simulated the evolution of the magnetic field from 1976 to 1984. At each time step of one day, they calculated the mean field and compared it with the mean field as measured by using the Wilcox Solar Observatory data. The found that the diffusivity, rotation rate, and meridional flow acted together to dissipate the flux from the active region sources. They also found that the sixteen largest active region sources had a huge effect on the evolution of the mean field, while the 1498 smallest active region sources had virtually no effect of the mean field evolution.

Wang et al. (1989) used the same Surface Flux Transport model to simulate the magnetic field evolution from 1976 to 1986. They modified the differential rotation, meridional flow, and diffusion parameters to further investigate the role the each played in reversing the polar fields. They found that diffusion was essential for separating the leading and following polarity flux in bipolar active regions and for creating cancellation of flux across the equator. They found that the meridional flow was essential for transporting the following polarity flux to the poles and keeping it concentrated there (in opposition to the diffusive effect of the supergranular flows). They concluded that a meridional flow must be present on the Sun and suggested that it varied over Solar Cycle 21 such that it was faster at solar maximum and slower late in the cycle.

The Surface Flux Transport model was extend into the corona by van Ballegooijen et al. (1998) by adding in horizontal transport of magnetic flux. The velocities in the corona were extrapolated from the surface flows, such that

$$\begin{aligned} v_r &= 0 \\ v_\theta &= u(\theta) r / R_\odot \\ v_\phi &= r \sin\theta \Omega(\theta) \end{aligned} \tag{2.34}$$

where the differential rotation, $\Omega(\theta)$, was given in deg day^{-1} by

$$\Omega(\theta) = 13.38 - 2.3cos^2\theta - 1.62\cos^4\theta - \Omega_0 \tag{2.35}$$

where Ω_0 is the Carrington rotation rate. The meridional flow was given by

$$u(\lambda) = -u_0 \sin(\pi\lambda/\lambda_0) \qquad \text{for} |\lambda| < \lambda_0 \tag{2.36}$$

where λ is latitude ($\lambda \equiv \pi/2 - \theta$) and with $\lambda_0 = 75^\circ$ and $u_0 = 11$m s^{-1}. The meridional flow was taken to be 0 above λ_0. They simulated the evolution of the magnetic field for two solar cycles and were able to produce polar fields with magnitudes that agreed with observations. However, they found discrepancies in the orientation of the magnetic field.

Surface Flux Transport models have also been used to simulate flux transport on Sun-like stars (Schrijver & Title, 2001). They recognized that the magnetic fields in active regions inhibit the diffusive effects of the supergranular motion (i.e., large active regions do not disperse as quickly as small active regions). To account for this, they used a Lagrangian Surface Flux Transport model that tracked the motions of the individual magnetic flux elements rather than an Eulerian model that solves for flows on a grid. The diffusivity was given as a function of the magnetic element strength. The differential rotation was given by the measurements of (Komm et al., 1993b). The meridional flow at flow latitude was given by (Komm et al., 1993a), but was tapered off at high latitudes. By using an amplified (flux density of ~ 10 times that of the Sun) 11-year sunspot cycle, they were able to produce strong polar caps that were consistent with the formation of high latitude starspots that have been observed on other stars.

CHAPTER 3

MEASURING FLOWS

In this dissertation, I investigate the evolution of the Sun's magnetic fields using a surface flux transport model. Ideally, a transport model should be able to reproduce the magnetic field evolution at the surface by incorporating the observed flows. In this chapter I will discuss the measurement of the flows that transport flux near the surface of the Sun. This includes the axisymmetric flows (Section 3.1) and turbulent flows due to convective motions (Section 3.2. Then, in Chapter 4, I introduce a purely advective surface flux transport model that incorporates those observations.

3.1 Axisymmetric Flows

The axisymmetric flows include differential rotation (Section 2.1.2) and meridional flow (Section 2.1.3). While the differential rotation has been well described, the meridional flow has been more elusive, particularly at the poles. However, the meridional flow at high latitudes has significant consequences for models of the Sun's magnetic dynamo. Models of the magnetic flux transport at the Sun's surface (van Ballegooijen et al., 1998; Schrijver & Title, 2001; Wang et al., 2009) have employed meridional flow profiles which either stop completely at 75° latitude or quickly fall to zero before entering the polar regions. Flux Transport Dynamo models depend critically on the strength and structure of the meridional circulation. With assumptions about the meridional circulation, these models have been used to predict the amplitude and timing of Solar Cycle 24 (Dikpati et al., 2006; Choudhuri et al., 2007). The presence or absence of counter-cells in the meridional flow at high latitudes has been shown to alter the length of the sunspot cycle in these models (Dikpati et al., 2010).

Previous measurements of the meridional motion of the magnetic elements have been limited to lower latitudes. Komm et al. (1993a) limited their measurements to latitudes less than 52.5°.

Meunier (1999) included measurement to 70°. Measurements of the meridional flow using the methods of helioseismology have been limited to latitudes below 50° (González Hernández et al., 2010; Basu & Antia, 2010). While direct Doppler measurements can conceivably measure the meridional flow right to the poles (Ulrich, 2010), these measurements are subject to systematic errors from the Convective Blue Shift signal (an apparent blue shift of spectral lines due to the correlation between emergent intensity and radial velocity in convective flows at the surface).

In this Section, I discuss our measurements of the axisymmetric flow velocities, especially the meridional flow, at the highest latitudes possible for Solar Cycle 23 and the rise of Solar Cycle 24 (from 1996 to 2013.) We measured these flows by using a cross-correlation technique on magnetograms to determine the motion of small magnetic elements on the surface of the Sun. The magnetograms were obtained by two different instruments: the MDI instrument on board SOHO and the HMI instrument on board SDO (Scherrer et al., 1995, 2012). Our MDI results have been published in Hathaway & Rightmire (2010, 2011) and our HMI results were published in Rightmire-Upton et al. (2012).

3.1.1 MDI Analysis

The MDI instrument obtained full-disk magnetograms with a resolution of 1024x1024 and at a cadence of 96 minutes. This instrument was in operation from May 1996 to March of 2011, with an interruption during the "SOHO summer Vacation," beginning in June 1998. Though MDI resumed observations in October of 1998, these data were not reliable until February 1999. We used all available MDI full-disk magnetograms (excluding June 1998 to February 1999) at a cadence of 96 minutes.

The magnetic fields measured by the magnetograms represent the line of sight magnetic field. The network field outside of active regions consists of small (100 - 300 km) magnetic elements with vertical magnetic fields of up to $\sim$ 1200 Gauss (Stenflo, 1973; Spruit, 1979). We account for the radial nature of these magnetic elements by dividing the line-of-sight signal by the cosine of the heliographic angle from disc center (Svalgaard et al., 1978). The resulting magnetograms were

then mapped into heliographic coordinates,(i.e., Sun-centered and equally spaced in latitude and longitude).

Sunspots, with strong magnetic fields, have been shown to have flows that are not representative of the surface axisymmetric flows (this was illustrated in Figure 2.6) and therefore we have excluded regions with strong fields from the analysis. For MDI this was done by masking out all pixels where |B|>500 G as well as any nearby pixels (within 5 pixels) where |B|>100 G. Figure 3.1 shows an example of a MDI mapped image with active regions masked out.

The 1024x1024 MDI magnetic maps were divided into 11x601 pixel strips, one for every single pixel latitude position. Each strip was then cross-correlated with corresponding strips from 8 hours later (no measurements were taken if the shifted strips extended beyond the mapped data). Measurements were typically obtained for $\sim$ 400 image pairs for each 27-day rotation of the Sun, and for over 60,000 image pairs during the entire MDI era. These measurements were averaged over each rotation to obtain differential rotation (relative to the sidereal Carrington rotation rate of 14.184 deg day^{-1}) and meridional flow profiles for each of 178 Carrington rotations.

The axisymmetric profiles were then fit to polynomials in $\sin\lambda$ (described in the next section in more detail). The polynomial coefficients were plotted as a function of time revealing a persistent north-south flow. While transitory north-south asymmetries are common place on the Sun, a persistent asymmetry is an indication of an error in the geometry (e.g. a small rotational misalignment would cause the differential rotation to appear as a cross-equator meridional flow). This north-south asymmetry could be minimized by applying a 0.21° counterclockwise correction to the position angle (i.e., the angle of the instrument with respect to Sun's rotation axis).

Once this correction was applied, a second weak signal became apparent: an annual signal in the cross equator flow. This signal is illustrated in Figure 3.2. This signal could be removed with a 0.08° decrease in the tilt of the Sun's rotational axis with respect to the plane of Earth's orbit. This value has been accepted as being 7.25° for the last 150 years. However these results (and similar results of Beck & Giles (2005)) suggest this value should be revised as 7.17°.

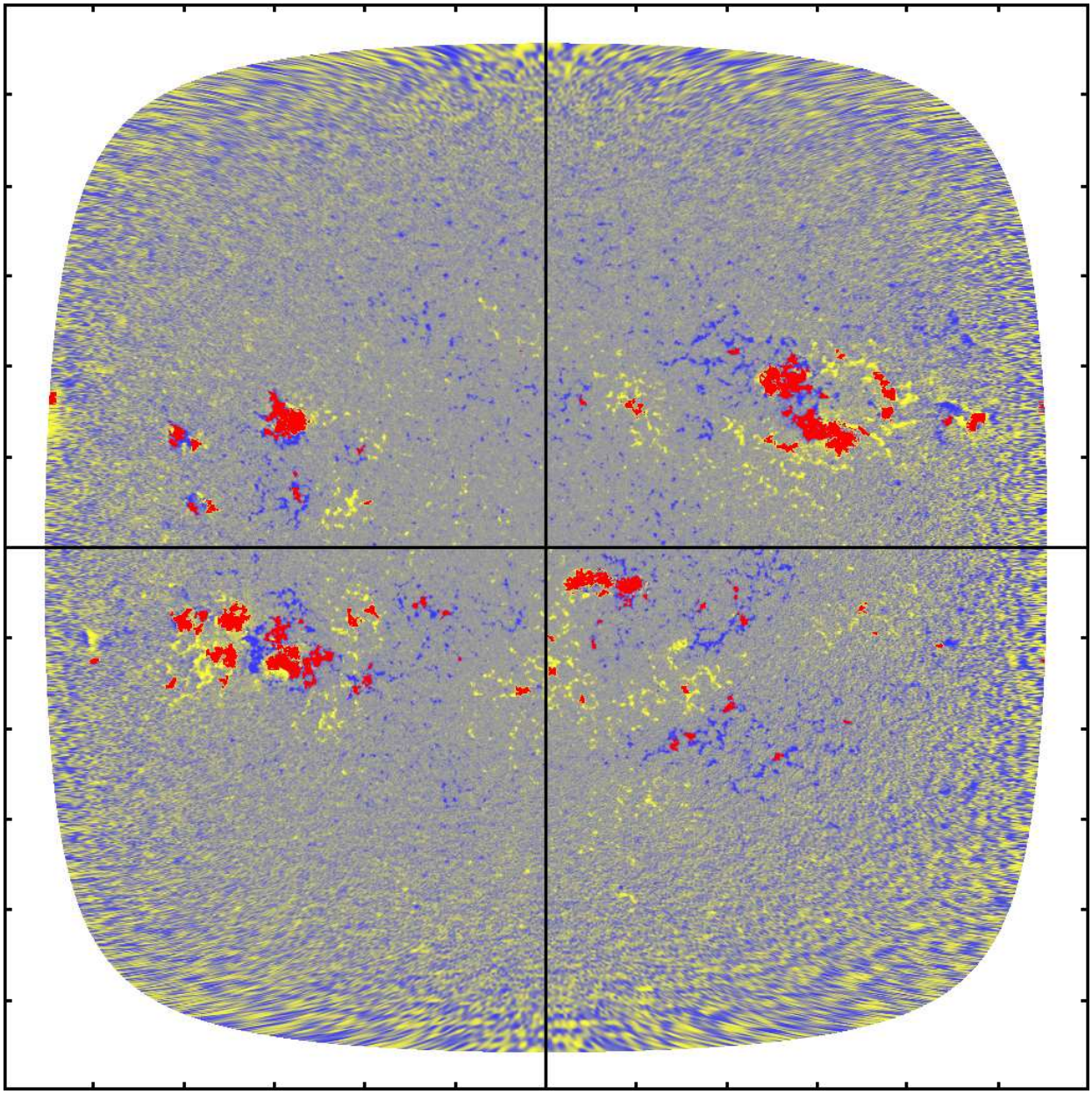

Figure 3.1: A MDI magnetogram from 2001 June 5 at 04:48 U.T. mapped into heliographic coordinates from pole to pole and $\pm 90^{\circ}$ from the central meridian and with a resolution of 1024^2. Yellow represents positive polarity, blue represents negative polarity, and the red regions are the masked active regions.

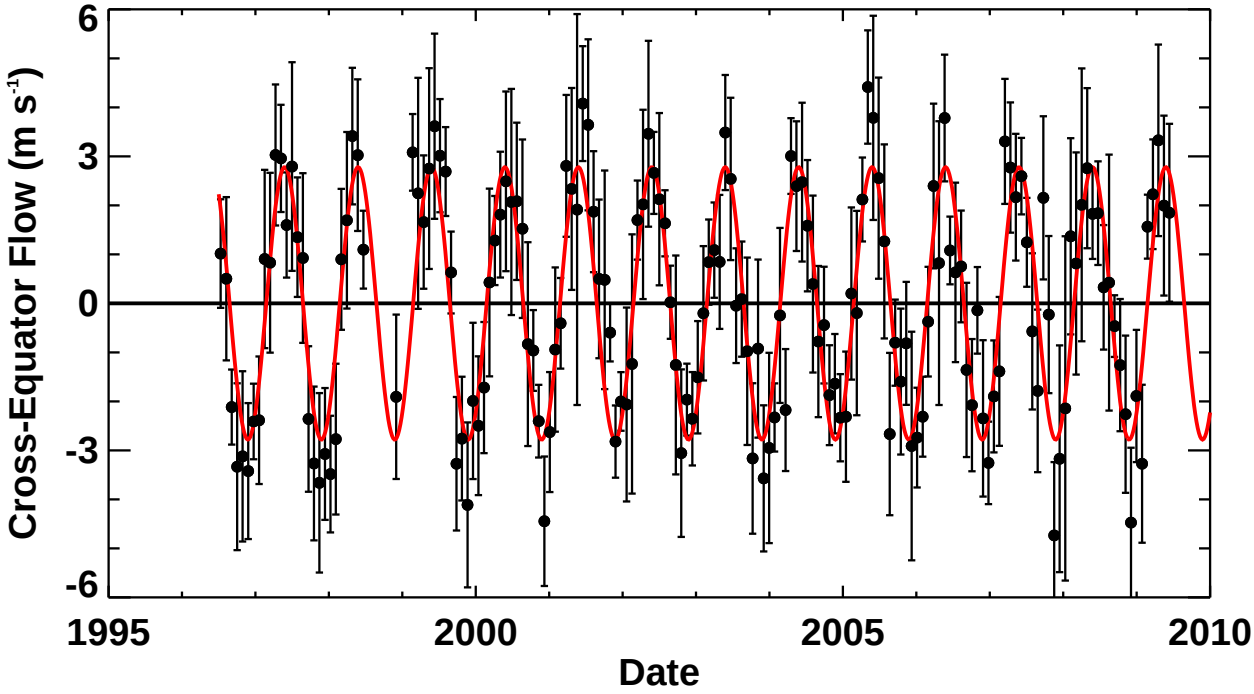

Figure 3.2: Annual Signal in Cross Equator Flow. The amplitude of the cross-quator flow is plotted with 2σ errors. The signal produced by a 0.08° error in the tilt of the Sun's equatorial plane with respect to the plane of the Earth's orbit is shown in red.

3.1.2 MDI Results

We have characterized the axisymmetric flows using magnetic feature tracking for May 1996 to March of 2011, with an interruption from June 1998 until February 1999. We determined the average differential rotation using all of the MDI data. This profile was fit to a fourth-order polynomial in sin λ (shown in Figure 3.3), where λ is the heliographic latitude . The average symmetric differential rotation is given by

$$v_\phi(\lambda) = [a + b\sin^2(\lambda) + c\sin^4(\lambda)]\cos(\lambda) \tag{3.1}$$

with

$$
\begin{aligned}
a &= 35.6 \pm 0.1 \text{ m s}^{-1} \\
b &= -208.6 \pm 1.1 \text{ m s}^{-1} \\
c &= -420.6 \pm 1.6 \text{ m s}^{-1}
\end{aligned}
\tag{3.2}
$$

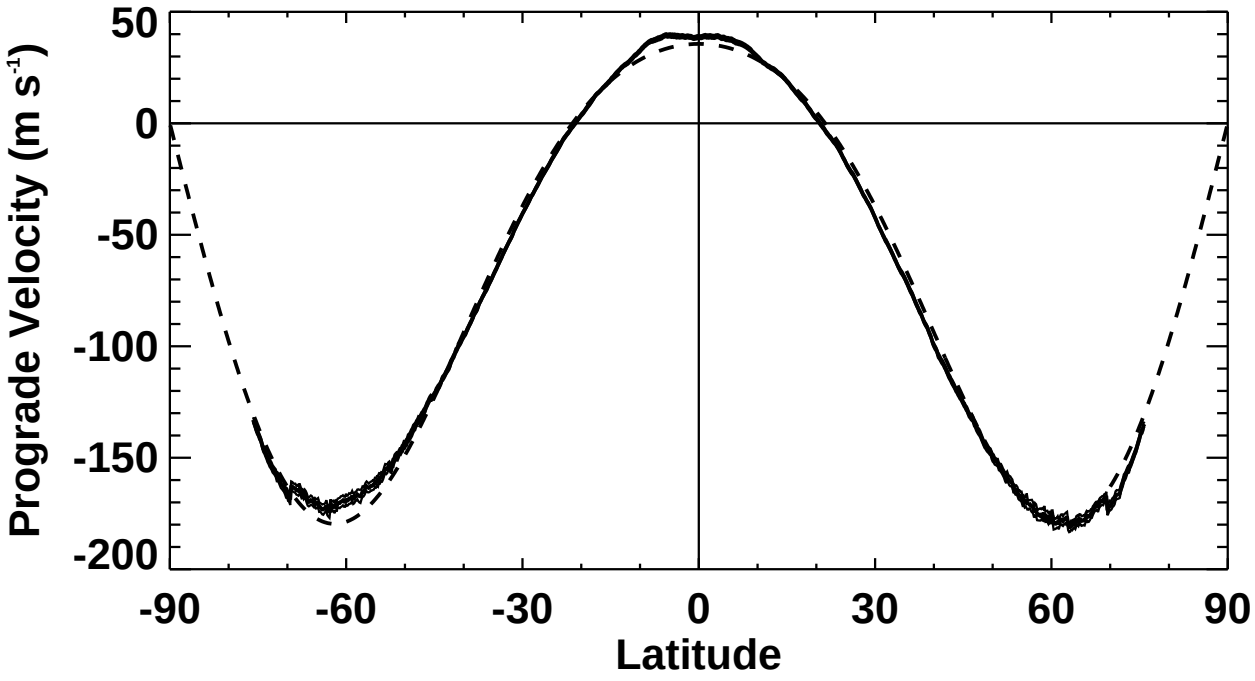

Figure 3.3: The MDI Average Differential Rotation from 1996-2010. The MDI result with 2σ errors is plotted in black and the symmetrized profile represented by equations (3.1), (3.2) is shown with the dashed line.

A comparison of the average differential rotation with the fit to a symmetric differential rotation shows a slight asymmetry: weaker in the south and stronger in the north. We find a flattening of the differential rotation at the equator with a slight dimpling. A similar feature has been observed with earlier measurements of the differential rotation via direct Doppler measurements (Howard et al.,

1980) and magnetic feature tracking (Snodgrass, 1983).

Similarly, we obtained the average axisymmetric meridional flow (Figure 3.4), which is given by

$$v_\theta(\lambda) = [d\sin + e\sin^3(\lambda)]\cos(\lambda) \tag{3.3}$$

with

$$\begin{aligned} d &= 29.7 \pm 0.3 \text{ m s}^{-1} \\ e &= 17.7 \pm 0.7 \text{ m s}^{-1} \end{aligned} \tag{3.4}$$

We find that the average meridional flow possesses a significant asymmetry. The flow is stronger in the south and weaker in the north. More importantly, the meridional flow in the north reaches zero at the edge (75°) of our measurements, suggesting the possibility of a polar counter-cell in the north. The meridional flow in the south appears to continue all the way to the pole.

We have fit the flow profiles to associated Legendre polynomials of order 1 (and normalized to 1.0 or -1.0) in order to investigate the long term variability of the axisymmetric flows. These polynomials are:

$$\begin{aligned} P_1^1 &= \cos\lambda \\ P_2^1 &= 2\sin\lambda\cos\lambda \\ P_3^1 &= \sqrt{\frac{135}{256}}(5\sin^2\lambda - 1)\cos\lambda \\ P_4^1 &= 0.947(7\sin^3\lambda - 3\sin\lambda)\cos\lambda \\ P_5^1 &= 0.583(21\sin^4\lambda - 14\sin^2\lambda + 1)\cos\lambda \end{aligned} \tag{3.5}$$

The coefficients that multiply each component represent the peak velocity of that component. The orthogonal nature of Legendre polynomials ensure that any coupling between two components is physical and not mathematical in nature (Snodgrass, 1984).

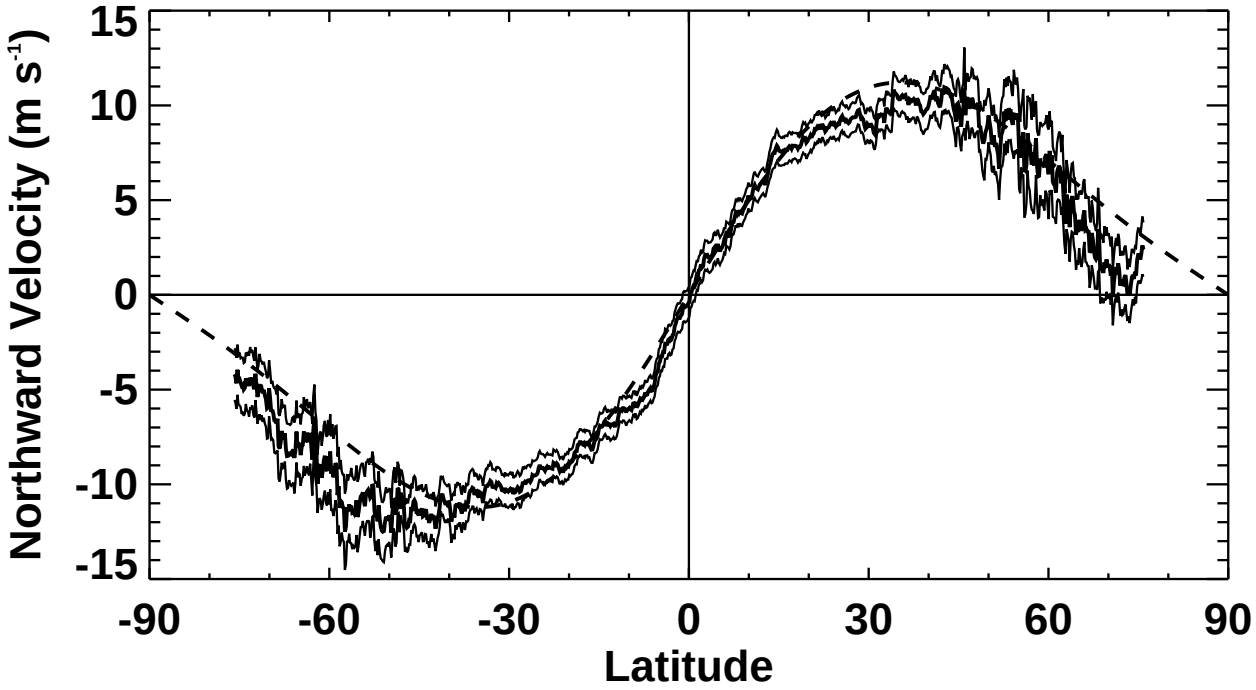

Figure 3.4: The MDI Average Meridional Flow from 1996-2010. The MDI result with 2σ errors is plotted in black and the symmetrized profile represented by equations (3.3),(3.4) is shown with the dashed line. The weaker flow in the north is suggestive of a polar counter-cell.

The coefficients for the differential rotation are T0,T2, and T4 such that T0 multiplies P_1^1, T2 multiplies P_3^1, and T4 multiplies P_5^1. These coefficients are plotted in Figure 3.5. For reference the smoothed sunspot number divided by 4 is also shown. We find that very little variation (only a few percent) is seen in the differential rotation associated Legendre polynomial coefficients. We do find a bowing of the coefficients that indicates a slight weakening (flattening) of the differential rotation near the time of solar maximum ($\sim$2002). A similar effect was observed for Solar Cycle 21 by Komm et al. (1993b).

The coefficients for the meridional flow are S1 and S3 such that S1 multiplies P_2^1 and S3 multiplies P_4^1. These coefficients are plotted in Figure 3.6. For reference the smoothed sunspot number divided by 20 is also shown. We find that the meridional flow coefficients show substantial variability over the solar cycle. The meridional flow is stronger at solar minimum and weaker at solar maximum. A similar effect was observed for Solar Cycle 21 by Komm et al. (1993a).

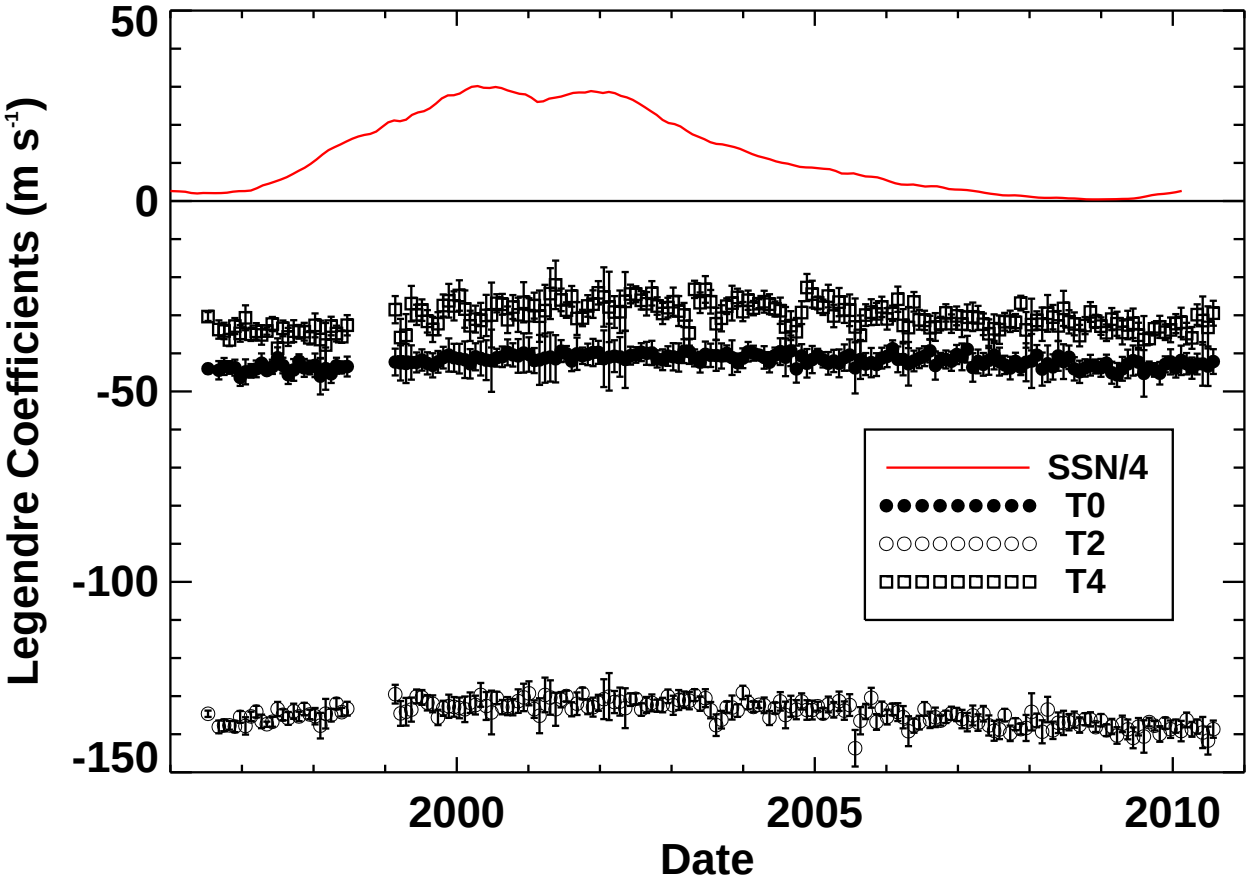

Figure 3.5: Legendre Coefficients used to represent the MDI Differential Rotation. These coefficients can be used with the polynomials given by (3.5) to represent the differential rotation. T0 multiplies P_1^1, T2 multiplies P_3^1, and T4 multiplies P_5^1. For reference the smoothed sunspot number divided by 4 is shown in red.

In addition to the variability seen over the cycle, these results also show a variability from one cycle to the next. We find that the meridional flow during the Solar Cycle 23/24 minimum in 2008 is $\sim$ 20% faster than the meridional flow during the Solar Cycle 22/23 minimum in 1996. This result has been confirmed with helioseismology by Basu & Antia (2010) and González Hernández et al. (2010).

To investigate the variations in the structure of the axisymmetric flows, we used the flow profiles to create history plots. For each Carrington rotation, the measured flow profiles are smoothed with a tapered Gaussian with a FWHM of $\sim 1^\circ$. We then plot these smoothed profiles as a function of

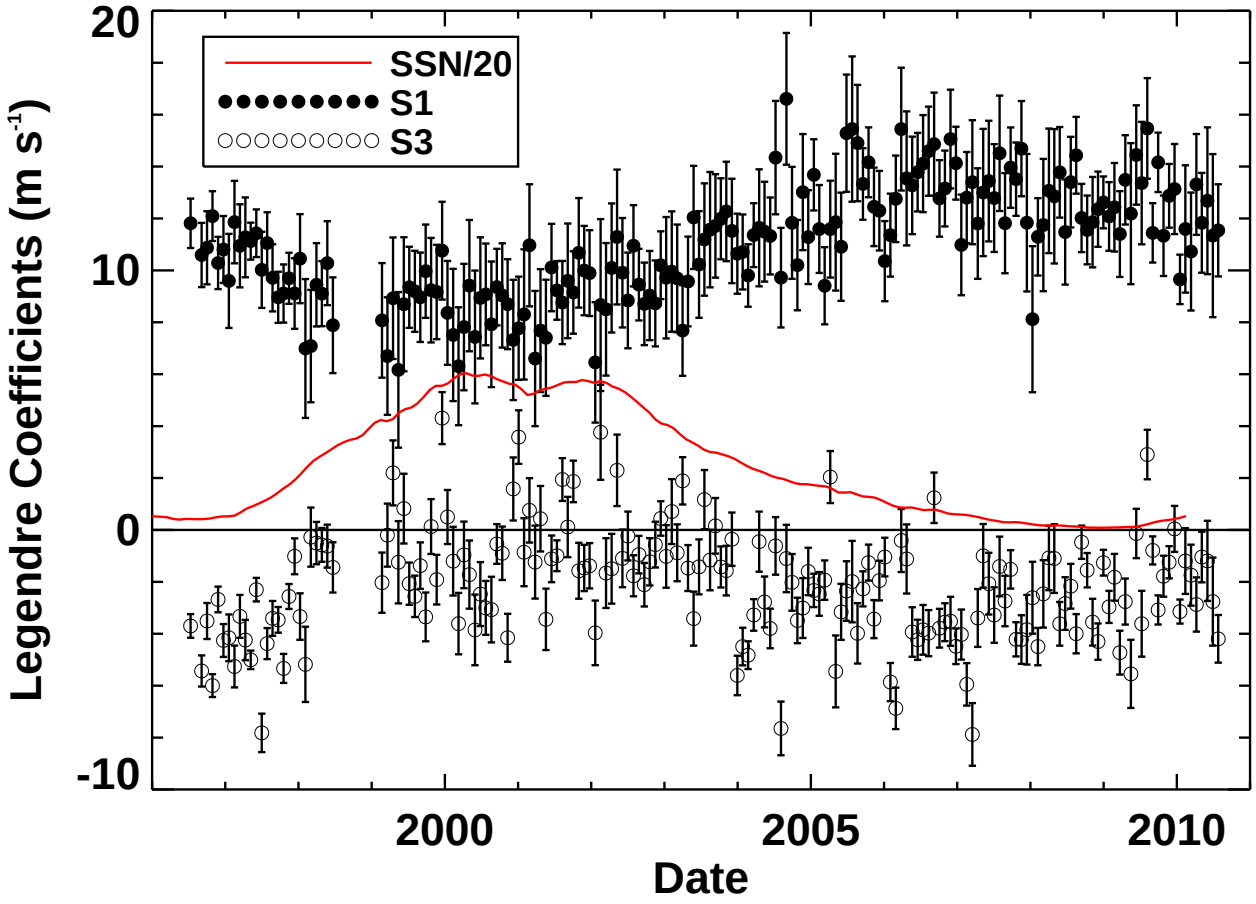

Figure 3.6: Legendre Coefficients used to represent the MDI Meridional Flow. These coefficients can be used with the polynomials given by (3.5) to represent the differential rotation. S1 multiplies P_2^1 and S3 multiplies P_4^1. For reference the smoothed sunspot number divided by 20 is shown in red.

both latitude and time.

We find that the differential rotation is relatively static, and so it's history plot was uninformative (and therefore not shown here). We then subtracted the average symmetrized profile from the smoothed profile for each rotation and plotted the residual to create a difference history for the differential rotation (shown in Figure 3.7). Blue represents retrograde (or slower than average) motion, while yellow represents prograde (or faster than average) motion. The centroid positions for the active regions are shown in red. Prograde flow is observed on the equatorward side of active regions while retrograde flow is observed on the poleward of side active regions. This is

the signature of the torsional oscillation first observed by Howard & Labonte (1980) and may be associated with cooling due to enhanced radiation in small scale magnetic features in the network surrounding active regions (Spruit, 2003). These results are consistent with the torsional oscillations observed with helioseismology (Howe et al., 2009). However, while those results required averaging the two hemispheres, our measurements are not subject to that restriction.

The meridional flow history (Figure 3.8) revealed polar counter-cells (regions of equatorward plasma flows). Blue represents equatorward flow and yellow represents poleward flow. Prior to 2001 a counter-cell (blue) is seen in the South. Around 2001, the southern counter-cell dwindles away while a new counter-cell appears to form in North. The longer duration of the counter-cell in the North (compared to the cell in the South) explains the asymmetry seen in the average meridional flow profile. The weakening of the meridional flow during solar maximum can be seen as dampened yellow tones near the active regions. The difference history for the meridional flow is shown in Figure 3.9. The counter-cells become more apparent in the difference history. In addition, the weakening of the meridional flow during solar maximum appears as an inflow toward the active latitudes, particularly on the poleward side of the active latitudes. These MDI results were published in Hathaway & Rightmire (2010, 2011).

3.1.3 HMI Analysis

SDO was launched in February, 2010 with HMI on board and began obtaining full-disk magnetograms in April 2010. HMI magnetograms, with a size of 4096^2, have four times the spatial resolution of MDI full-disk magnetograms (see Figure 1.4). HMI magnetograms are continuously available with a cadence of 45 seconds, rather than the 96 minutes of MDI. HMI magnetograms averaged over 720 seconds are virtually unaffected by the p-modes (Liu et al., 2012). These advances make HMI data ideal for the continuation of our correlation tracking analysis and ideal for extending the measurements to higher latitudes. From the HMI dataset, we chose the HMI 720 second full-disk line-of-sight magnetograms, obtained every hour on the hour, for analysis.

Again, we divided the line-of-sight signal by the cosine of the heliographic angle from disc

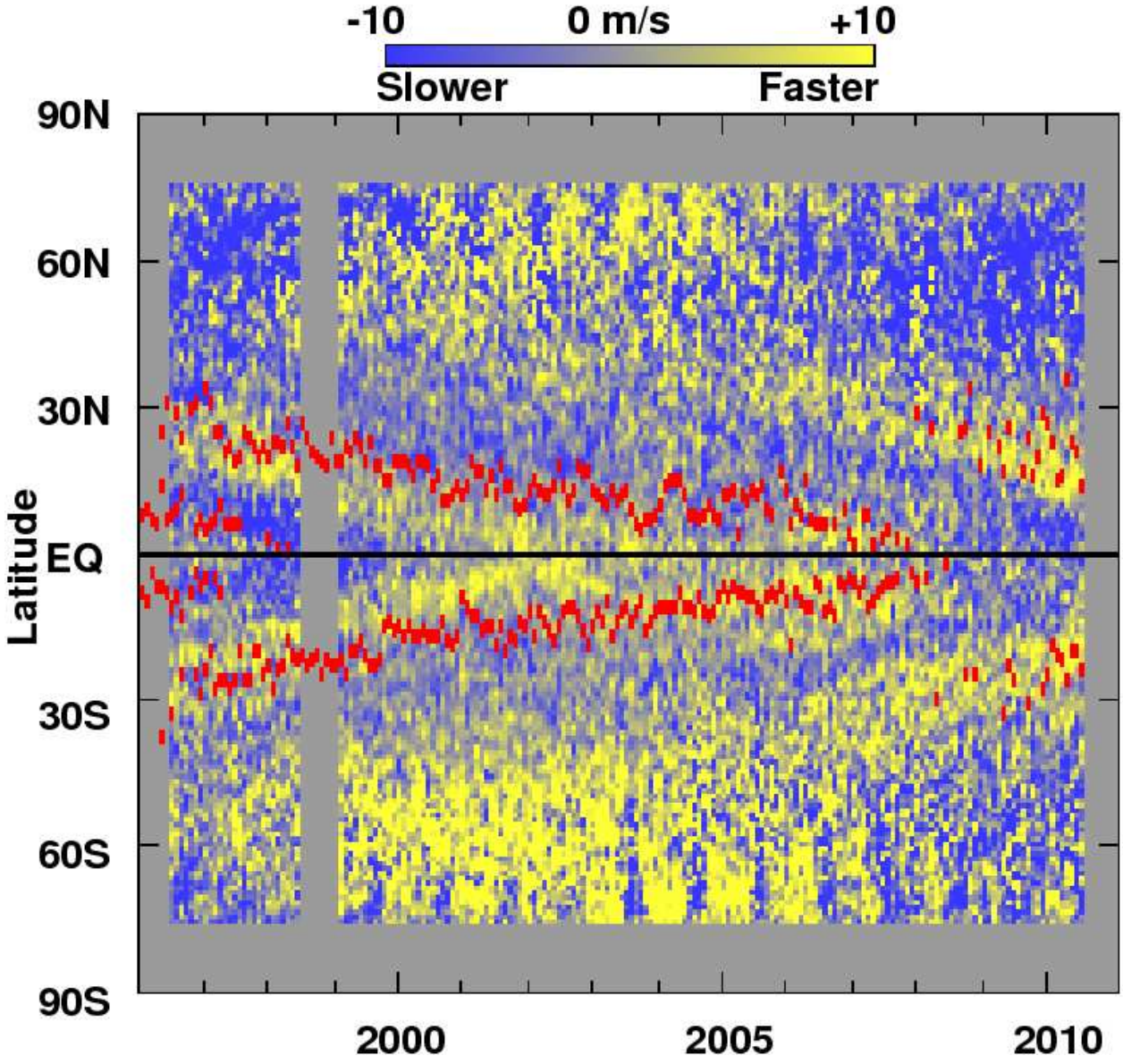

Figure 3.7: Difference History for the MDI Differential Rotation. The average symmetric profile has been subtracted from the individual differential rotation profiles and plotted as a function of time from 1996 to 2010. Retrograde flow (slower relative to the average) is indicated by blue and prograde flow (faster relative to the average) is indicated by yellow. The active region centroid position is shown in red for each hemisphere for reference.

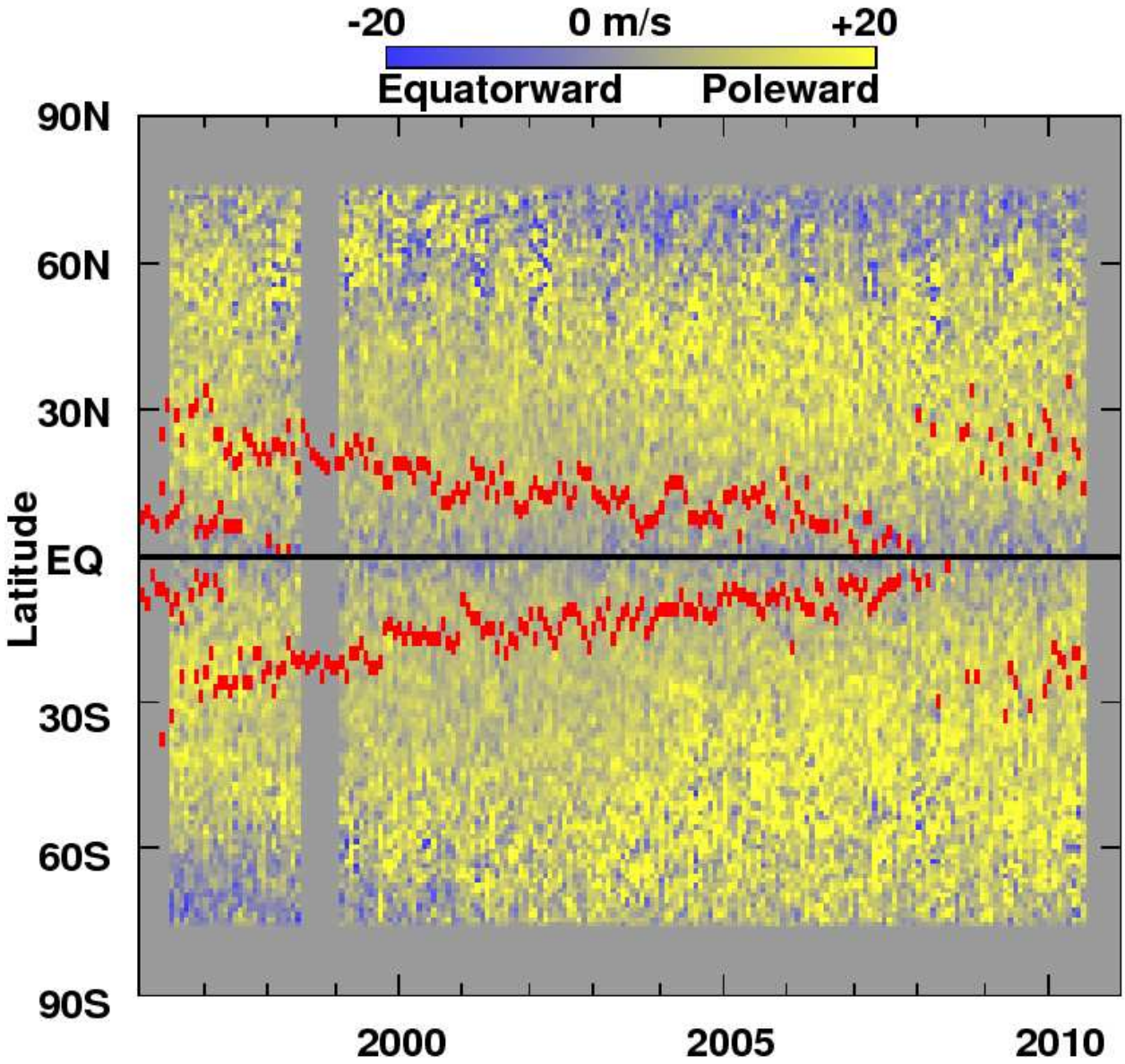

Figure 3.8: History for the MDI Meridional Flow. The smoothed meridional flow profiles plotted as a function of time from 1996 to 2010. Equatorward flow is indicated by blue and poleward flow is indicated by yellow. The active region centroid position is shown in red for each hemisphere for reference.

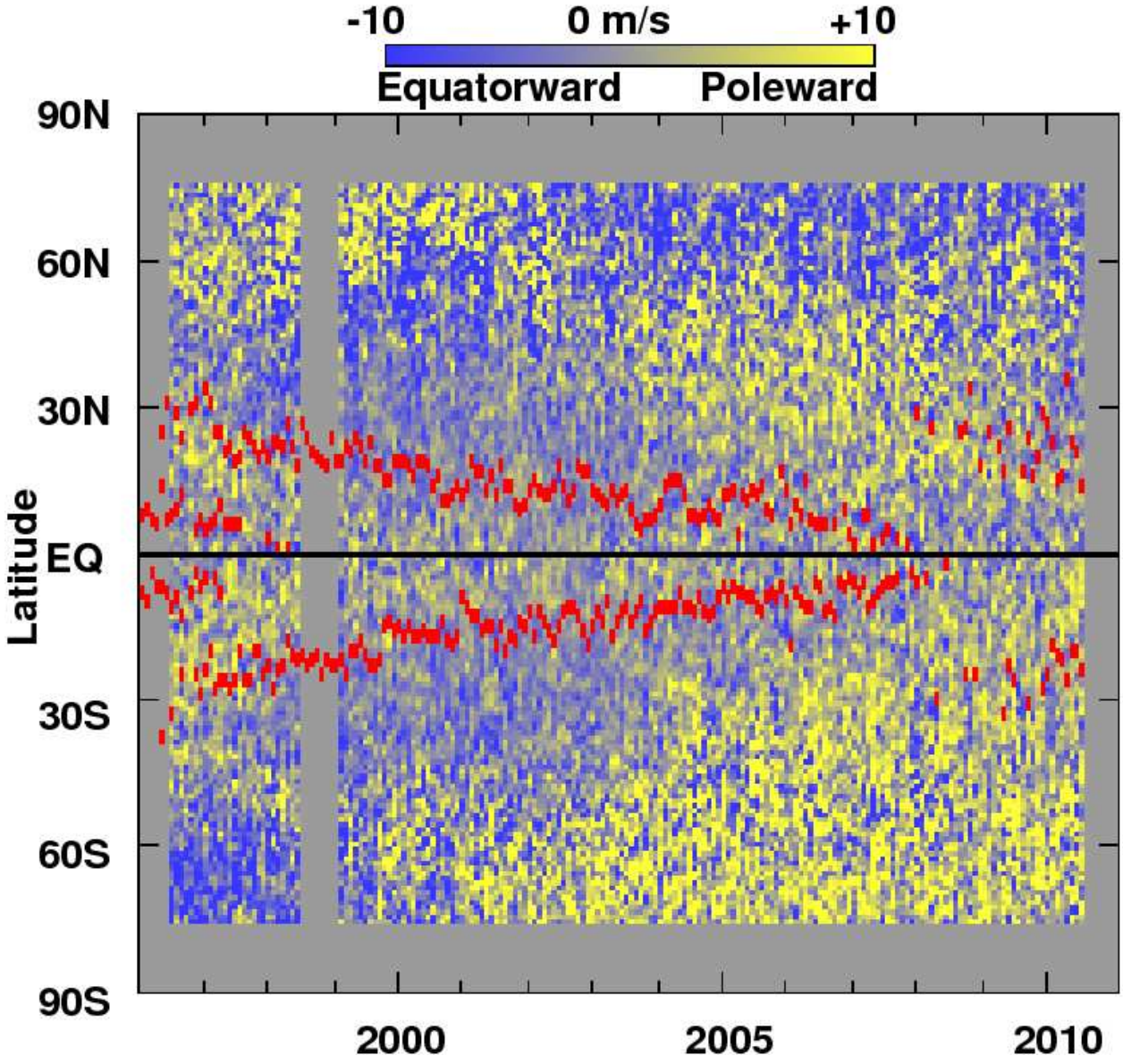

Figure 3.9: Difference History for the MDI Meridional Flow. The average symmetric profile has been subtracted from the individual meridional flow profiles and plotted as a function of time from 1996 to 2010. Equatorward flow (relative to the average) is indicated by blue and poleward flow (relative to the average) is indicated by yellow. The active region centroid position is shown in red for each hemisphere for reference.

center and mapped into heliographic coordinates while excluding data within three pixels from the limb. Corrections were made for the ephemeris error in the orientation of the Suns rotation axis (recall Figure 3.2). The analysis with masked regions is significantly more computationally intensive, therefore due to the large size of the HMI magnetograms, we only performed masking equatorward of 30° (where active regions occur). For HMI, pixels with |B|>1000 G and the adjacent pixels were masked out.

We divided the 4096x4096 HMI magnetic maps into 41x2401 pixel strips, one for every 10^{th} pixel latitude position. (One of these strips is shown in Figure 3.10) These HMI strips correspond to the same area as the 11x601 pixel MDI strips. Figure 3.10 shows an example of an HMI mapped image from a 720 second magnetogram with one of these strips marked for reference. We then cross-correlated each strip with corresponding strips from 8 hours later. Measurements were obtained with $\sim$ 600 image pairs for HMI during each 27-day rotation of the Sun. We then averaged these measurements over the entire rotation and calculated the RMS variations about those averages.

With HMI data, we further improved our cross-correlation analysis by incorporating a Forward-Backward technique. In the Forward step (previously used exclusively) a strip centered on the central meridian is taken from the initial map and cross-correlated with shifted strips from the later map. In this case, the displacement is typically prograde and poleward. In the Backward step, a strip centered on the central meridian is taken from the later map and cross-correlated with shifted strips from the initial map. In this case, the displacement is typically retrograde and equatorward. The correlations were then combined and the peaks in the subsequent cross-correlations were fit to parabolas with the position of that peak used to determine flow velocities in both latitude and longitude. By applying this Forward-Backward technique, our statistics are doubled, further reducing the noise. Moreover, any systematic effect that might mimic flow toward or away from disk center is then canceled in the meridional flow measurements by this Forward-Backward technique.

We find that while spatial resolution is impaired near the limb, this only results in noisier

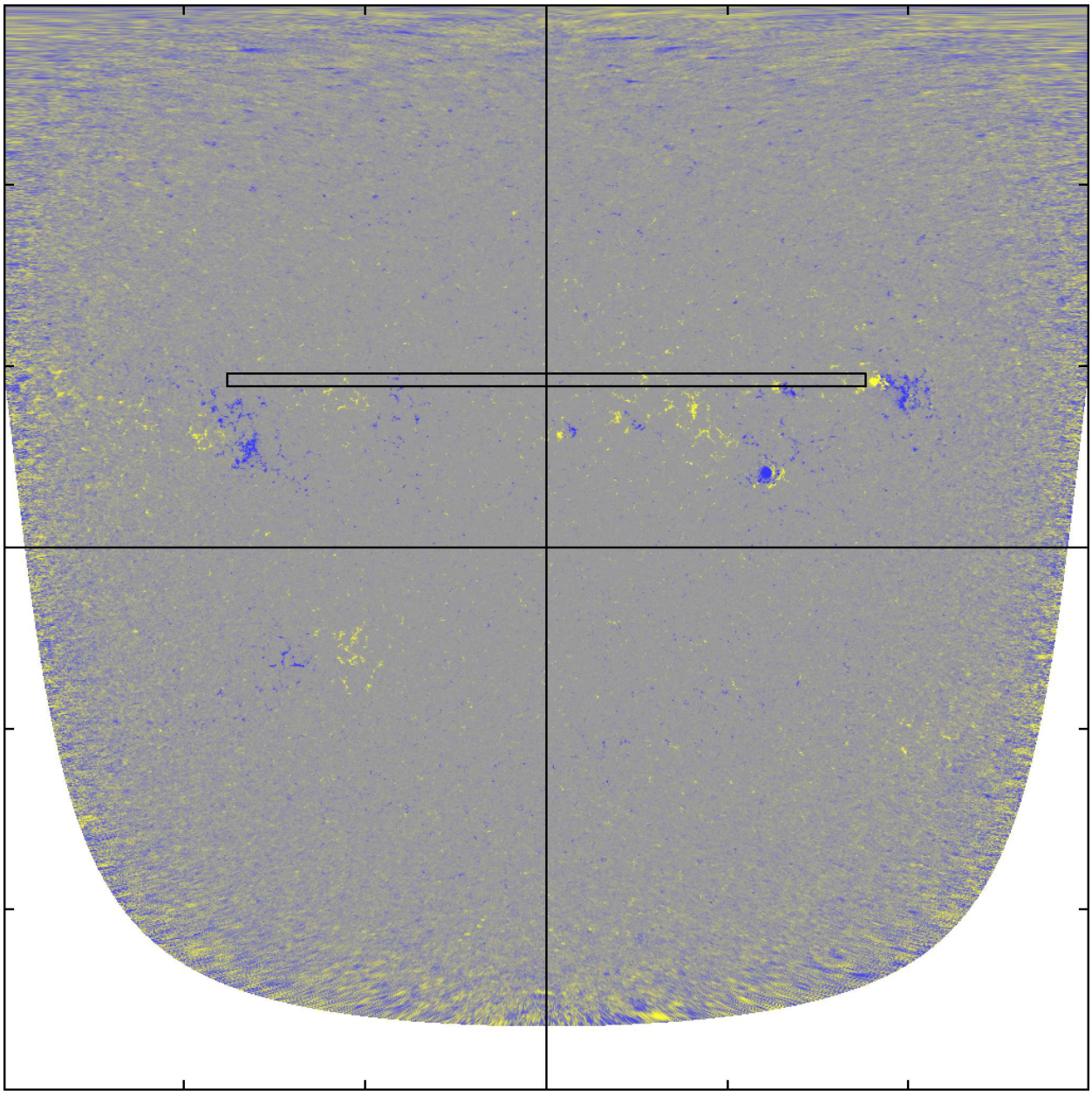

Figure 3.10: A 720 second averaged magnetogram from 9/2/2010 at 10:00:00 U.T. mapped into heliographic coordinates from pole to pole and $\pm 90^{\circ}$ from the central meridian and with a resolution of 4096^2. For this date and time the North polar region is well sampled while the South is not. An example of a 41x2401 pixel strip used in our cross-correlation analysis is marked for reference.

measurements at the higher latitudes without inducing a net flow signal. While MDI measurements were restricted to 75°, HMI measurements were attempted at latitudes up to 85° in both the North and South but were limited to latitudes where the strips did not extend beyond the mapped data ($\sim$75° when the Sun's rotation axis was tilted away from the instrument).

Geometrical errors in the size, shape, or orientation of the images can lead to systematic errors in the desired flows. Using simultaneous measurements from MDI and HMI allows us to identify these errors. Carrington Rotations 2096-2107 comprise the $\sim$ 1 year of overlap between observations made by these two instruments. Particular attention was paid to the systematic and statistical errors and the consequent latitudinal limits for the two data sources.

3.1.4 HMI Results

We averaged the axisymmetric flow velocities from each Carrington Rotation over Carrington Rotations 2096-2107 (April 2010 - March 2011) using the inverse of the standard errors squared as weights. The HMI average flow velocity profiles were then plotted on top of the average flow velocities obtained using MDI data from the same time periods. We find that results obtained with HMI data have significantly less noise than those from MDI, especially near the poles.

The HMI meridional flow results were found to be $\sim 2-3$ m s^{-1} more northward than the MDI results. This offset can be explained by a rotation of the HMI imaging system with respect to MDI, as suggested by Liu et al. (2012). Further analysis revealed that the MDI images needed to be corrected for a 0.19° rotation relative to the Sun's rotation axis (rather than the 0.21° used previously). Applying a least squares fit to the difference between the two profiles indicates a counter-clockwise rotation of HMI by 0.075° (or a meridional flow velocity correction of $\sim 2.5\cos(\lambda)$ m s^{-1}). Our corrected HMI average flow velocity profiles are plotted along with the MDI profiles in Figure 3.11 (differential rotation)and Figure 3.12 (meridional flow).

We find that our MDI and HMI differential rotations, equatorward of 55°, are in very good agreement. There are however small systematic differences ($\sim 1-2$ m s^{-1}), with larger velocities in HMI. Poleward of 55° HMI is $\sim 10-20$ m s^{-1} more retrograde relative to the rotating frame

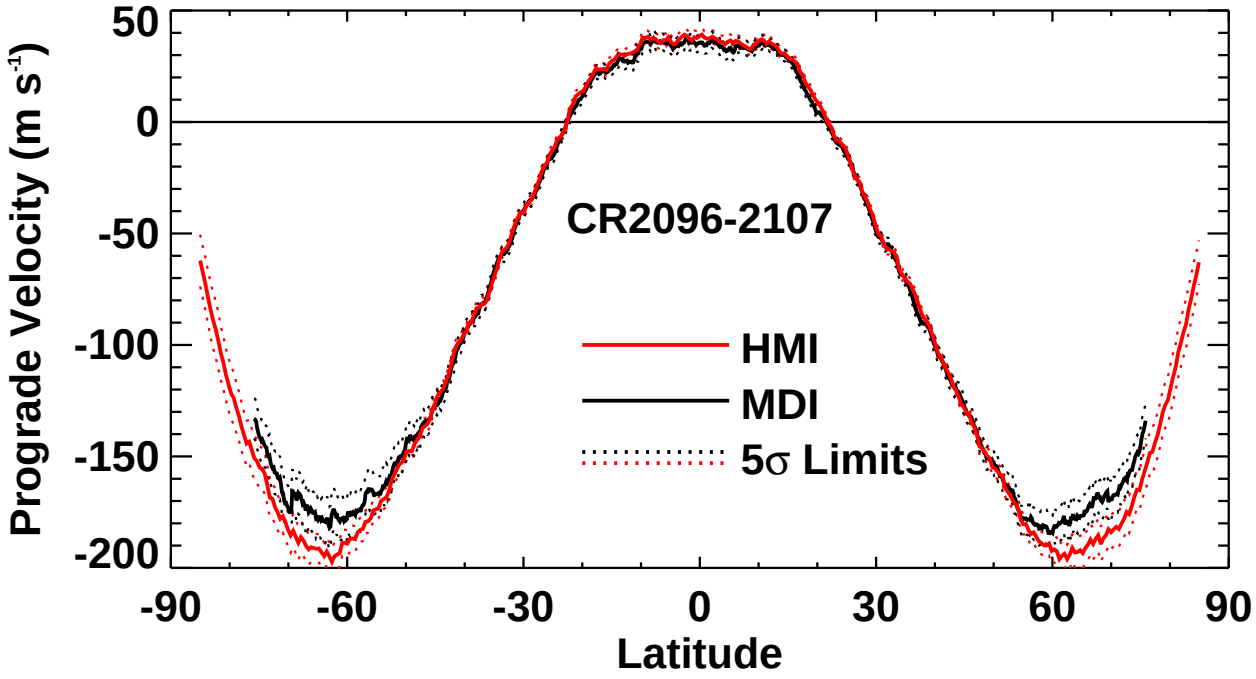

Figure 3.11: The Differential Rotation from Carrington Rotations 2096-2007. The MDI result is plotted in black and the HMI result is plotted in red. The five sigma error ranges are indicated by the dotted lines.

of reference than MDI. This may be attributed to a reported elliptical distortion of the MDI images (Korzennik et al., 2004) which was not completely accounted for in our mapping due to the fact that it is not well characterized. We find that the statistical errors in the HMI data (dotted red lines in Figure 3.11) indicate that precise measurements can be made to $\pm 85^\circ$ latitude.

Our HMI measurements of the meridional flow also agree well with our MDI measurements obtained at latitudes up to $\sim 55^\circ$ (Figure 3.12a), but are systematically slower by $\sim 1-2$ m s^{-1}. Again, this can be attributed to a possible elliptical distortion of MDI images. We find that at higher latitudes HMI tells a different story than MDI. Our MDI measurements suggested a counter-cell in the North (equatorward flow above $\sim 60^\circ$) but flow to the pole in the South. Our HMI measurements have no indication of counter-cells in either hemisphere for this time interval. The results do show a slight, but potentially important, North-South asymmetry. A faster poleward flow is seen in the South through the active latitudes (from the equator to $\sim 40^\circ$) and in the North

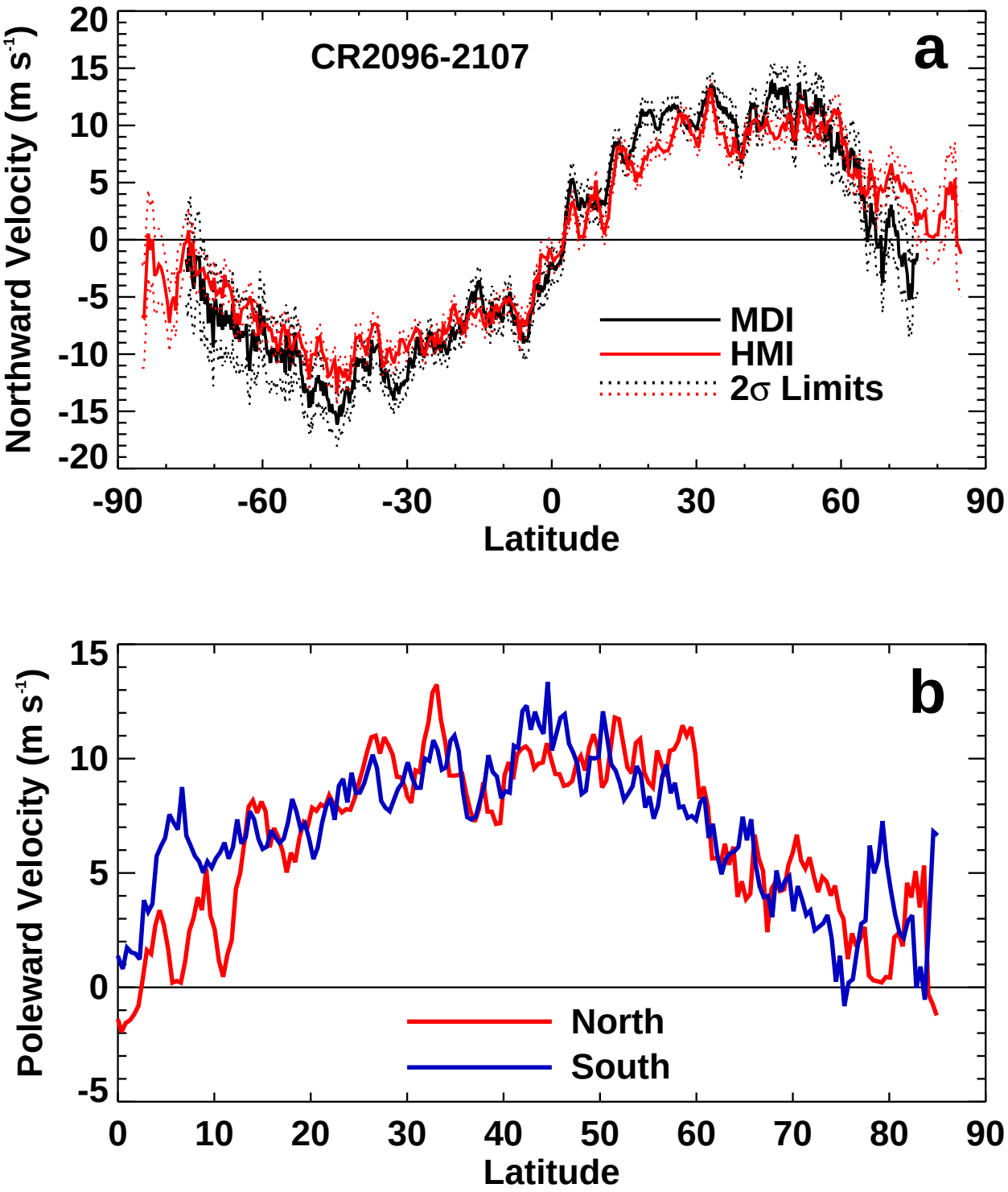

Figure 3.12: The Meridional Flow from Carrington Rotations 2096-2007. a) The corrected HMI results are shown in red. Results from MDI are shown in black. The two sigma error ranges are indicated by the dotted lines. b) The poleward velocities in the North (red) and South (blue) are plotted to highlight the North-South asymmetry.

at higher latitudes. The errors in our HMI meridional flow data (dotted red lines in Figure 3.12a) indicate that many of fluctuations in the meridional flow profile are actual features, rather than noise. We find that the noise level is low enough that the meridional flow is well determined at 85° using HMI data.

3.1.5 Discussion

We have characterized the axisymmetric flows using magnetic feature tracking for nearly the entire MDI era (Hathaway & Rightmire, 2010, 2011). We found that the meridional flow varied considerably during that time. Specifically, the meridional flow speed that led up to Solar Cycle 23/24 minimum in 2008 was much faster than the meridional flow speed during the prior minimum in 1996 (see Fig 3.13). Faster meridional flow in the active latitudes (equatorward of $\sim 40°$) inhibits the cancellation of opposite polarity magnetic elements across the equator (DeVore et al., 1984; Wang et al., 1989; van Ballegooijen et al., 1998; Schrijver & Title, 2001). This reduces the imbalance of magnetic polarities in the active latitudes which, when transported to the poles, leads to weaker polar fields, a weaker Solar Cycle 24, and an extended solar minimum between Solar Cycles 23 and 24. While this gives a credible physical explanation for the peculiarities of the Solar Cycle 23/24 minimum, it requires knowledge of the poleward transport all the way to the polar regions. For this reason, as well as others, it is important to measure the meridional flow to the highest latitudes possible.

Models of the magnetic flux transport at the Sun's surface have employed meridional flow profiles (shown in Figure 3.14) which either stop completely at 75° latitude or quickly fall to zero before entering the polar regions (van Ballegooijen et al., 1998; Schrijver & Title, 2001; Wang et al., 2009). These meridional flow profiles were chosen because they worked best with the model (i.e., enabled the model to produce results that best matched observations). However, our measurements of the axisymmetric flows show that these meridional profiles are not realistic. The meridional circulation varies considerably over the solar cycle and from one cycle to the next. Furthermore, the meridional flow typically extends all the way to the poles. These observations suggest that

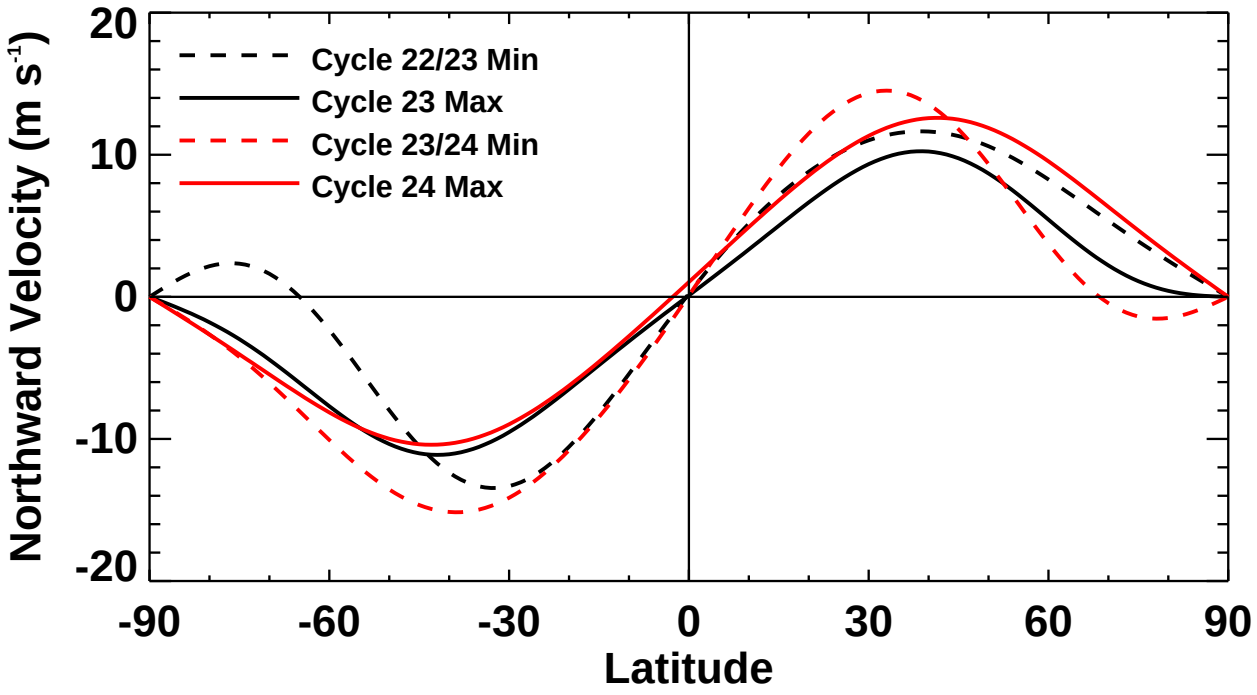

Figure 3.13: Meridional Flow Variations. The meridional flow is faster at solar minimum than at solar maximum. The meridional flow for Solar Cycle 24 was faster than the meridional flow for Solar Cycle 23.

revisions to flux transport models are needed.

We find that the improved data from HMI can extend the measurements of the axisymmetric flows, differential rotation and meridional flow, to much higher latitudes – 85° or more (during this analysis, measurements were restricted to 85°). While noise levels are higher at the poles, it is reasonable to expect that measurements could be obtained all the way to the pole, particularly for Carrington Rotations in which the Sun is tilted 7° toward or away from the Earth. Our measurements of these flows during the $\sim$ 1 year of overlap between the MDI and HMI instrument operations clearly show that the poleward meridional flow extends to the poles. Surprisingly, we find no evidence for any polar counter-cells as was indicated in the highest latitude measurements from MDI.

Recently Zhao et al. (2012) found and corrected a systematic error in the meridional flow measurements made with time-distance helioseismology. Their comparison of their corrected merid-

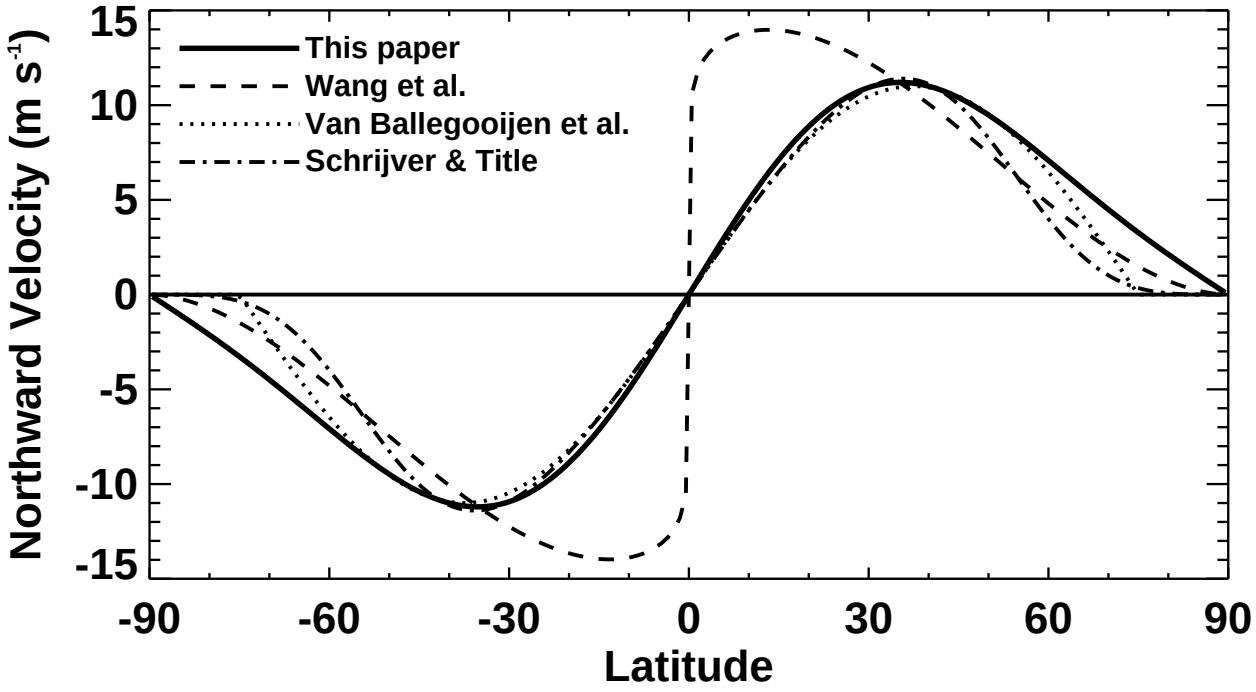

Figure 3.14: MDI Versus Surface Flux Transport Meridional Flow Profiles. The average meridional flow as measured by MDI (solid line) is compared with the meridional flow profiles that have been used in surface flux transport models. The flow profile used by van Ballegooijen et al. (1998) is indicated by the dotted line, Schrijver & Title (2001) is represented by the dot-dashed line, and (Wang et al., 2009) is shown with the dashed line.

ional flow profile with our contemporaneous meridional flow measurements from magnetic element motions seen with MDI (Hathaway & Rightmire, 2010) and from direct Doppler measurements (Ulrich, 2010) show good agreement to latitudes of $50-60^\circ$ but not much agreement at higher latitudes. Our high latitude measurements shown here are largely in agreement with the helioseismology results but further out of line with the direct Doppler measurements (which show counter-cells above 60° in each hemisphere).

We also find slight, but potentially important, North-South asymmetries in the meridional flow profile. The poleward flow is faster in the South in the active latitudes and faster in the North in the polar latitudes. Both of these asymmetries may help to explain the observed North-South asymmetry in the polar fields. Shiota et al. (2012) observed a faster decline in magnetic flux of the

North pole between 2008 and 2012 than was seen in the South. The trend in the North suggests an imminent polar field reversal. While some of this trend may be due to the fact the the northern hemisphere was more active during this period, the observed meridional flow asymmetry should also contribute.

The Sun's polar field reversals are produced by the poleward transport of opposite polarity magnetic flux from the active latitudes (opposite to that of the pole at the start of the sunspot cycle). While active regions (sunspot groups) have a balance of both magnetic polarities, in each hemisphere the opposite polarity is systematically found at higher latitudes (Joy's Law). Some of the lower latitude, like polarity, magnetic elements can cross the equator to cancel with similar (but reverse) polarity elements from the other hemisphere and leave behind an excess of the higher latitude, opposite polarity, magnetic elements. A fast meridional flow through the active latitudes inhibits this cross-equator cancellation and leaves a smaller excess of the opposite polarity for subsequent transport to the poles. Thus, the faster meridional flow in the southern active latitudes should result in a slower erosion of the South polar field. In addition, the fast poleward flow at high latitudes in the North should accelerate the erosion of the North polar field.

This poleward flow above 75° latitude is, nonetheless, problematic for most models of the magnetic flux transport in the near surface layers (van Ballegooijen et al., 1998; Schrijver & Title, 2001; Wang et al., 2009). In these models this high latitude poleward flow tends to produce polar magnetic fields that are too strong and too highly concentrated at the poles themselves. Our high latitude meridional flow observations may require further adjustments be made to those models.

3.2 Non-Axisymmetric Flows

In this work, I introduce a purely advective surface flux transport model that strives to reproduce the surface flows as they are observed on the Sun. In addition to the axisymmetric flows (meridional flow and differential rotation), magnetic features on the Sun are transported by turbulent motions caused by convection, primarily in the form of supergranules. Previous surface flux transport models have employed a diffusive term to simulate the effects of these convective motions

with a parameterized diffusion coefficient. In the surface flux transport model presented here, the convective flows are created explicitly by using vector spherical harmonics, as described by Hathaway et al. (2010) and Hathaway (2012a). While the convective flow model was developed by Dr. David Hathaway and was not created as part of this dissertation, it constitutes a major component of the surface flux transport model, and thus warrants an in-depth discussion.

Hathaway et al. (2010) measured the supergranule spectrum using full-disk Doppler images obtained with the MDI instrument on SOHO during the 1996 MDI Dynamics Run (a period of 60 days where MDI made full disk dopplergrams at a cadence of 1 minute). They began by filtering out the $p-$mode signal (a.k.a 5-minute oscillations) caused by acoustic waves at the surface. This was done by using a tapered Gaussian to average Doppler images over 31 minutes. These filtered images were obtained with a cadence of 15 minutes for the full 60 day period. An example is shown on the left of Figure 3.15. These images include additional Doppler signal due to observer motion,the convective blue shift (an excess blue shift due to the fact that updrafts are brighter than downdrafts), and the axisymmetric flows. These flows (shown in Figure 3.16 were measured and removed to produce images of the supergranular motions (shown on the right of Figure 3.15). The images of the supergranular motions were then mapped into heliographic coordinates

The heliographic images of the supergranular motions were projected onto spherical harmonics. The power at a given wavenumber(l) is given by

$$P(l) = \sum_{m=-l}^{l} |A_l^m|^2 \tag{3.6}$$

with

$$A_l^m = \frac{1}{N_l^m} \int_{-l}^{1} \int_{\phi_1}^{\phi_2} V_{los}(\theta,\phi) W(\theta,\phi) Y_l^m(\theta,\phi) d\phi d(\cos\theta) \tag{3.7}$$

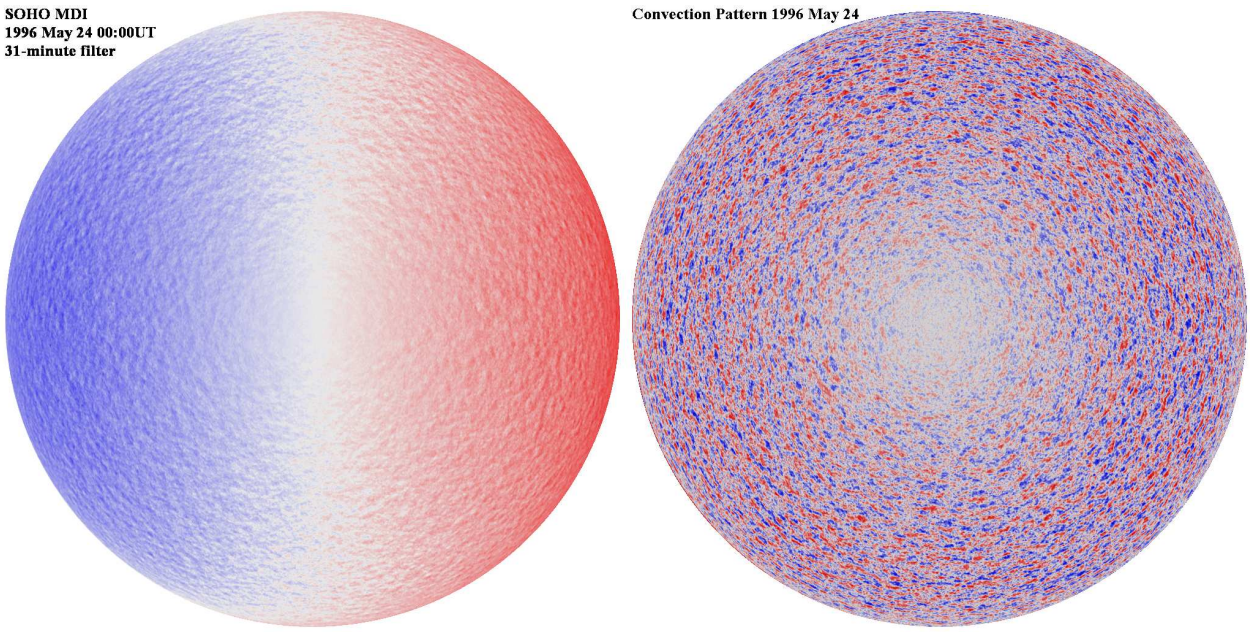

Figure 3.15: MDI Doppler Images. The image on the left shows the original MDI Doppler signal. This signal includes additional signals (see Figure 3.16 that once removed produce the supergranule pattern created by convective motions (shown on right). Credit: David Hathaway, NASA/MSFC.

where N_l^m is the normalization function given by

$$N_l^m = \int_{-l}^{1} \int_{\phi_1}^{\phi_2} W(\theta,\phi)[Y_l^m(\theta,\phi)]^2 d\phi d(\cos\theta) \tag{3.8}$$

and $Y_l^m(\theta,\phi)$ is the spherical harmonic function, $V_{los}(\theta,\phi)$ is the line of sight velocity, and $W(\theta,\phi)$ is a weighting function (used to smooth discontinuities). Here, θ is the colatitude measured southward from the north pole, and ϕ is the longitude measured prograde from the central meridian.

These observations are simulated by creating synthetic data from vector velocities created with a set of complex spectral coefficients R_l^m (radial), S_l^m (solenoidal/poloidal), and T_l^m (toroidal) with $l = 0$ to $l = 1500$. These coefficients were used to create vector velocities to simulate convection

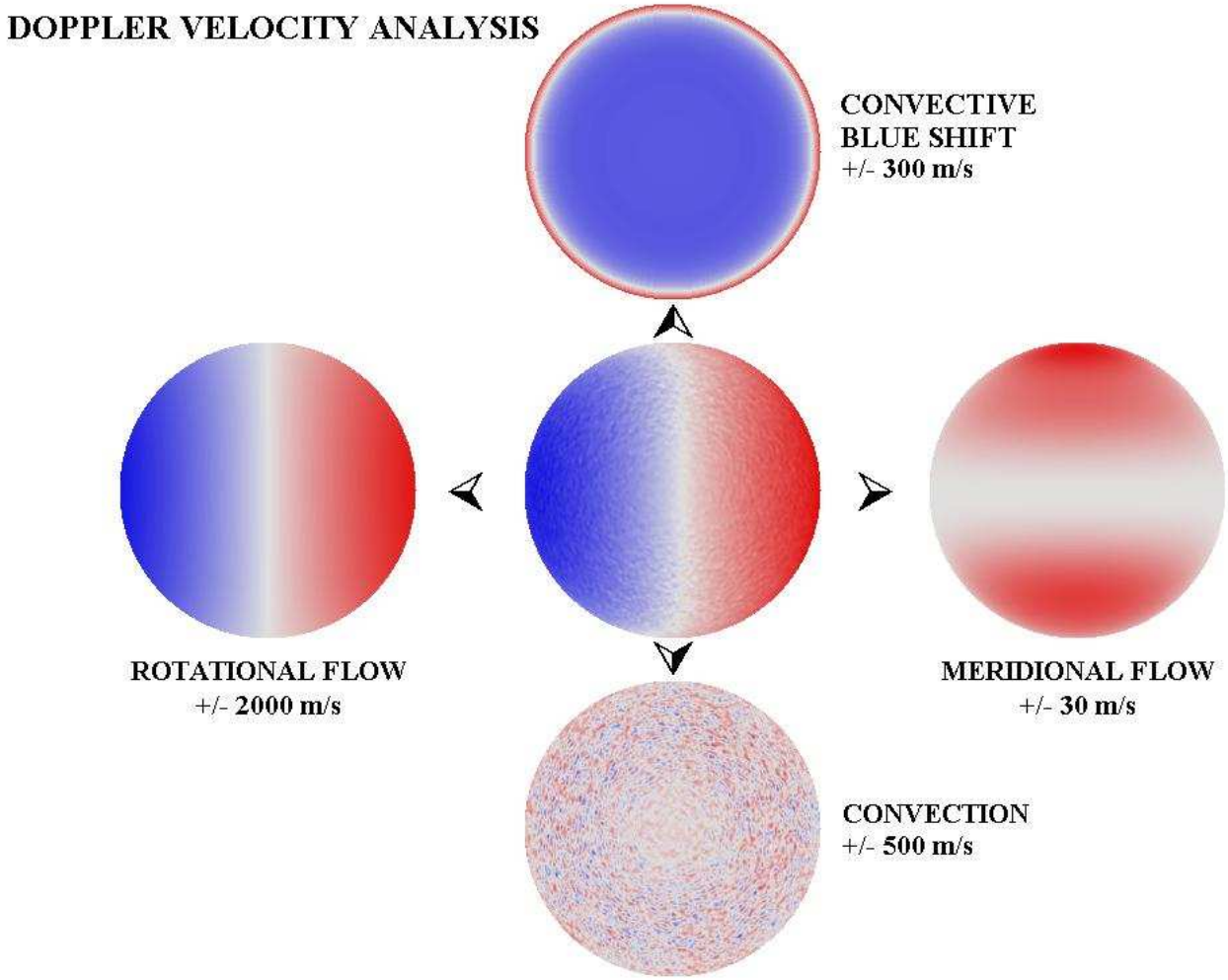

Figure 3.16: Doppler Signals. This image illustrates the four component signals in a Doppler Image of the Sun. These signals include the convective blue shift, the rotational flow, and the meridional flow. These three signals must be carefully removed in order to obtain the signal for the convective motions. The relative velocities are notated for reference.Credit: David Hathaway, NASA/MSFC.

cells. These vector velocities are given by Chandrasekhar (1961):

$$
\begin{aligned}
V_r(\theta,\phi) &= \sum_{l=0}^{l_{max}} \sum_{m=-l}^{l} R_l^m Y_l^m(\theta,\phi) \\
V_\theta(\theta,\phi) &= \sum_{l=0}^{l_{max}} \sum_{m=-l}^{l} S_l^m \frac{\partial Y_l^m(\theta,\phi)}{\partial \theta} + \sum_{l=0}^{l_{max}} \sum_{m=-l}^{l} \frac{1}{\sin\theta} T_l^m \frac{\partial Y_l^m(\theta,\phi)}{\partial \phi} \\
V_\phi(\theta,\phi) &= \sum_{l=0}^{l_{max}} \sum_{m=-l}^{l} \frac{1}{\sin\theta} S_l^m \frac{\partial Y_l^m(\theta,\phi)}{\partial \phi} - \sum_{l=0}^{l_{max}} \sum_{m=-l}^{l} T_l^m \frac{\partial Y_l^m(\theta,\phi)}{\partial \theta}
\end{aligned}
\tag{3.9}
$$

The three components of the vector velocity are combined to produce a line-of-sight velocity (V_{los})

$$\begin{aligned} V_{los} = {} & V_r(\theta,\phi)\sin B_0\cos\theta + V_r(\theta,\phi)\cos B_0\sin\theta\cos\phi + \\ & V_\theta(\theta,\phi)\sin B_0\sin\theta - V_\theta(\theta,\phi)\cos B_0\cos\theta\cos\phi + \\ & V_\phi(\theta,\phi)\cos B_0\sin\phi \end{aligned} \tag{3.10}$$

The line-of-sight velocities were mapped into a simulated Doppler velocity image and the simulated power spectra was measured as with the MDI data. The spectral coefficients (R_l^m, S_l^m, and T_l^m) were adjusted iteratively until the simulated power spectra matched the spectra observed from the MDI data. These spectra are shown in Figure 3.17. Figure 3.18 shows that the observed data and simulated data are visually indistinguishable. The closest match was obtained with input spectra constructed from two Lorentzian functions. The first Lorentzian corresponds to the supergranules with a peak at $l \sim 100$ and a width of 100. The second Lorentzian corresponds to the granules with peak at $l \sim 4000$ and a width of 3000. (The diameters of convective cells are inversely proportional to wavenumber l.) These results suggest that Sun preferentially makes convective cells corresponding to these two sizes, thought the mechanism behind this is not currently understood.

While the direct contribution of the axisymmetric flows was removed from the Doppler signal, the supergranules themselves are nonetheless advected by axisymmetric flows (Hathaway, 2012a,b). These axisymmetric flows were measured by applying the cross correlation technique on the supergranules. Observationally, the lifetimes of convective cells are related to their sizes (granules live for minutes, while supergranules live for many hours). This relationship can be characterized with

$$\tau(l) = 6.5\frac{100^2}{l^2} \qquad \text{hours} \tag{3.11}$$

where $\tau(l)$ is the lifetime and l is the wavenumber. Small cells (with larger l) have shorter lifetimes, whereas large cells (small l) have longer lifetimes.

The finite lifetimes of the convective cells has a direct and important impact on the cross cor-

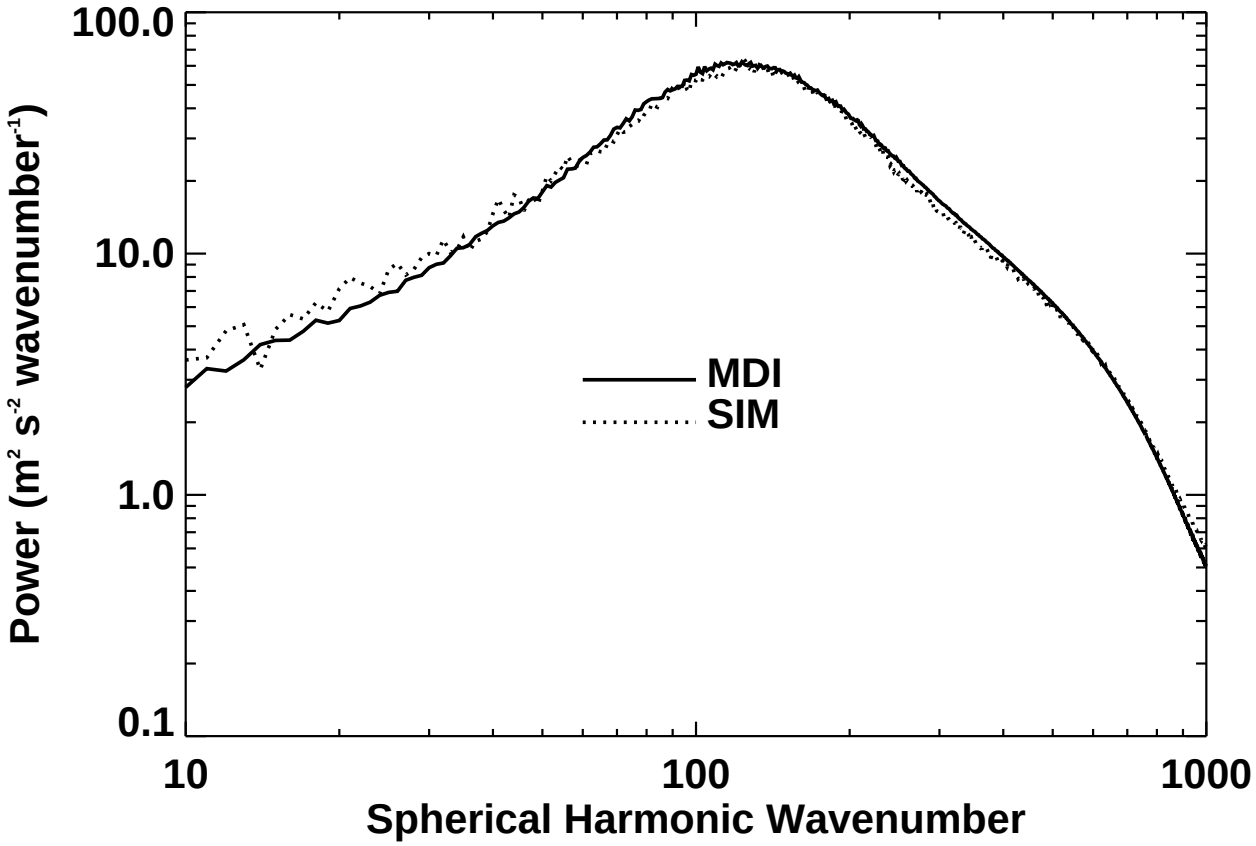

Figure 3.17: MDI Doppler Spectrum. Spectral coefficients R_l^m, S_l^m, and T_l^m were adjusted until the simulated Doppler image produced a power spectra that matched the spectra observed from the MDI data. Supergranules peak at wavenumber 110. Credit: David Hathaway, NASA/MSFC.

relation technique (Hathaway et al., 2010; Hathaway, 2012a,b). During a short time lag between images (e.g. 2 hours), the majority of convective cells are still "alive" producing strong cross correlation coefficients. As the duration of the time lag between images increases (e.g. 16 hours) many of the smallest convection cells have "died off" producing weaker cross correlation coefficients. Furthermore, the velocity of the convection cells changes with size. Larger long lived cells extend deeper and have velocities of the flows at those depths. This means that as the time lag increases, the velocities measured will be more representative of convection cells that extend deeper into the convection zone.

The simulated convective cells were moved by the axisymmetric flows through an advection

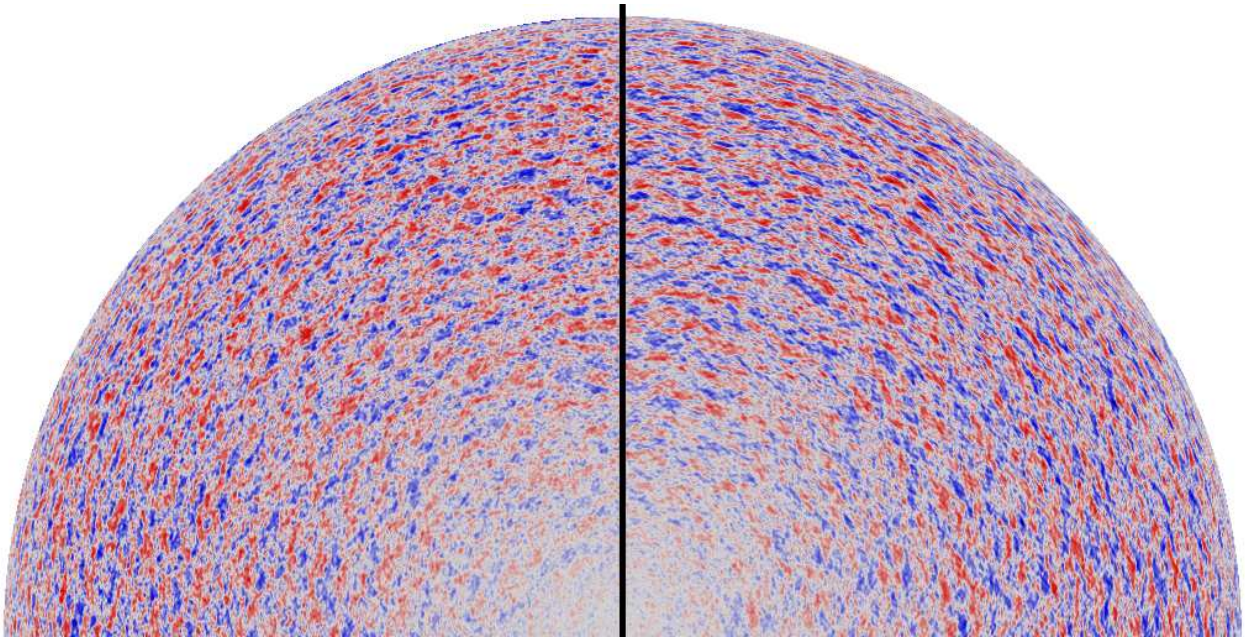

Figure 3.18: Doppler Simulation. A Doppler image (left) of the observed convective motions is shown alongside of the simulated convective motions (right). The two are visually identical. Credit: David Hathaway, NASA/MSFC.

equation given by

$$\frac{\partial w}{\partial t} = -\frac{MF(\theta)}{r}\frac{\partial w}{\partial \theta} - \frac{DR(\theta)}{r\sin\theta}\frac{\partial w}{\partial \phi} \tag{3.12}$$

where w is a velocity component, $MF(\theta)$ is the meridional flow as a function of latitude in m s^{-1}, and $DR(\theta)$ is the differential rotation as a function of latitude in m s^{-1}. These axisymmetric velocities were projected into spherical harmonics to create a set of coupled equations with which to evolve the spectral coefficients for the convection. The finite lifetimes of the convective cells were reproduced in the simulation by perturbing the phases of the complex spectral coefficients. The size of these perturbations changed with wavelength so that the lifetimes increased with the size of the convective cells as in Equation (3.11).

The strength of the correlations as a function of time lag was measured with the simulated data and compared to the observed data (shown in Figure 3.19). The correlations of the simulated

data match the observed correlations fairly well for the 4, 8, and 18 hour time lags. However, with a 2 hour time lag, the observations show a weaker correlation than the simulation at 2 hours. (This suggests that the lifetimes of the smallest convection cells may need to be shorter in the simulation.)

The meridional flow was measured using cross-correlation on the simulated data and compared to the observed data (shown in Figure 3.20). Cross-correlation was performed with 2, 4, 8, 16, 24, and 32 hour time lags between images. The meridional flow is observed to become weaker with increasing depth. The meridional flow then reverses direction and becomes equatorward by a depth of 60Mm. Comparison of the simulation with the observations show that this weakening of the meridional flow as a function of depth is captured by the evolving supergranule simulation.

This evolving supergranule simulation was designed to emulate the details of convective motions on the Sun. It is visually indistinguishable from Doppler observations of the Sun. Furthermore, it is able to capture details of the turbulent motion including the power spectra, the finite lifetimes, and the change in the axisymmetric flows with depths. This simulation far surpasses the detail that can be provided by a diffusion coefficient alone, making it very effective for use in our surface flux transport model.

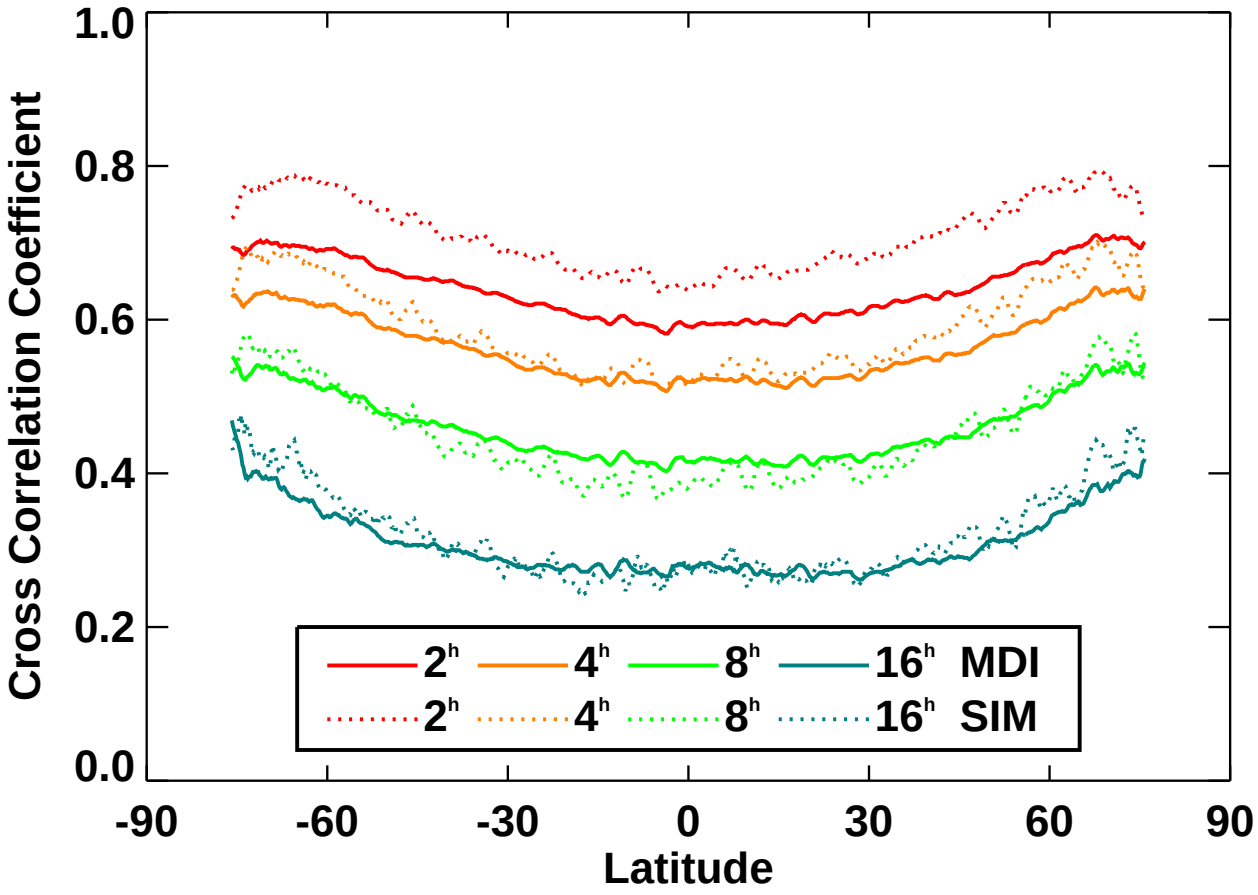

Figure 3.19: Doppler Pattern Cross-Correlation Coefficients. The strength of the cross-correlations are shown for 2, 4, 8, and 16 hour time lags. Coefficients for the observed data are indicated with solid lines while the coefficients for the simulated data are indicated with the dotted lines. The simulation matches the observed coefficients fairly well for 4, 8, and 16 hour time lags but the coefficients are weaker for the observations with a 2 hour time lag. Credit: David Hathaway, NASA/MSFC.

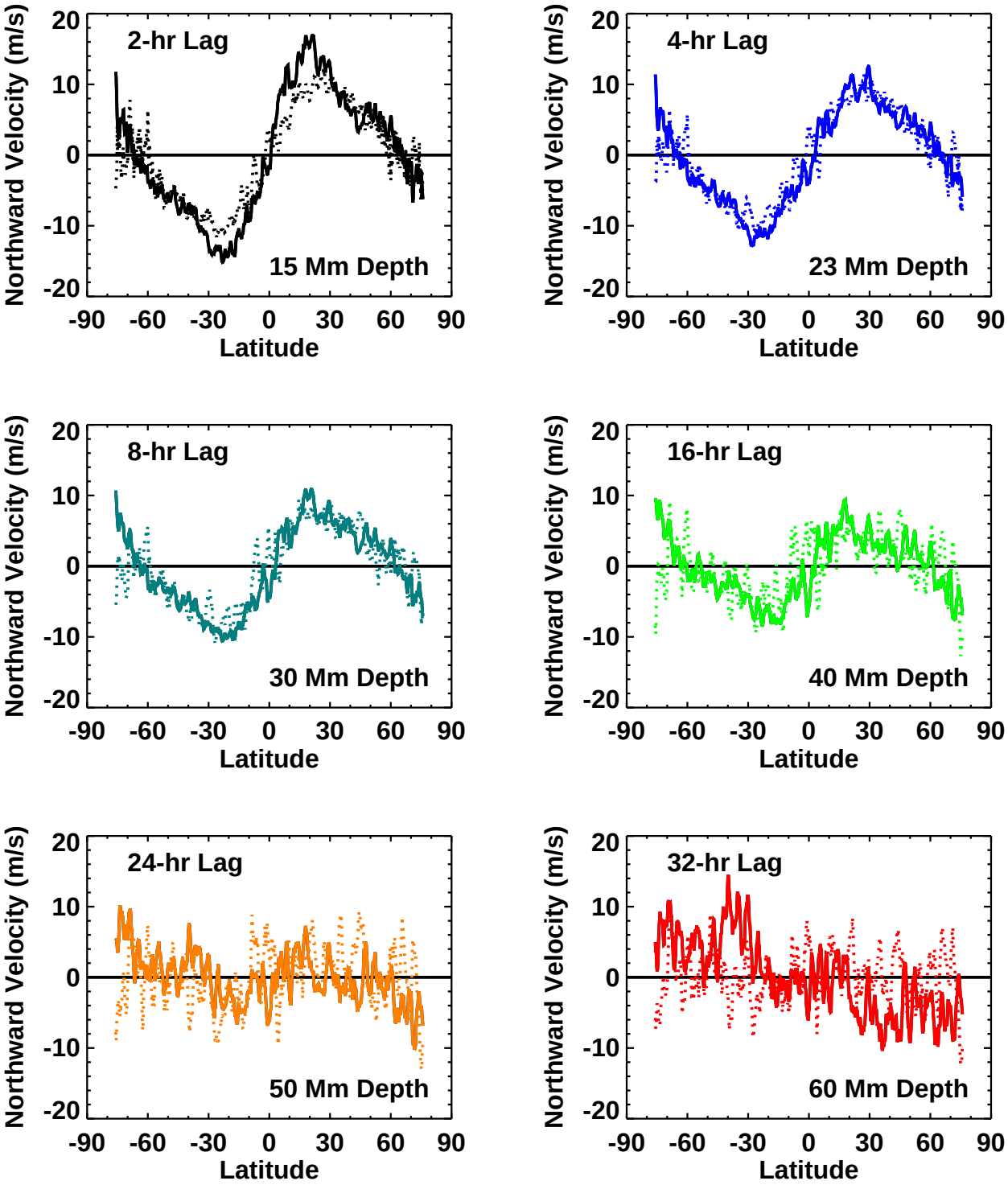

Figure 3.20: Doppler Pattern Meridional Flow. The meridional flow measured by cross-correlating the observed (solid lines) and simulated (dotted lines) Doppler images. Results are shown 2, 4, 8, 16, 24, and 32 hour time lags between images. Estimates of the corresponding depth are shown for reference. The meridional flow becomes weaker with depth and reverses all together by 60 Mm. The simulation matches the observations Credit: David Hathaway, NASA/MSFC.

CHAPTER 4

FLUX TRANSPORT MODEL

Previous surface flux transport models (see Section 2.2.2) have used meridional flow profiles that worked best with the model. These flow profiles were constant in time and typically stopped completely before reaching 75° in latitude. However, observations presented in Chapter 3 have shown that these meridional profiles are not realistic. The meridional circulation has been found to vary considerably over the solar cycle and from one cycle to the next (Hathaway & Rightmire, 2010; Basu & Antia, 2010; González Hernández et al., 2010). Unlike the flow profiles used in prior models, the meridional flow was also found to extend all the way to the poles (Hathaway & Rightmire, 2011; Rightmire-Upton et al., 2012). Additionally, surface flux transport models have typically employed a diffusive term to simulate effects of convective motions (i.e., advective-diffusive models). While this is easier to do computationally, the magnitude of this term is not well constrained and it does not fully capture the convective motions.

An ideal flux transport model should be able to reproduce the magnetic field evolution at the surface by incorporating the observed flows. In this chapter, I will introduce a surface flux transport model that advects the magnetic elements with the flows as they are observed on the Sun. The flux transport model will use the observed axisymmetric flows. Rather than a parameterized diffusive coefficient, the convective flows (i.e., supergranular flows) were modeled explicitly by using vector spherical harmonics, as described in Section 3.2 and by Hathaway et al. (2010), to create a purely advective surface flux transport model. This model, first introduced in (Upton & Hathaway, 2014), was developed as a collaborative effort between myself and Dr. David H. Hathaway.

4.1 Advective Surface Flux Transport Model

We have created a surface flux transport model to simulate the dynamics of magnetic fields over the entire surface of the Sun. The basis of this flux transport model is the advection equation:

$$\frac{\partial B_r}{\partial t} + \nabla \cdot (uB_r) = S(\theta, \phi, t) \tag{4.1}$$

where B_r is the radial magnetic flux, u is the horizontal velocity vector (which includes the observed axisymmetric flows and the nonaxisymmetric convective flows), and S is a (magnetic) source term as a function of latitude (θ), longitude (ϕ), and time (t).

This purely advective model is supported by both theory and observation. The Sun's magnetic field elements are carried to the boundaries of the convective structures (granules and supergranules) by flows within those convective structures. The motions of those magnetic elements are faithful representations of the plasma flow itself. These weak magnetic elements are transported like passive scalars (corks). This treatment has been found in numerous numerical simulations of magneto-convection (c.f. Vögler et al., 2005) and is borne out in high time- and space-resolution observations of the Sun (Simon et al., 1988; Roudier et al., 2009).

We modeled the convective flows, i.e., supergranular flows, explicitly by using vector spherical harmonics (described in Section 3.2 and by Hathaway et al. (2010)). We used a spectrum of spherical harmonics to create convection cells that reproduce the observed spectral characteristics. The spectral coefficients were evolved at each time step to give the cells finite lifetimes and the observed differential rotation and meridional flow. These convection cells have lifetimes that are proportional to their size, e.g. granules with velocities of 3000 m s^{-1}, diameters of 1 Mm, and lifetimes of $\sim$10 minutes and supergranules with velocities of 500 m s^{-1}, diameters of 30 Mm, and lifetimes of $\sim$1 day. These convective cells are advected by the axisymmetric flows given by our smoothed polynomial coefficients. The vector velocities were created for the full Sun with 1024 pixels in longitude and 512 pixels in latitude at 15 minute time steps.

Outside of active regions, the magnetic fields are weak and the plasma beta is high (see Equa-

tion (2.20)). For high beta, the magnetic pressure of these weak fields is dominated by the kinematic pressure, and these weak fields are carried by the plasma flows. Inside active regions, the plasma beta is low and the magnetic pressure dominates, so the flows are modified by the magnetic field. To account for this, we have reduced the supergranule flow velocities where the magnetic field was strong.

We have measured the axisymmetric flows (meridional flow and differential rotation) for each Carrington rotation by using feature tracking on MDI and HMI magnetograms as described in Section 3.1 (Hathaway & Rightmire, 2010, 2011; Rightmire-Upton et al., 2012). These axisymmetric flow profiles were fit with polynomials and the polynomial coefficients were smoothed using a tapered Gaussian with a full width at half maximum of 13 rotations. These smoothed coefficients were used to update the axisymmetric flow component of the vector velocities for each rotation, thereby including the solar cycle variations inherent in these flows.

The advection equation (4.1) was solved with explicit finite differencing (first order in time and second order in space) to produce magnetic flux maps of the entire Sun with a cadence of 15 minutes. (These maps are referred to as *synchronic maps* since they represent the Sun's magnetic field at a moment in time.) The high velocities and high resolution in the model can produce Gibbs phenomenon, i.e., ringing artifacts at sharp edges that can cause flux to overshoot/undershoot into surrounding pixels. To stabilize the numerical integrations and mitigate this effect, a diffusion term is added so that:

$$\frac{\partial B_r}{\partial t} + \nabla \cdot (uB_r) = S(\theta, \phi, t) + \eta \nabla^2 B_r \tag{4.2}$$

where η is the diffusivity. We note that this diffusivity term was strictly for numerical stability. Unlike previous Surface Flux Transport models, the addition of this term had little effect on the flux transport. The convective motions of the supergranular cells gave detailed random walks for the magnetic elements in this model.

Finite differencing requires that the Courant-Friedrichs-Lewy condition

$$\Delta x \geq v\Delta t \tag{4.3}$$

(where Δx is the grid spacing, v is the velocity, and Δt is the time step) be satisfied in order to maintain numerical stability. We have velocities of hundreds of m s^{-1} and a time step of 15 minutes, therefore Δx needs to be larger than 500 km at all latitudes. To ensure that this condition is met, we created a modified grid for performing the finite differencing. The modified grid features 1024 points at the equator. This is transitioned by repeatedly halving that number, leading to 8 points at the poles. These transitions occurred at latitudes where

$$1024\cos\lambda = \{512, 256, 128, 64, 32, 16, \text{and } 8\}\,. \tag{4.4}$$

To accommodate the modified grid, we applied three different finite differencing schemes: normal, transitioning, and polar (illustrated by Figure 4.1). Under the normal scheme, flux is advected in from two sides (e.g., positions B and D) and out the other sides (e.g., C and E). In the transitioning scheme, flux was advected normally in the horizontal direction (e.g., A_{new} = A_{old} + B - C), but an extra term was needed in the vertical direction (e.g., A_{new} = A_{old} + D - E_1 - E_2). For the polar scheme, again flux was advected normally in the horizontal direction. In the vertical direction, an extra term was added on one side but no term was present on the opposite side (where the polar boundary becomes a point). In all three schemes, the diffusion was accomplished by taking second derivatives in each direction and by using the average where two horizontal cells contribute.

4.2 The Baseline: Data Assimilation

Data assimilation is a process in which forecasts (e.g. the weather) can be updated with real-time observations. In order to create a *baseline* dataset of synchronic maps, we have created a data assimilation process which periodically updates the model with data from full disk magnetograms. This baseline provides the closest contact with observations by correcting for any differences be-

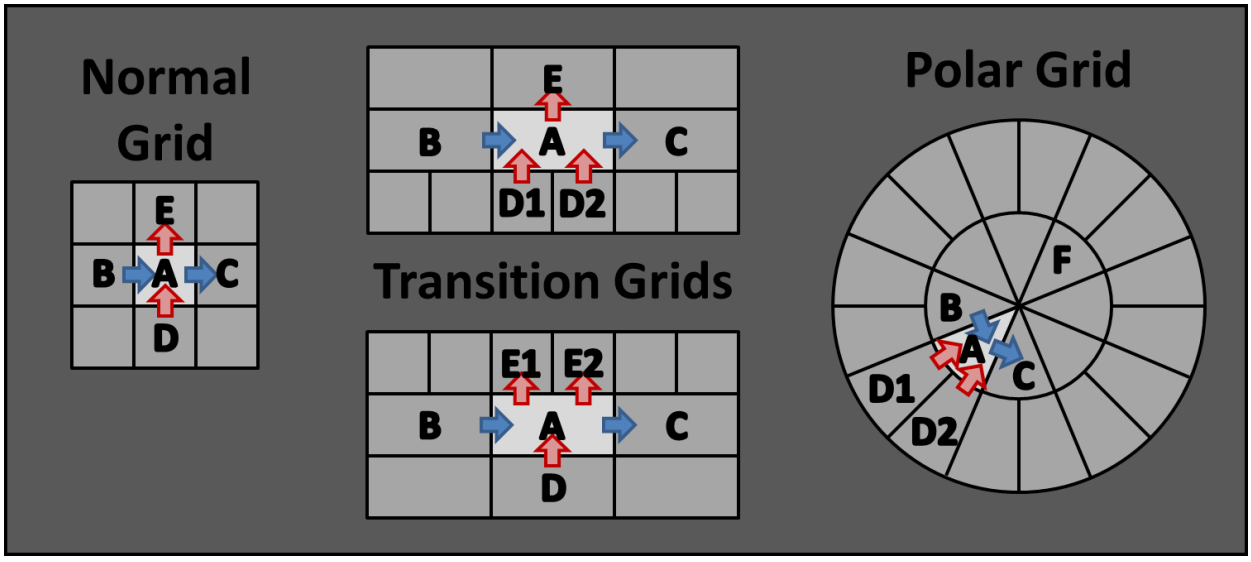

Figure 4.1: Modified Grid. We have created a modified grid with 1024 pixels at the equator, but with that number repeatedly halved at higher latitudes. In most grid positions, a normal grid (left) is used. At latitudes given by Equation (4.4) the transition grid (middle) is used. The polar grid (right) is used at both poles.

tween data and model. In regions where data were recently assimilated, the model is nearly identical to the observations. This baseline is used in Chapter 5 to examine the different methods for characterizing the polar fields and also served as a metric for evaluating simulation results in Chapters 5 and 6.

Our data assimilation process merges magnetogram observations with forecasts made by the surface flux transport model. This was done by assigning weights to both the observed data and the data forecasted by the model (shown in Figure 4.2). The observed magnetic fields have signal-to-noise ratios that degrade away from disk center so the weights for the observed data fall off as a function of center to limb distance. The weights for the forecasted data were created by adding the newly observed weights to the model weights from the previous time step and then multiplying by a latitude dependent exponential decay function. This exponential decay function was designed to account for the drift between observations and model for places and times for which observations are unavailable. The weights decay by a factor of e^{-1} in $\sim$1 week at the

rapidly evolving equator, but more slowly (up to several months) at the poles. A new map was created by adding the forecasted data multiplied by its weights to the observed data multiplied by its weights and then by dividing by the sum of the two weights.

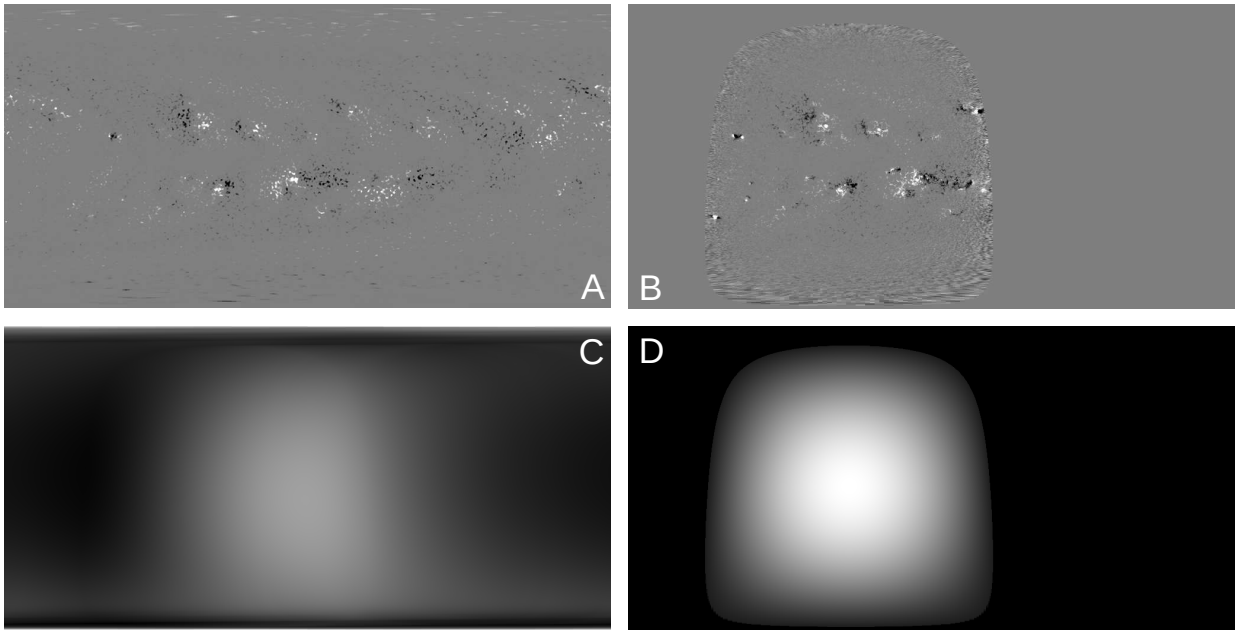

Figure 4.2: Data Assimilation. A) The data forecasted by the flux transport model. B) The data observed with a magnetograph. C) The weights for the simulated data. D) The weights for the observed data.

MDI magnetograms were assimilated from 1996 May to 2010 May with a cadence of 96 minutes (excluding the time period in late 1998 and early 1999 when MDI data was unavailable or unreliable). From 2010 May to 2013 July the HMI magnetograms were assimilated hourly. The flux in each pixel of the magnetograms was divided by the cosine of the angle from disk center in order to best approximate the assumed radial magnetic field.

Full Sun synchronic maps were retained at 8 hour intervals (times of 0, 8, and 16 hours), from 1996 May to 2013 July. A magnetic butterfly diagram was constructed by averaging B_r over

longitude for all of the synchronic maps in each solar rotation. This butterfly diagram, shown in Figure 4.3, illustrates several important details. As expected, our baseline magnetic butterfly diagram is nearly indistinguishable from a butterfly diagram constructed directly from observations (shown in Figure 1.7). In particular, an annual signal in the polar field strength is seen at high latitudes. This annual signal has been a characteristic feature of MDI, Mount Wilson Observatory (MWO) and SOLIS datasets albeit with differences depending on the instrument and spectral line used. There have been attempts (Ulrich & Tran, 2013; Jin et al., 2013) to explain the origin of this annual signal in terms of a systematic tilt of the fields, but so far no consensus has emerged for explaining the origin of this signal. Perhaps one of the most telling aspects of this annual signal is that it is either not present or too weak to be seen in the HMI data. This suggests that this annual signal could be due to changes in spatial resolution, noise levels at the poles, or possibly errors (at high latitudes) in the calculation of field strength using different spectral lines.

The baseline butterfly diagram also illustrates some important details about flux transport. Figure 4.3 shows that it takes $\sim$1-2 years for active region flux to be transported to the poles from the active latitudes. This suggests that a flux transport model should be able to reproduce the evolution of the polar field strengths at least this far in advance. Furthermore, our flux transport continued during the "SOHO summer Vacation" from 1998 June through 1999 February, i.e., a period when no data assimilation was occurring. The absence of data to assimilate resulted in the poleward transport of leading polarity flux from the lower latitudes. This demonstrates that it is essential that new active region sources continue to be added. If the active region emergence is prematurely cut off, excess leading polarity (that would have been canceled by the new emerging flux) remains and is transported to the poles along with (or just after) the following polarity flux. This has the effect of slowing down the reversal (or depending on the timing, slowing the subsequent buildup of new polarity). If enough excess leading polarity is transported to the poles, then a relapse in the polar field reversal may also be observed. In this case, the assimilation corrected for these problems once it was re-initiated in 1999 February.

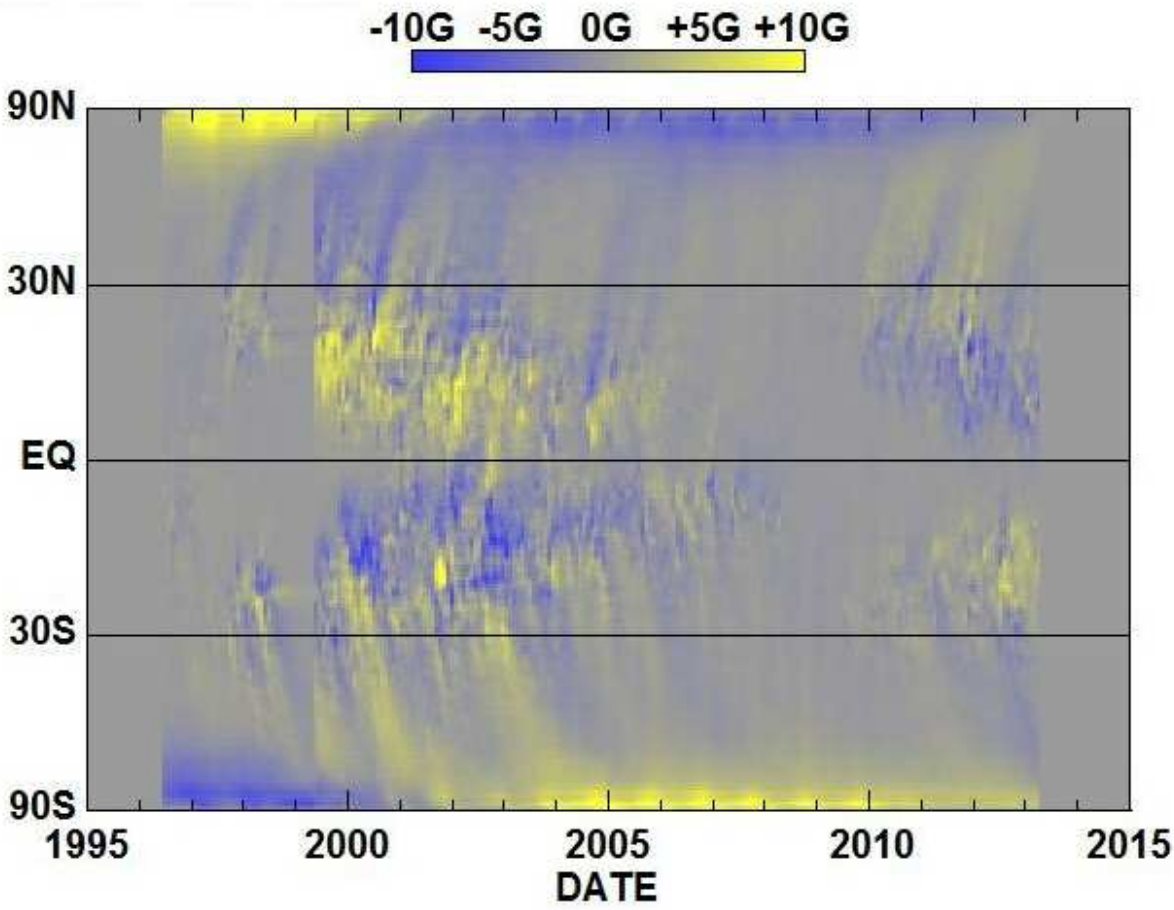

Figure 4.3: Baseline Magnetic Butterfly Diagram. Yellow (positive) and blue (negative) streamers show that it takes ∼1-2 years for active region flux to reach the poles. The "SOHO summer Vacation" from June 1998 through February 1999 illustrates the importance of continued active region emergence.

CHAPTER 5

POLAR FIELD PREDICTIONS

Obtaining a complete understanding of solar cycle variability (recall Section 1.3.1) is one of the oldest and most significant problems in solar physics. Babcock & Livingston (1958) reported the first observation of a reversal in the Sun's dipolar magnetic fields, noting that this reversal occurred near the time of solar maximum. Shortly thereafter, Babcock (1961) linked solar cycle variability to magnetism on the Sun by proposing a solar dynamo model. While Babcock's model is widely accepted as the underlying mechanism behind the solar cycle, the finer details are still not well understood.

Two points in the evolution of the polar fields stand out as being the most significant: the reversal of the polar fields and the polar fields at solar minimum (i.e. the seed to the next cycle). The reversal of the polar fields marks the time of solar cycle maximum, i.e., when solar activity peaks and then begins to wane. Furthermore, the reversal is important to galactic cosmic ray observations. Galactic cosmic ray propagation is inhibited by the magnetic fields that are threaded through the heliosphere as a result of solar activity. Furthermore, the polarity of the solar dipole changes the manner in which the positively charged cosmic rays propagate through the heliosphere (Ferreira & Potgieter, 2004). Positive cosmic rays enter from the heliospheric polar regions when the Sun's dipole is positive, but along the heliospheric current sheet when the Sun's dipole is negative. This results in cosmic ray flux with a flat peak when the Sun's magnetic dipole is positive and a sharp peak when the Sun's magnetic dipole is negative. On the other hand, the polar fields at solar minimum are thought to be the seeds to the next solar cycle. Indeed, observations have shown that the strengths of the polar fields at solar minimum are a good indicator of the strength of the next cycle (Svalgaard et al., 2005; Muñoz-Jaramillo et al., 2012; Svalgaard & Kamide, 2013). Interestingly, the polar fields leading up to the Cycle 23/24 minimum in 2008 were about half as strong as observed for the previous two cycles (Svalgaard et al., 2005). This was followed by an

extended Cycle 23/24 minimum and what is proving to be the weakest solar cycle in over a hundred years. This has caused speculation that the Sun may be entering another Maunder Minimum. With such unusual solar conditions there is increasing motivation to determine exactly how magnetic flux is transported to the poles and how the polar fields are modulated.

In this Chapter, I will introduce current techniques for characterizing the polar field strengths. I will discuss the strengths and weaknesses associated with the different techniques. I will discuss modifications to the surface flux transport model (described in Chapter 4) that will enable the simulation of the polar field evolution and the capability to make predictions of future polar field strengths. The contents of this chapter were published in (Upton & Hathaway, 2014).

5.1 Polar Fields

Magnetic maps of the entire Sun provide the ability to change the angle from which the Sun is viewed. For example, rather than look at the Sun from a near-equatorial position in the ecliptic, we can look directly down on the poles as shown in Figure 5.1. Seeing the Sun from above the poles is vital to furthering our understanding of the evolution of polar regions and their impact on the solar cycle (Shiota et al., 2012; Muñoz-Jaramillo et al., 2013). By watching the flux transport from this angle it is clear that the residual active region flux at high latitudes is substantially sheared by differential rotation. The combined effect of the differential rotation shearing and the meridional flow driving the flux poleward causes the residual flux to spiral into the pole. The polarity of this residual flux is typically opposite in sign to the polarity of the pole at the beginning of the solar cycle. When this (typically) opposite polarity flux reaches the poles it cancels with the original polar fields until it disappeared completely and the new (opposite polarity) polar field begins to build.

The polar fields are often characterized by averaging the flux density over a polar region of the Sun. However, the determination of what area is considered a polar region is rather arbitrary. For the Wilcox Solar Observatory, the polar field strengths are defined using the line of sight fields between 55° and the poles. This range is established by the resolution of the instrument. With the ad-

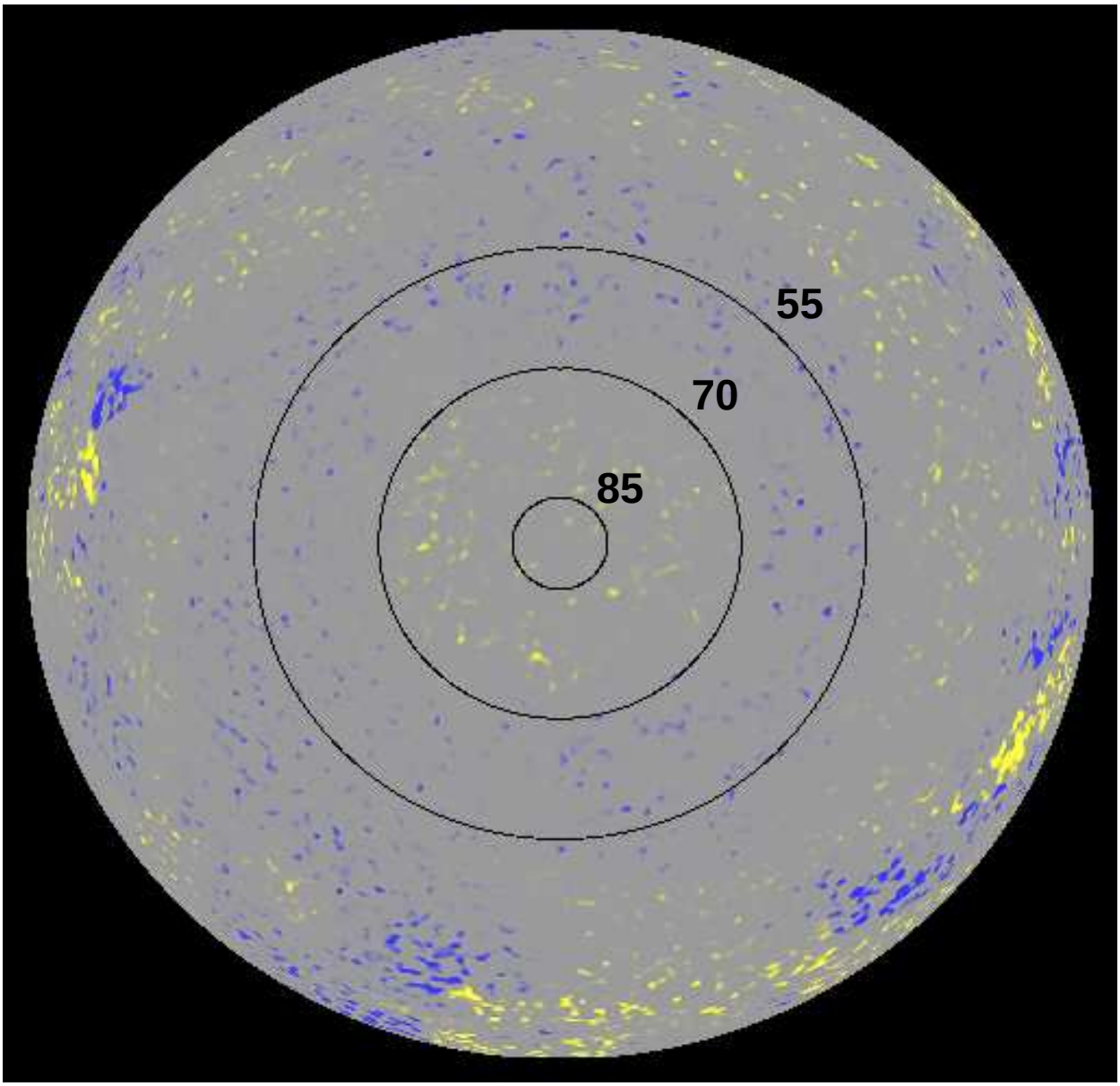

Figure 5.1: North Polar View in 2001 April. Synchronic magnetic maps allow the Sun to be seen from the perspective of looking directly down on the poles. The 55°, 70°, and 85° latitude lines used in definitions of polar fields are marked for reference.

vancements in the spatial resolution of more modern instruments, recent polar field measurements have become more restrictive in defining the polar region. For example, de Toma (2011) measured the polar fields using the radial fields between 60° and 80° latitude. Muñoz-Jaramillo et al. (2012) obtained polar field strengths by averaging the line-of-sight fields poleward of 70°. Alternatively, the polar fields can be defined by the axial component of the Sun's magnetic dipole (Svalgaard et al., 2005).

Magnetic maps of the entire Sun also provide the benefit of being able to calculate the polar field strengths using all longitudes and latitudes extending all the way to the poles. Here, we have used three different definitions of polar area (above 55°, above 70°, and above 85° latitude). These latitudes are indicated by the circular black lines in Figure 5.1. The magnetic maps made by assimilating the MDI magnetograms produced an annual periodicity in the polar field strength, due to the instrumental artifact discussed previously (see Section 4.2). Fortunately, there is almost a full year of overlap (2010 April to 2011 March) in the observations of MDI and HMI. This overlap in observations provides the opportunity to calibrate the MDI-based polar field measurements. First we smoothed the MDI-based polar field measurements using a tapered Gaussian with a full width at half maximum of 13 rotations. The smoothed MDI-based polar field measurements were then compared to the HMI-based polar field measurements. We found that the two measurements agreed when 0.5 Gauss was uniformly subtracted from the MDI-based polar field measurements. We then applied the 13-rotation tapered Gaussian smoothing and 0.5 G offset to all of the MDI data.

The corrected polar field strengths during Solar Cycle 23 maximum are shown in Figure 5.2 (top plot). For all three definitions of polar area, we find the timing of the North and South reversals are well synchronized (i.e., they occur within a couple months of each other). However, the timing of the reversal differs by $\sim$1 year depending on which definition of polar area was used. For 55° and above, the reversal comes at the end of 2000, the 70° reversal occurs in mid-2001, and the 85° reversal does not occur until the end of 2001. These results demonstrate that measuring the polar field strength over a polar area is arbitrary (because there is no formal standard as to what polar

area should be used). Furthermore, these measurements are ambiguous (they vary by as much as a year depending on what polar area is used).

The synchronic maps can also be used to calculate the axial magnetic dipole moment B_p (shown in bottom panel of Figure 5.2), where:

$$B_p = \frac{1}{2\pi} \int_0^{2\pi} \int_0^{\pi} B_r(\theta, \phi) Y_1^0(\theta, \phi) \sin\theta d\theta d\phi \tag{5.1}$$

Not surprisingly, the synchronic maps made by assimilating MDI data produced an annual signal in the magnetic dipole moment measurements as well. This annual signal was removed by smoothing with the tapered Gaussian with a full width at half maximum of 1 year (the red line in Figure 5.2). The axial magnetic dipole moment reverses sign in early 2000, almost precisely the time of the Solar Cycle 23 maximum. No data was assimilated during late 1998 and early 1999. During this time period, the axial dipole moment appears to decay very slightly and is followed by a sudden jump when data assimilation is re-initiated. For this time period in particular (and a few months afterwards) the smoothed dipole moment appears to be a better measure of the axial dipole moment on the Sun.

We find that the axial dipole moment appears to be a better metric for analyzing the relationship between the polar fields and the solar activity cycle. First of all, the axial dipole moment depends on the magnetic field over the entire Sun rather than over some arbitrarily defined polar area. Therefore the axial dipole moment is less ambiguous metric. Secondly, the polar field strengths can become asymmetric if active region emergence is asymmetric. This asymmetry is certainly an interesting and important aspect of the solar dynamo; however the role, if any, that these asymmetries play in modulating the solar activity cycle is uncertain. These hemispheric asymmetries are short lived, usually disappearing in less than a year or two (Norton & Gallagher, 2010). As the axial dipole moment reflects the magnetic state of the Sun as a whole, it is not as sensitive to these hemispheric differences. Furthermore, the timing of the axial dipole moment reversals appears to be better correlated to the timing of the solar cycle maximum. The smoothed Wilcox Solar Obser-

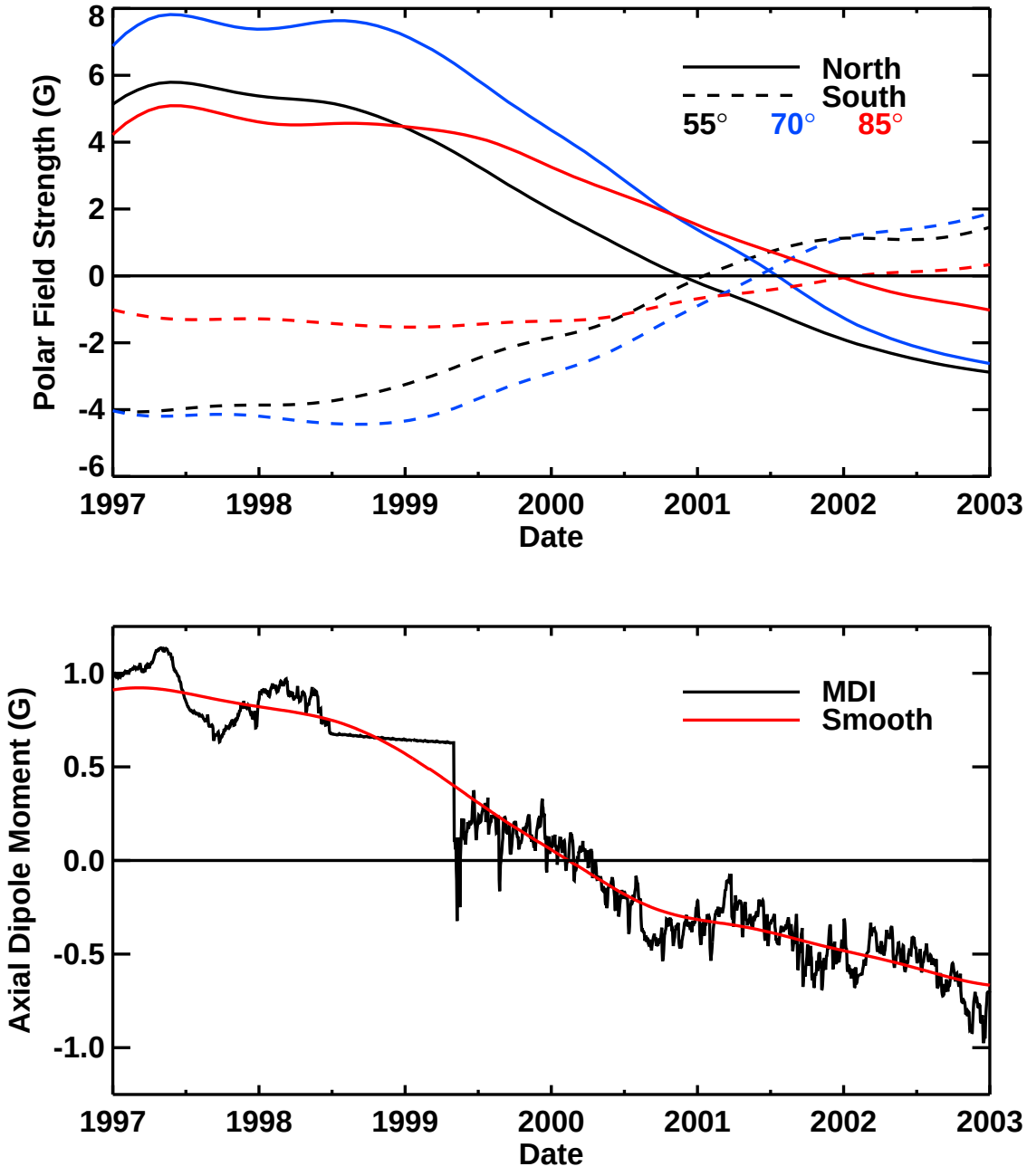

Figure 5.2: Polar Field Reversals. The corrected North (solid) and South (dashed) polar field strength reversals (top) are shown for three different definitions of polar area: $> 55°$ in black, $> 70°$ in blue, and $> 85°$ in red. The timing of the reversal depends greatly on which polar area is used, with $\sim$1 year between the $55°$ reversal and the $85°$ reversal. This behavior is consistent with the notion of new polarity flux spiraling in and canceling the old polarity flux residing in the polar cap. The reversal of the axial dipole moment (bottom) occurs early in 2000. The raw data (black) is contaminated by an annual signal in the MDI data. The smoothed axial dipole moment is shown in red.

vatory axial dipole moment reversed in 1979 November, 1989 December, and 1999 October. A 13 month running mean of the International Sunspot Number shows these reversals nearly coincide with solar maximum: 1979 December, 1989 July, and 2000 April. In the case of the later two, the axial dipole moment reversals actually precede solar cycle maximum by a few months, further indication that the dipole moment is a key measure of the dynamo process.

5.2 Predictive Model: Active Region Sources

In order to be used for predictive purposes, we need to the modify surface flux transport model presented in Chapter 4. Detailed predictions of the emergence of active region flux are not possible at this time. However, reliable predictions of the number of active regions and the latitudes at which they emerge are available once a cycle is underway (Hathaway, 2010). These predictions (or active region data from similar sunspot cycles) can be used to provide the active region sources for the flux transport model. In addition, the synchronic maps used as initial conditions need to be adjusted to remove the annual signal described above.

An initial synchronic map is needed to begin a prediction. Synchronic maps generated using the MDI data had the previously described annual signal. The nature of this annual signal is still not fully understood so properly correcting the full disk magnetograms is not feasible at this time. This flux error would propagate through the simulation and cause errors in the polar field strength measurements. The annual signal can, however, be removed from the axial dipole moment component. We have done this by measuring the axial dipole moment present in each synchronic map during the MDI time period (1996 May to 2010 May), smoothing it with the 1-year tapered Gaussian, and producing a new set of maps using the smoothed axial dipole moment. The annual signal did not appear in the HMI data, and so these steps are not necessary when a synchronic map generated from HMI data is used to initialize the simulation.

We simulated active region emergence by adding bipolar Gaussian spot pairs in the locations of the active regions. The Royal Greenwich Observatory (RGO) and the National Oceanic and Atmospheric Administration (NOAA) sunspot records provide information about the sizes and locations

of nearly all the sunspot groups that have been observed since 1874 (Solar Cycles 12-24). We used these databases to characterize the active regions in terms of size, location, and longitudinal separation. The flux was calculated as a function of reported area using the relationship described by Sheeley (1966) and confirmed by Mosher (1977):

$$\Phi(A) = 7.0 \times 10^{19} A \tag{5.2}$$

where $\Phi(A)$ is the magnetic flux in Maxwells and A is the total sunspot area in units of micro Hemispheres (1 μHem = 3×10^{16} cm^2). The tilt was given by the average Joy's Law tilt, i.e., the angle between the bipolar spots (with respect to lines of latitude) is equal to one half of the latitude. While the NOAA sunspot record (1974 to present) includes both the sunspot area and longitudinal extent, the RGO data only include the sunspot area. Using the NOAA data, we found a relationship between the area of the sunspot group and the longitudinal extent (shown in Figure 5.3):

$$\Delta\phi(A) = A\frac{17}{2000} + 7\tanh\frac{A}{70} \tag{5.3}$$

where $\Delta\phi$ is the longitudinal extent in degrees and A is the group sunspot area in micro Hemispheres. This equation was used to set the longitudinal separation of the bipolar spots added to the simulation from the sunspot database.

Lastly, instead of using the measured flows for each rotation in the flux transport, we used our average axisymmetric flows to create the vector velocities in these prediction simulations. Alternatively, we could generate meridional flow profiles that have the observed systematic solar cycle variations (Basu & Antia, 2003; Hathaway & Rightmire, 2010). Chapter 6 will investigate the importance of these systematic meridional flow variations in this flux transport model.

To demonstrate the viability of this predictive flux transport model, we simulated the magnetic field evolution for the three years leading up to the Solar Cycle 23/24 minimum using the active regions from Solar Cycle 23. We repeated the simulation five times, using different realizations of the supergranular flows. Statistically these realizations all had cellular flows with the same

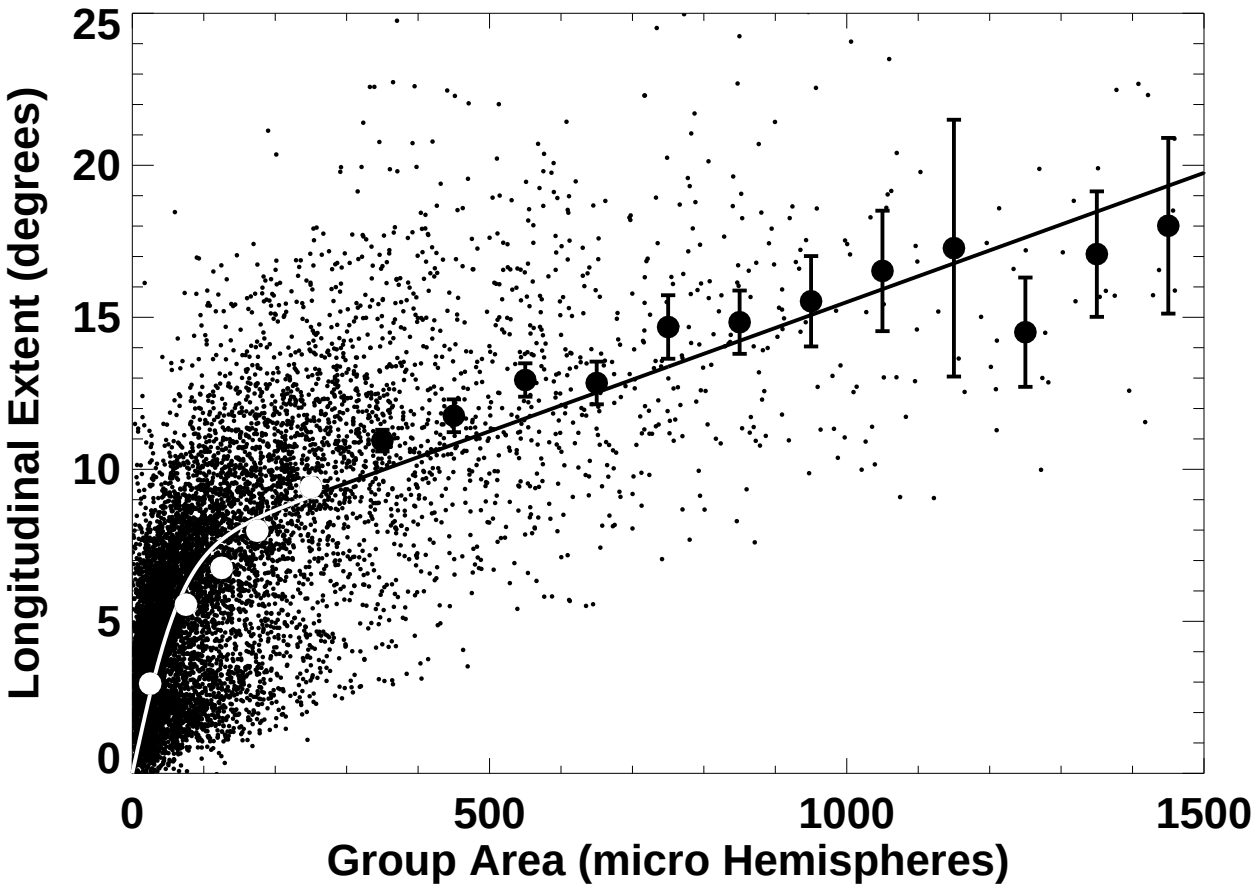

Figure 5.3: Longitudinal Extent of Sunspot Groups. NOAA data from 1995 to 2013 was used in this plot of the longitudinal extent of individual sunspot groups as a function of group area. The large dots show the averaged binned data with 2 sigma errors. Equation (5.3) is shown as the solid line.

characteristic sizes and lifetimes, but certain details of the individual cells were changed (e.g. their locations relative to active region flux concentrations).

All five realizations of the axial dipole moment evolution are shown in Figure 5.4. For comparison, the unsmoothed baseline axial dipole moment is shown by the dashed black line. All of the realizations are in good agreement, showing a dipole moment that coincides almost precisely with the baseline dipole moment. The increase in the spread of the measurements over time highlights the stochastic nature and important role that supergranules play in the transport of flux. The random details of individual cells can produce variations in the dipole moment on timescales of years,

but this variation is significantly smaller than the variation due to the annual signal carried over from the MDI data. Despite these stochastic variations, the flux transport demonstrates its functionality and potential for predicting the polar fields three years (and perhaps longer) in advance of the solar cycle minimum.

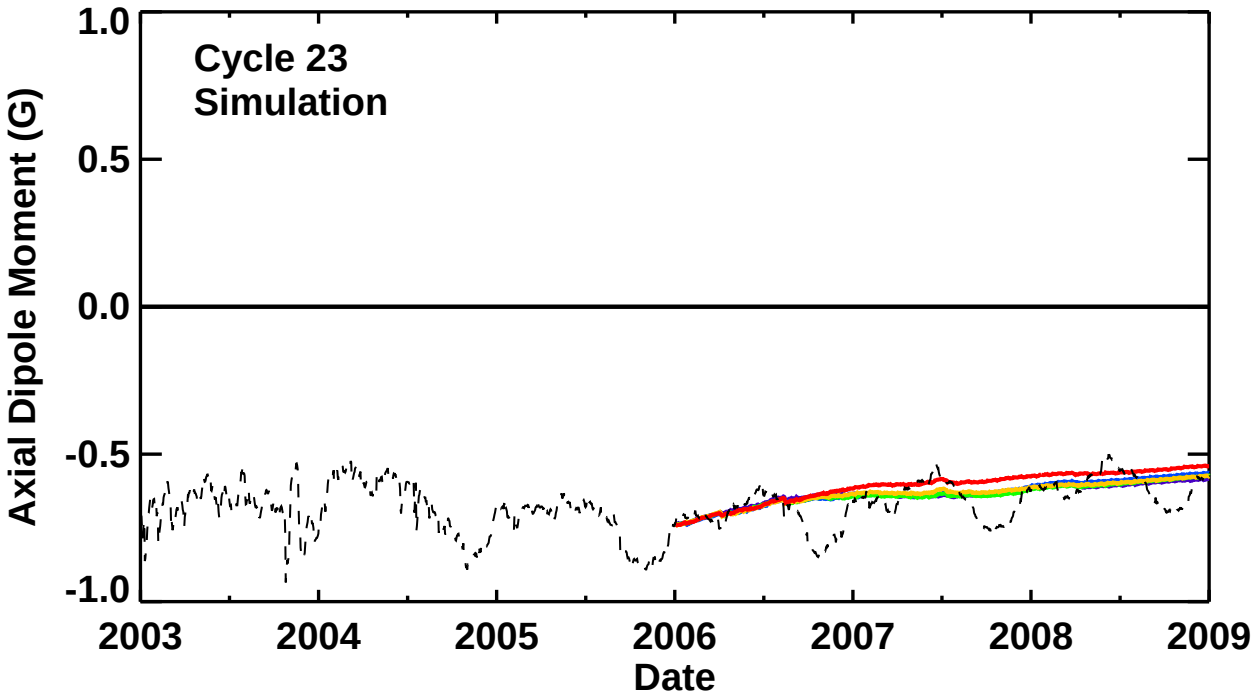

Figure 5.4: Predictions of Cycle 23/24 axial dipole moment approaching minimum using Cycle 23 active regions starting ∼three years ahead of the observed minimum. The five different supergranule realizations are represented by the solid lines shown in color. For reference the unsmoothed MDI axial dipole moment is shown with a black dashed line.

5.3 Prediction Test - Cycle 23 Using Cycle 17 Active Regions

We have tested the predictive abilities of our flux transport model by attempting to reproduce the axial dipole moments of Solar Cycle 23 using proxy data for the active region sources. Solar Cycle

17 most closely matched the amplitude and shape of Solar Cycle 23 (shown in Figure 5.5) and was used as a proxy for Solar Cycle 23 active region emergence. Two primary points of interest during the solar cycle were investigated: Solar Cycle 23/24 minimum (the end of 2008) and the reversal of the polar fields during Solar Cycle 23 maximum (spring of 2000). In both cases the model started with a lead time of ∼three years and five different realizations of the convective motions were used. The simulation of the polar field reversal ran until the end of 2002, to ensure that the reversal was fully captured.

Our predictions of the approach to the Solar Cycle 23/24 minimum using Cycle 17 active region data (SC23AR17) is shown in the top panel of Figure 5.6. For comparison, the baseline axial dipole moment is shown by the dashed black line. The SC23AR17 prediction is fully consistent with the baseline. For the first two years, the axial dipole moments are nearly identical to the axial dipole moments that were simulated using the Cycle 23 active regions (SC23AR23, Figure 5.4). For the last year, the SC23AR17 prediction begins to diverge somewhat from the SC23AR23 simulation. This divergence is small in comparison to the annual signal variation seen in the baseline.

Our predictions of the SC23AR17 dipole moment reversal is shown in the bottom panel of Figure 5.6. All of the realizations (made with a lead time of ∼three years ahead) predicted the timing of the reversal to within four months of the baseline axial dipole moment reversal. Four of the realizations predict the timing of the reversal almost precisely (to within a month). The fifth realization places the reversal about four months late. Surprisingly, the amplitude of the dipole moment (in 4 of the five realizations) stays in remarkably good agreement with the baseline through to the end of the prediction (some six years after the prediction start time).

Comparison of the model predictions during the two different phases of the solar cycle shows that the spread of the measurements (due to the stochastic nature of supergranules) is more pronounced in the prediction for the dipole moment reversal (i.e., solar maximum) than the for prediction of the dipole moment amplitude leading up to solar minimum. This is due to the fact that much more flux is being added to the model during solar maximum. With more flux being advected the random motions of the convective cells have a pronounced effect. This suggests that predictions

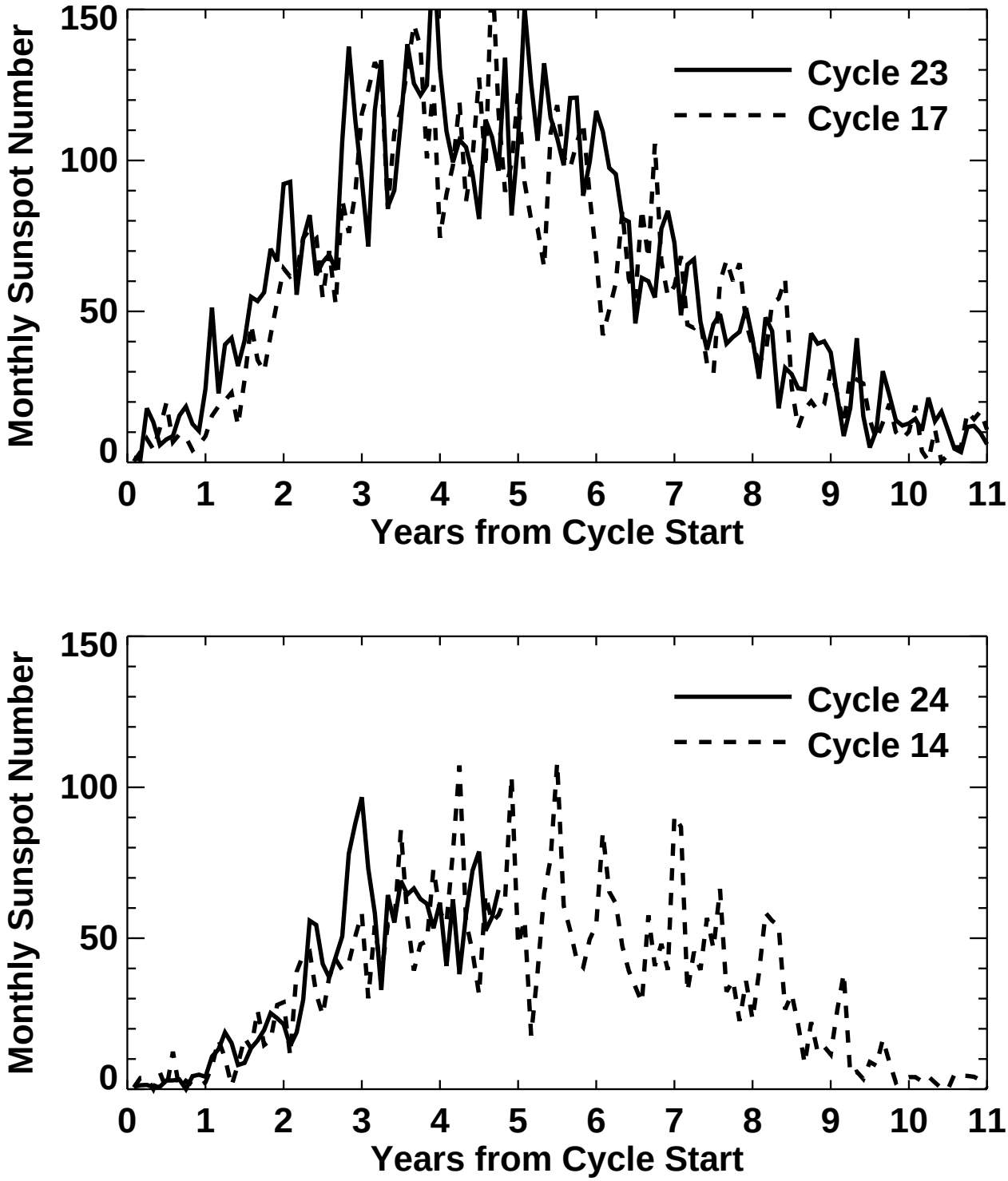

Figure 5.5: Solar Cycle Proxies. Active region sources are simulated by using prior solar cycles as proxies for the modeled cycles. Solar Cycle 17 is chosen as a proxy for Solar Cycle 23 (top). Solar Cycle 14 is chosen as a proxy for Solar Cycle 24 (bottom).

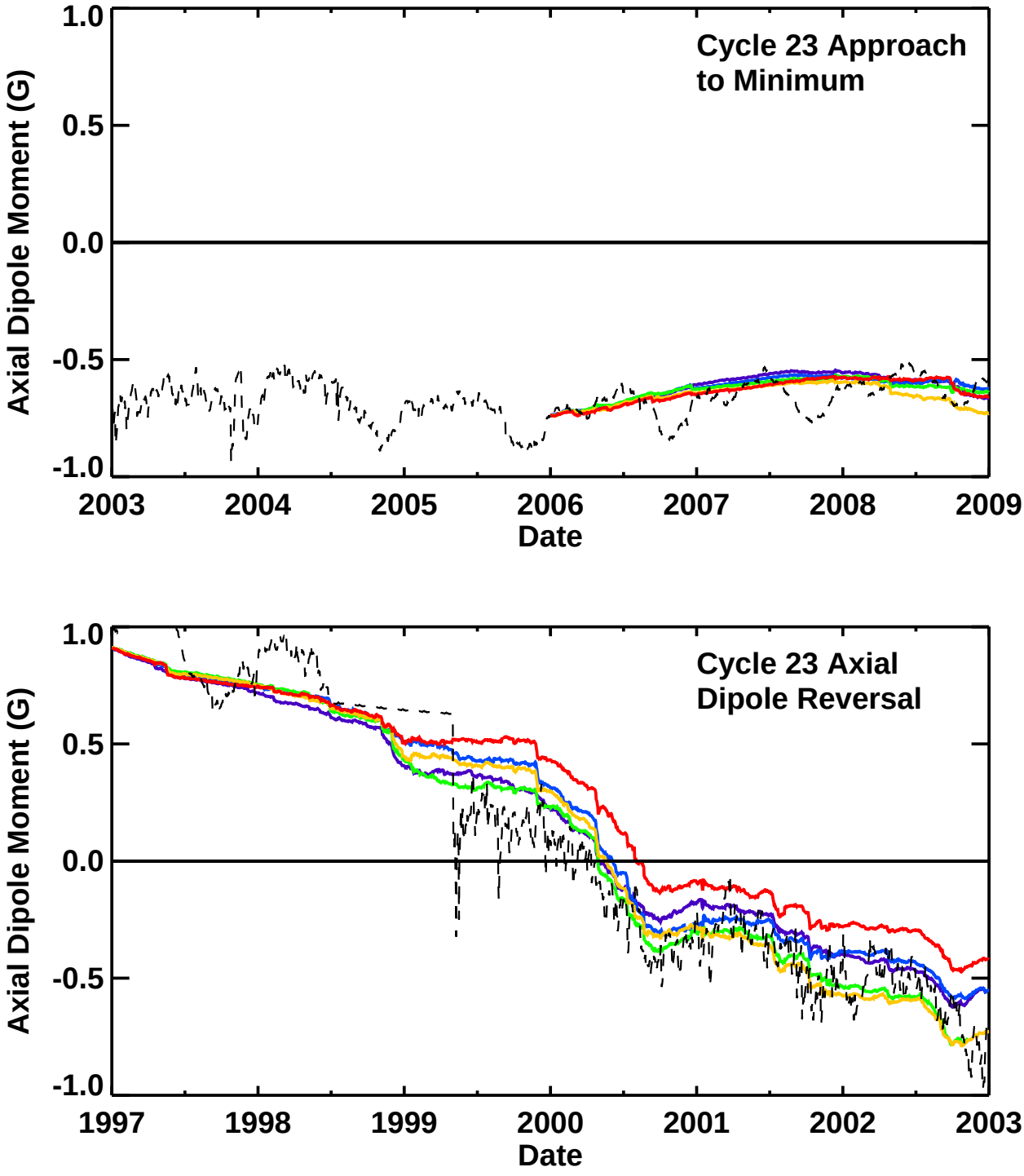

Figure 5.6: Predictions of Cycle 23 with Cycle 17 active regions. Axial dipole moment predictions of Cycle 23/24 minimum made with Cycle 17 active regions and a start time of ∼three years (top). Axial dipole moment predictions of Cycle 23 polar fields reversal made with Cycle 17 active regions and a start-time of ∼three years (bottom). In both cases, the five different realizations are represented by the solid lines shown in color. For reference the unsmoothed MDI axial dipole moment is shown with a black dashed line.

made during times of solar maximum are more difficult to make than predictions made near solar minimum.

5.4 Prediction for Cycle 24 Reversal

We used the flux transport model to predict the Solar Cycle 24 axial dipole moment reversal and subsequent magnetic field buildup. Solar Cycle 14 was chosen to act as a proxy for continued active region emergence (see Figure 5.5, bottom). The flux transport is identical to the flux transport used in our Cycle 23 prediction: using the average axisymmetric flows and the five different supergranule realizations. The prediction started on 2013 August 1 and ran until 2016 December 31.

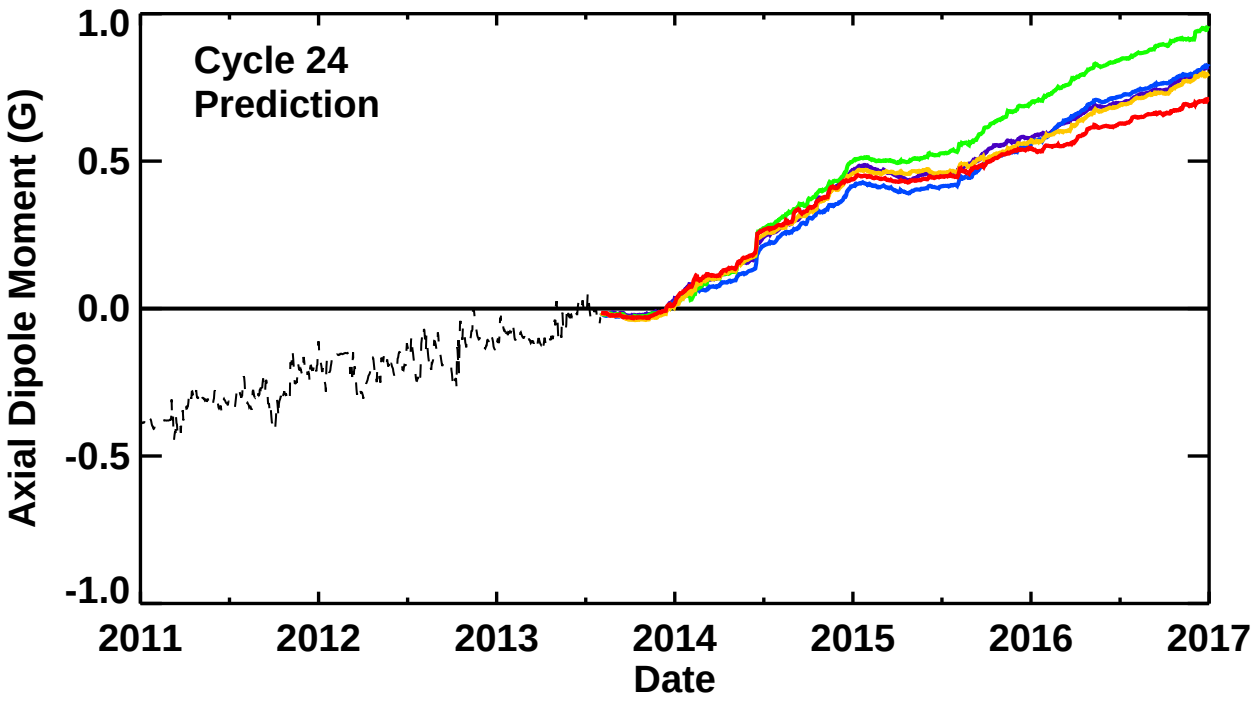

Figure 5.7: Predictions of Cycle 24 with Cycle 14 active regions. Axial dipole moment predictions of Cycle 24 dipole moment reversal made with Cycle 14 active regions. For reference the observed HMI axial dipole moment is shown with a black dashed line.

Our Solar Cycle 24 axial dipole moment prediction (see Figure 5.7) shows the dipole moment stalling for a few months before the reversal occurring in December of 2013. The subsequent magnetic field buildup is similar to the buildup observed during Solar Cycle 23. This would suggest that Solar Cycle 25 might be similar in amplitude to Cycle 24. However, it is the axial dipole moment *at solar minimum* that is the best indicator of the amplitude of the coming cycle. Minimum is not expected to occur until around 2020 or 2021. Predictions made 2-3 years prior (2017-2019) will provide a more accurate estimate of the amplitude of Cycle 25.

5.5 Discussion

Understanding the Sun's surface magnetic field evolution, including the buildup of the polar fields and subsequent magnetic reversals, is essential to deciphering the sunspot cycle. Previous surface flux transport models have been used to investigate the role of surface flows and active region emergence in the surface magnetic field evolution, but all have used contrived meridional flow profiles and have parameterized the advection by supergranules with a diffusion coefficient. I have used a new flux transport model to investigate metrics for defining the polar field reversals and to test the predictions of the polar fields at different phases of the solar cycle.

We found the axial dipole moment to be the best indicator of the reversal of the Sun's magnetic field. Determinations of the polar field reversals varied by as much as a year when using different definitions of polar area. Though it does not capture asymmetries in the polar fields, the axial dipole moment (as opposed to the polar area) provides a metric for characterizing the evolution of the polar fields that is neither ambiguous nor arbitrary. More importantly, the axial dipole moment reversal more closely reflects the timing of solar maximum. The timing of this reversal is critical for the propagation of galactic cosmic rays in the inner solar system. In the case of the synchronized Solar Cycle 23 polar field reversals, the axial dipole moment occurs before both the North and South reversals. Solar cycle 24 is currently experiencing an extreme asymmetry in the polar field reversal: the North has already reversed and the South is not expected to reverse until 2014. In this case the timing of the axial dipole moment reversal occurs between the North and

South reversals.

We used the predictive flux transport model with Solar Cycle 23 active regions to simulate the evolution of the polar fields during the three years leading up to the Solar Cycle 23/24 minimum. The flux transport model was able to reproduce the observed axial dipole moment without the annual signal created by a presumed instrumental effect of MDI (see Section 4.2). Our supergranule flows introduce stochastic variations in the flux transport that are not captured by a diffusivity term. During this time period the stochastic nature of supergranular motions created minimal variations.

We then used the predictive flux transport model with Solar Cycle 17 active regions to examine the predictive ability of the model for two different phases of the solar cycle. The first two years of results using Solar Cycle 17 for the three years leading up to the Solar Cycle 23/24 minimum were nearly identical to the results that used the Solar Cycle 23 active regions. While the results for the last year were somewhat divergent, they were still consistent with the baseline results. Further testing should be done to illustrate the impact of using different active region sources or a varying meridional flow. Our flux transport model was able to reproduce the timing of the polar field reversal of Solar Cycle 23 to within a few months at least three years in advance. We showed that the stochastic nature of supergranular motions had a larger effect during this phase of the cycle.

Our results for the Solar Cycle 24 predictions show a reversal of the axial dipole moment in 2013 December. After the reversal, the axial dipole moment exhibits a rise similar in slope to the rise that followed the Cycle 23 axial dipole reversal. While this may be an early indication that Cycle 25 will be similar to Cycle 24, predictions made within 2-3 years of the coming minimum (estimated to be 2020 or 2021) will provide a more accurate estimate of the amplitude of Cycle 25.

CHAPTER 6

EFFECTS OF FLUX TRANSPORT ON THE SOLAR ACTIVITY CYCLE

The polar fields during the last solar minimum (Cycle 23/24 minimum) were the weakest to date, at about half the strength of the prior two cycles. This minimum was extended in duration and Solar Cycle 24 (the current solar cycle) is developing into the weakest solar cycle in the last century. The weak polar fields of this extended minimum may be caused by variations in surface flux transport. On the Sun, flux transport is achieved via differential rotation, meridional circulation, and the turbulent motions of convection. While the convective motions and differential rotation are fairly constant, the meridional flow varies in two fundamental ways: over the course of a solar cycle and from one cycle to the next, as shown in Chapter 3. The meridional flow is faster at solar cycle minimum and slower at maximum. Furthermore, the meridional flow speeds that preceded the Solar Cycle 23/24 minimum were $\sim$20% faster than the meridional flow speeds that preceded the prior minimum (recall Figure 3.13). It has been suggested that this faster meridional flow may have led to the weaker polar field strengths of Solar Cycle 23/24 and thus the subsequent extended solar minimum and a weak Cycle 24 (Wang et al., 2009; Hathaway & Rightmire, 2010, 2011). In this Chapter, I will use our Surface Flux Transport model to investigate possible causes of the weak Cycle 24, and the importance of the variations in the meridional flow in particular.

6.1 Analysis

We used the predictive model (described in Section 5.2) in three simulations to determine the impact of meridional flow variations on the sunspot cycle. Each simulation was run from 1997 January through 2013 July. The RGO and NOAA active region databases were used to characterize and simulate the emergence of observed active regions by adding bipolar Gaussian spot pairs in the location of the active regions. These active regions sources were constructed with total flux,

longitudinal separation, and characteristic tilt based on the observed statistics of these properties.

All three models used the same average, constant, North-South symmetric differential rotation, given in terms of latitude (λ) by

$$v_\phi(\lambda) = [a + b\sin^2(\lambda) + c\sin^4(\lambda)]\cos(\lambda) \tag{6.1}$$

with

$$\begin{aligned} a &= 39 \text{ m s}^{-1} \\ b &= -244 \text{ m s}^{-1} \\ c &= -374 \text{ m s}^{-1} \end{aligned} \tag{6.2}$$

The supergranule realization used was nearly identical for all three simulations. The size, lifetimes, and initial location of each cell were the same. However the latitudinal motions of the convective cells were modulated by the meridional flow applied to each simulation. The meridional flow for each simulation was updated at six month intervals.

The first simulation (hereafter referred to as *Sim 1*) included an average, constant, North-South antisymmetric meridional flow given by

$$v_\theta(\lambda) = [a\sin + b\sin^3(\lambda) + c\sin^5(\lambda)]\cos(\lambda) \tag{6.3}$$

with

$$\begin{aligned} a &= 24 \text{ m s}^{-1} \\ b &= 16 \text{ m s}^{-1} \\ c &= -37 \text{ m s}^{-1} \end{aligned} \tag{6.4}$$

The second simulation (*Sim 2*) included a meridional flow with the observed variations in time as described in Chapter 3. In the third simulation (*Sim 3*), the differences between the average

meridional flow and the observed meridional flow were doubled to amplify the variations in the meridional flow. The meridional flows in Sim 2 and Sim 3 included additional terms to account for the observed North-South asymmetries - most notably the polar counter-cells observed by MDI. For reference, the meridional flows for all three simulations are shown as functions of time in Figure 6.1. For additional context, the difference histories are shown in Figure 6.2.

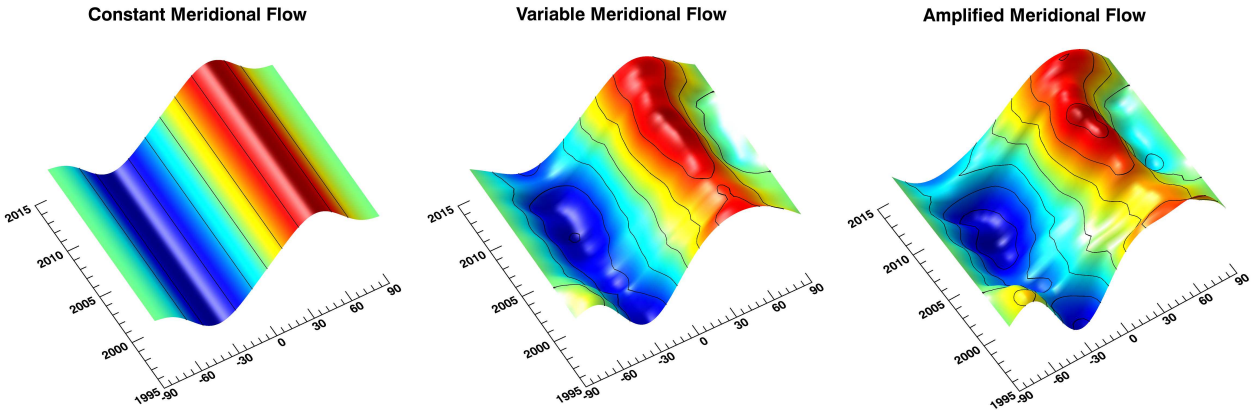

Figure 6.1: Variations in the meridional flow. The constant North-South antisymmetric meridional flow used in Sim 1 is shown in on the left. The observed meridional flow used in Sim 2 is shown in the middle. The amplified meridional flow is shown on the right. Red is northward flow and blue is southward flow.For reference the contours (black lines) show 0, ± 5, ± 10,± 15 m s^{-1}.

6.2 Results

Each simulation produces synchronic maps (magnetic flux maps of the entire Sun) with a cadence of 15 minutes. We used these maps to calculate the axial magnetic dipole moment B_p at each time step using Equation (5.1). The axial dipole moment measured for each simulation is plotted in Figure 6.3, along with the observed MDI/HMI axial dipole moment obtained from the baseline (see Section 4.2). To provide context, the magnetic butterfly diagram of each simulation is shown in Figure 6.4. The baseline magnetic butterfly diagram is also shown for comparison.

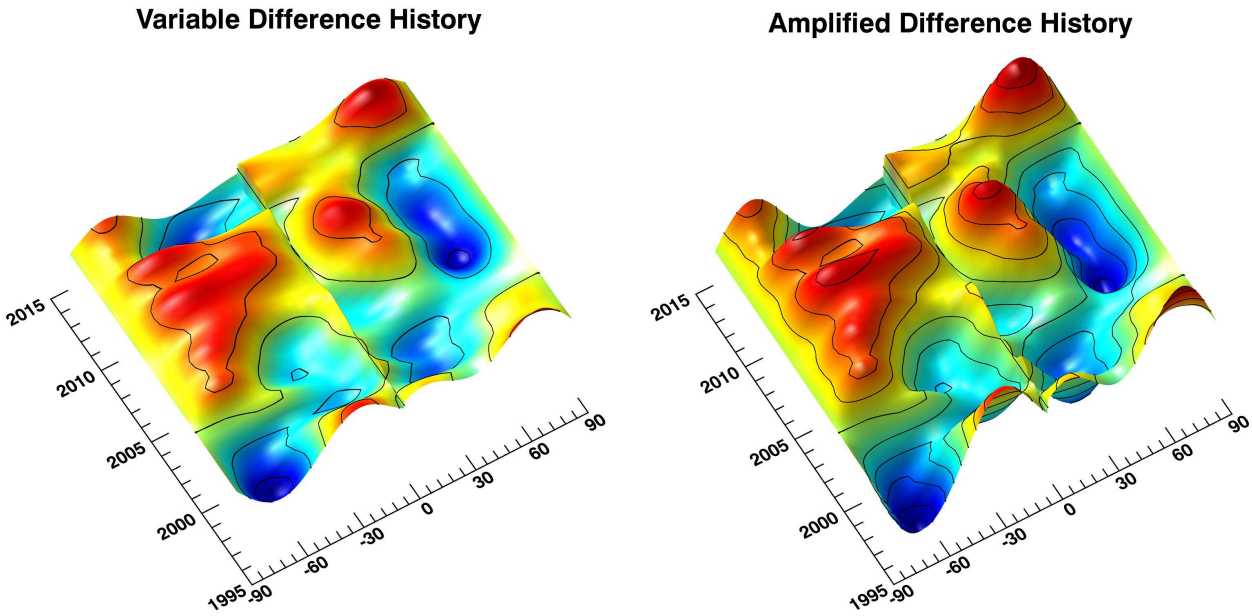

Figure 6.2: Differences in the meridional flow. The difference between the variable and constant meridional flow is shown on the left. The difference between the amplified and constant meridional flow is shown on the right. Red is poleward flow and blue is equatorward flow. For reference the contours (black lines) show 0, ± 2, ± 4,± 6, ± 8 m s^{-1}.

Immediately, inspection of the axial dipole moment plot reveals that the dipole moments in the simulations reach amplitudes about twice as strong as the observed axial dipole moment. Remarkably (and despite this) the timing of the Solar Cycle 24 reversal is accurate to within about a year. This suggests that the active region sources are being over-estimated for both the Solar Cycle 23/24 buildup and the Cycle 24 reversal. An adjustment to the amount of flux added per unit area (see Equation (5.2)) may improve the model to the point that the axial dipole moment for an entire solar cycle can be reproduced with the predictive model (see Section 5.2).

Surprisingly, rather than producing weaker polar fields, the variable meridional flow produced a stronger axial dipole moment. This effect was more pronounced with the amplified meridional flow. A detailed comparison of the strengths of the dipole moments reveals several distinct phases of interest:

1. In all cases, the axial dipole is well matched for the first three years as the dipole steadily

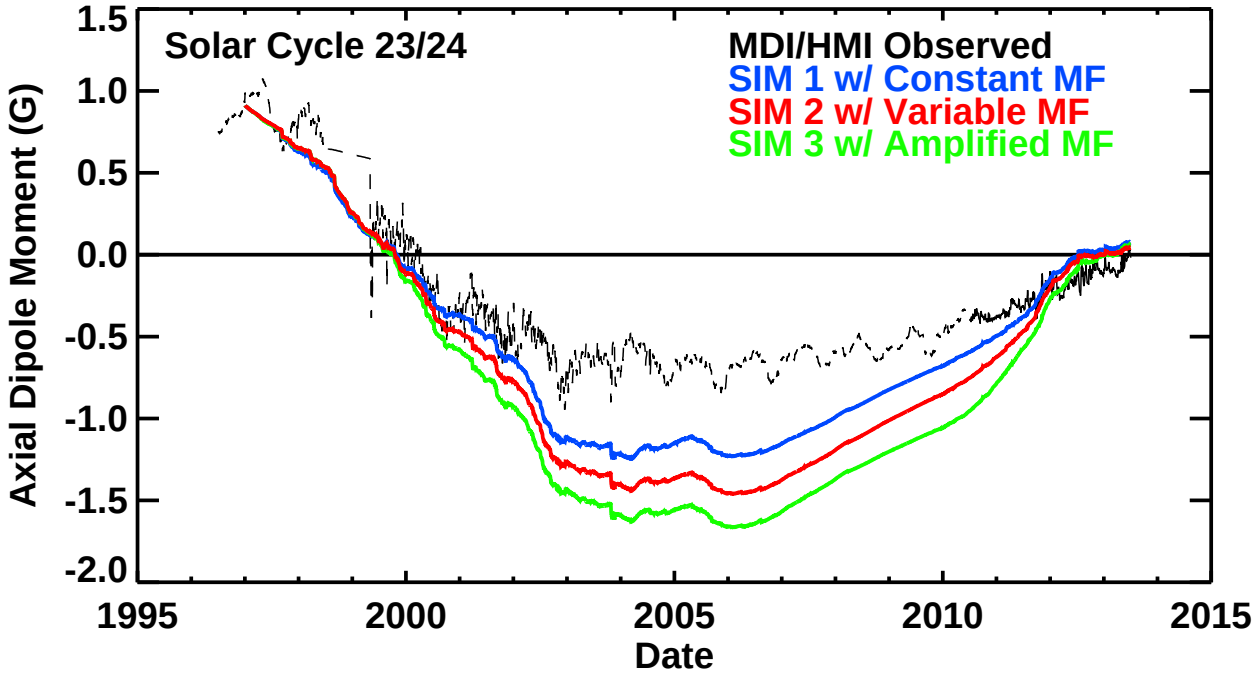

Figure 6.3: The evolution of the axial dipole moment (color) with different meridional flow profiles. MDI/HMI observations (black dashed/solid) are shown for comparison. The simulation with the observed variations in the meridional flow (red) produces an axial dipole moment at minimum that is approximately 20% stronger than the simulation that used the constant average meridional flow profile (blue).

and rapidly reverses polarity.

2. During 2000-2003, the dipole continues to rapidly build, but the simulations begin to diverge from one another, with the slower meridional flow producing the strongest axial dipole.

3. During 2003, the strengthening of the axial dipole continues at a slower rate.

4. In 2004 and 2005, the axial dipole of all three simulations weakens before rebounding slightly.

5. Between 2006 and 2011, all three simulations weaken slowly at about the same rate.

6. From 2011 to the end, a phase of active reversal occurs with fastest meridional flow reversing the axial dipole fastest.

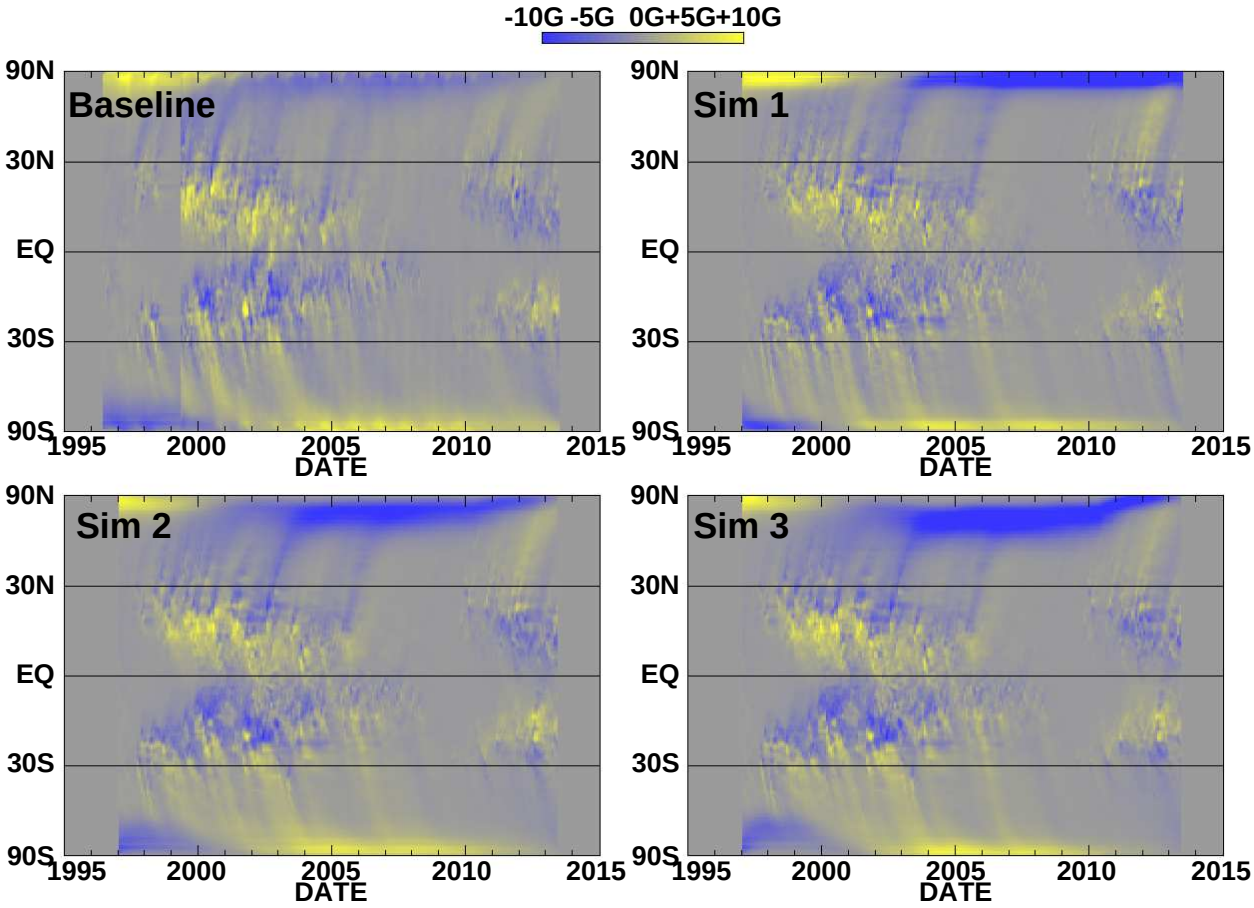

Figure 6.4: Magnetic Butterfly Diagrams from Simulations. These magnetic butterfly diagram illustrate the evolution of magnetic flux in the baseline and the simulations. The baseline is shown on the top left. Sim 1 (top right) used a constant axisymmetric meridional flow. The observed meridional flow was used in Sim 2 (bottom left). Sim 3 (bottom right) used the observed meridional flow multiplied by 1.5.

Each of these phases illustrates the importance of different aspects of flux transport. More importantly, they are indicative of the complex interplay that occurs depending on the specific details of each of these aspects. While the axial dipole plot alone clearly shows that the variations in the MF over cycle 23 have a significant impact ($\sim$20%) on the strength of the polar fields, the specifics are more elusive. In some phases the change in the meridional flow has a large impact and causes the simulations to diverge. In other phases, the change in the meridional flow appears to have no impact at all. To provide context one must also closely inspect the magnetic butterfly

diagram of each simulation (Figures 6.4). With this added context, each of these phases sheds light on the complexity of surface flux transport.

In all cases, the axial dipole is well matched for the first three years as the dipole steadily and rapidly reverses polarity. This primary reversal stage is caused by the onset and rise of the solar activity cycle. In this stage, the changes in the meridional flow appear to have little effect, instead it is the steadily increasing active region emergence combined with Joy's Law (Hale et al., 1919) and Spörer's Law that have the biggest impact. (Joy's Law is the characteristic tilt of bipolar active regions such that the leading polarity is more equatorward than the following polarity and Spörer's Law says that active region emergence progresses towards the equator over the course of the cycle.) The following polarity of newly emerging active regions cancels and exceeds the leading polarity of the older active regions. The excess following polarity flux is transported to poles where it cancels with the Sun's dipole field. During this phase, the reversal of the axial dipole is dominated by the details of active region emergence.

During 2000-2003, the dipole continues to rapidly build, but the simulations begin to diverge from one another, with the slower meridional flow producing the strongest axial dipole. This is the primary building phase for the axial dipole moment. During this phase, the variable meridional flow is weaker than the constant meridional flow (see Figure 6.1). This slower meridional flow allows for more diffusion and more cross-equator cancellation, resulting in a larger excess of following polarity. This effect is apparent when the leading polarity poleward streams are compared in one Sim to the next. These streams become significantly weaker from Sim 1 to Sim 2 to Sim 3. (The nature of these streams of leading polarity fields is discussed later.)

During 2003, the strengthening of the axial dipole continues at a slower rate. At this point, solar cycle maximum has come and gone and the rate of active region emergence begins to wane. With less excess polarity flux to be transported to the poles, the polar field build up continues, albeit at a much slower pace. In the magnetic butterfly diagrams, this appears as poleward streams giving way to diffuse flux.

In 2004 and 2005, the axial dipole of all three simulations weakens before rebounding slightly.

A break in active region emergence causes leading polarity flux to permeate the diffuse flux being transported to the poles, causing a slight weakening in the axial dipole moment. This is followed by a burst of very strong bipolar active regions produced late in the cycle. This spike in flux causes the simulations to diverge from the observations even more. Inspection of the magnetic butterfly diagram shows a poleward stream that is much stronger in the simulations than the baseline during this time. This is further evidence that perhaps too much flux is being incorporated into the simulations.

Between 2006 and 2011, all three simulations weaken slowly at about the same rate. During this phase, solar minimum is occurring and very little flux is emerging in the form of active regions. Without flux to transport, meridional flow has little to no effect. Instead, turbulent motions slowly erode the flux at the poles and the axial dipole moment gradually decays. It is the polar field strengths during this phase that have been linked to the amplitude of the next cycle. At this point the axial dipole moment of the simulation with the variable meridional flow (Sim 2) is about $\sim$20% larger than was obtained with the constant meridional flow (Sim 1). The axial dipole moment in the simulation with the amplified meridional flow (Sim 3) is about another $\sim$20% larger. Without the presumed excess flux from active region emergence, this effect may have been even more significant ($\sim$30-50%).

From 2011 to the end, a phase of active reversal occurs with fastest meridional flow reversing the axial dipole fastest. From 2010 to the end, a phase of active reversal occurs with Sim 3 reversing the fastest and Sim 1 reversing the slowest. One would expect this phase to be identical to the first phase. However, the influence of the meridional circulation variations appear to be more significant in this phase than was observed in the first phase. While a steady rapid reversal occurs in all three simulations, Sim 3 reverses the dipole the fastest, whereas Sim 1 is the slowest. This increase in the importance of the meridional flow may be due to the weakness of solar cycle 24. (Note: There are no polar counter-cells during this phase.)

A comparison of the simulated magnetic butterfly diagram with the baseline illustrates great potential for our flux transport model. The simulated magnetic butterfly diagrams are detailed and

for the most-part extremely realistic. The mottled pattern produced by active region emergence (i.e. the butterfly 'wings') are very well reproduced, with distinct features visible in both the baseline and this simulations. Poleward streams of both polarities are also observed, typically with a one-to-one correspondence between the baseline and the simulations.

The biggest discrepancy between the baseline and the simulations appears at the poles, and in the north in particular. First off, the amplitude is too strong, further indicating that the sources are being over-estimated. Secondly, we note that the polar concentrations occur at lower latitudes for Sim 2 and Sim 3 when counter-cells are present in the meridional flow (in the south prior to 2000 and in the north from 2000 to 2010). The fact that this is not observed in the baseline, nor with the HMI data, suggests that these polar counter-cells are not real. The presence of counter-cells in the meridional flow as measured by MDI could be caused by unaccounted for errors in the geometry of the MDI images.

6.3 Discussion

Active region flux versus area is a crucial component to our model, yet this relationship may not be well characterized. Sheeley (1966) and Mosher (1977) found a linear relationship between these parameters; however this was based on very few data points. While Dikpati et al. (2006) agreed with this relationship, this was done by averaging over each rotation and smoothing over 6 rotations. Further investigation of this this relationship using MDI and HMI data may be needed to improve and extend the predictive capability of this flux transport model. Our surface flux transport model that uses active region databases to replicate magnetic field emergence has been shown to accurately predict the polar field evolution for 3-5 years. Improvements to the active region flux versus area relations may extend the predictive capability of the model by years. Remarkably, despite this impairment, the timing of the polar field reversal was accurate to within a year.

Comparison of the magnetic butterfly diagrams showed that polar counter-cells in the meridional flow produce magnetic flux concentrations that are offset in latitude from the poles. In the baseline, however, the flux is concentrated precisely at this poles. This is evidence that the polar

counter-cells observed in the meridional flow measurements are likely merely artifacts. Furthermore, the full magnetic butterfly diagram history (see Figure 1.7) does not contain any offset polar magnetic field concentration. This indicates that the meridional flow has not had any polar counter-cells during this time period, i.e., from 1975 to present.

The presence of poleward streams of leading polarity flux expose the nature of these streams. In the past, these poleward streams have been attributed to variations in Joy's law tilt. However, the current version of the flux transport model uses the average Joy's law tilt (i.e., the angle between the bipolar is equal to one-half of the latitude) without any variations. Since these streams can be reproduced without the scatter in the tilt of bipolar active regions, we propose an alternate explanation.

Normally, new active regions emerge equatorward of the older decaying active regions. This causes the following polarity of the new active regions to emerge at latitudes of the old active region's leading polarity flux. The excess following polarity flux is then transported to the poles forming a following polarity poleward stream, while the new leading polarity flux is left to be canceled by future following polarity emergence. However, if a substantial gap in active region emergence occurs, there would be nothing to cancel with the leading polarity flux. This leading polarity flux would then be transported (after the following polarity flux) to the poles in the form of a leading polarity poleward stream. Additionally, the appearance of an unusually strong bipolar active region may produce a similar effect.

Finally, the simulations presented in this chapter show that the variations in the MF over Cycle 23 have a significant impact (at least $\sim$20%) on the polar fields. The variable meridional flow produced a stronger axial dipole moment than was produced with a constant meridional flow. In addition, the simulations show that the relative importance of the meridional flow variations is not constant - it is highly dependant on the details of the flux transport (e.g., when and where the variations occur). Results showed that during the rise of Solar Cycle 23 (from 1995-2000), changes in the meridional flow had little effect, but a significant effect during the rise of Solar Cycle 24 (from 2010 to the present). Variations in the meridional flow become most important

when less flux is being transported (e.g. in the declining phase of the solar cycle or during a weak solar cycle.) Further investigation is needed to confirm this effect. If it does indeed occur, this may provide a possible feedback mechanism for regulating the solar cycle and possibly recovering from a Maunder-type minimum.

CHAPTER 7

CONCLUSIONS

Characterizing and modeling magnetic flux transport within the surface layers of the Sun is vital to explaining the sunspot cycle. The Sun's polar fields at solar cycle minimum are the seeds of the next solar cycle: weak polar fields produce weak cycles. The polar fields observed during the Cycle 23/24 minimum were significantly weaker (about half) than the polar fields observed during the prior two minima (see Figure 1.9). Solar Cycle 24 is now the weakest solar cycle in at least a hundred years. This has caused speculation that the Sun may be entering a dormant phase like the Maunder Minimum. These unusual solar conditions may provide insight as to how magnetic flux transport regulates the polar field evolution and thus the solar activity cycle.

The primary goals of this dissertation were threefold:

1. Make precise measurements of the Sun's axisymmetric flows (i.e., differential rotation and meridional flow).

2. Create a realistic surface flux transport model that reproduces the magnetic field evolution at the surface by incorporating the observed flows.

3. Investigate the role of flux transport in modulating the polar fields, and thereby the solar activity cycle.

In this Chapter, I will summarize the results that were obtained by achieving of each of these goals.

I began by using a cross-correlation technique on magnetograms to characterize the differential rotation and meridional flow and their variations. MDI data was analyzed from 1996 to 2011. The MDI spatial resolution resolution (1024x1024) limited these measurements to $\pm 75^{\circ}$ in latitude. The results from the MDI data were as follows:

1. A 0.08° error in the measurement of the tilt of the Sun with respect to the ecliptic plane (previously accepted as 7.25°) was found.

2. The measurement of the differential rotation was consistent with previous results. This flow was found to be relatively static.

3. Torsional oscillations were seen when the average flow profile was subtracted from the individual flow profiles.

4. Significant North-South asymmetries were observed in the meridional flow.

5. The meridional flow was found to vary inversely with the solar cycle (i.e., strong flows at minimum and weak flows at maximum).

6. The meridional flow was found to vary from cycle to cycle. Flows of Cycle 24 were found to be $\sim$20% faster than the flows of Cycle 23.

7. Polar counter-cells were observed in the meridional flow profiles.

It has been suggested that the faster meridional flow may have led to weaker polar field strengths and thus the subsequent extended solar minimum and an unusually weak cycle 24.

HMI data was analyzed from 2010 to 2013. Particular attention was given to the period when both MDI and HMI were observing, from April 2010 to March 2011. The better resolution of HMI (4096x4096) extended measurements of the flows to 85°+. While for the most part, HMI results were consistent with the MDI results, a critical difference was found: The polar counter-cells that were observed with MDI were *not* present in the HMI measurements.

In order to investigate the source of the unusually weak polar fields, we have developed a surface flux transport model. This flux transport model advects the magnetic flux emerging in active regions (sunspots) using detailed observations of the near-surface flows that transport the magnetic elements. These flows include the axisymmetric differential rotation and meridional flow and the non-axisymmetric cellular convective flows (supergranules), all of which vary in time in the model as indicated by direct observations. At each time step, magnetic maps of the entire

Sun are created. These maps are used to create plots of the Sun's axial dipole moment, a measure of the polar field.

Our innovative surface flux transport model features several advantages over previous surface flux transport models:

1. This model incorporates a simulation of supergranular motions, rather than a diffusion coefficient to account for the turbulent convective motions of the Sun.

2. This model incorporates the observed meridional flows, whereas previous models have used meridional profiles that do not adequately represent the meridional flow observed on the Sun.

3. In the Sun, the convective flows are affected by the magnetic field strength (i.e., the flows are quenched). While this effect is difficult to account for by the diffusivity coefficient used in prior models, this effect is captured in our model by actually quenching the convective flows where the field is strong.

4. While previous models have added a single source on the day of maximum sunspot group area to represent sunspots, our model slowly adds flux as it emerges rather than in one lump sum.

These advantages make this model the most realistic surface flux transport to date.

Our surface flux transport model can include sources in two ways: by assimilating magnetograms or by simulating emergence using active region databases. The surface flux transport by assimilating magnetograms produces magnetic maps that are nearly identical to other observations. This mode of operation is ideal for creating a baseline dataset. This baseline dataset was used to illustrate the difference between defining the polar field strengths by averaging over polar area or by the axial dipole moment. While the axial dipole moment does not capture hemispheric asymmetries, it was found to be a less arbitrary and less ambiguous metric.

The surface flux transport model was then tested by using active region databases to simulate and predict the evolution of the axial dipole moment. These experiments used constant and North-

South symmetric differential rotation and an antisymmetric meridional flow. The results of these experiments were as follows:

1. We were able to reproduce the Cycle 23/24 minimum with Cycle 23 active regions.
2. We were able to reproduce the Cycle 23/24 minimum with Cycle 17 active regions
3. We were able to reproduce the Cycle 23 reversal with Cycle 17 active regions.
4. We found that the supergranular motions introduces stochastic variations. These variation were small during the Cycle 23/24 minimum, but more pronounced ($\sim$20%) during the reversal.
5. A preliminary prediction of Cycle 24/25 minimum suggests Cycle 25 will be similar to Cycle 24, but these results are very preliminary and a more reliable predictions will come in the next 2-3 years.

These experiments have demonstrated that our surface flux transport model (using active region databases) is viable on short time scales (about five years) using average flow velocities.

In the last set of experiments, we used the surface flux transport model with active region databases on a longer time scale (about 17 years). A constant and North-South symmetric average differential rotation was used in all case. In the first case the constant and North-South antisymmetric average meridional flow was uses, in the second the meridional flow with the observed variations was used, and in the third case the observed variation were amplified. The results of these experiments were:

1. The axial dipole produced by the simulations was about twice as strong as the axial dipole produced in the baseline. This increased amplitude suggests that the active region flux versus sunspot area many be too strong and should be refined.
2. The simulation with the observed variations created polar concentrations offset from the poles. This type of configurations is not supported by observations, indicating that the polar counter-cells found in the MDI data are likely artifacts due to image distortions.

3. Though an average Joy's Law tilt was used consistently, leading polarity poleward streams were still present in the magnetic butterfly diagrams. This suggests that these poleward streams are often products of gaps in active region emergence, rather than variations in Joy's Law.

4. The meridional flow variations did produce at least a 20% impact on the polar fields. However, rather than producing weaker polar fields as expected, these variations produced stronger polar fields.

Despite the larger amplitude polar fields at solar minimum, the simulations produced a Solar Cycle 23/24 polar field reversal that was accurate to within a year. Refining the active region sources may improve the predictive capability of this model (i.e., accurate axial dipole predictions up to 15 years in advance).

As a result of this dissertation, I now believe that the Sun's meridional circulation does *not* include counter-cells at the poles. The fact that I find *stronger* polar fields with the observed, versus the average, meridional flow suggests that the cause of the weak polar fields at the end of Cycle 23 should be attributed to the emergence of fewer active region sources. (Cycle 23 had a peak sunspot number of $\sim$120 - much smaller that Cycle 21 and Cycle 22, which had peaks of $\sim$160. See Figure 1.6.) With fewer sunspots to reverse the strong polar field of Cycle 22, there was insufficient flux remaining to rebuild a strong polar field. The subsequently weak polar fields of the Cycle 23/24 minimum then went on to produce the weak Cycle 24.

The results from this fully advective surface flux transport model also indicate that the evolution of the Sun's surface magnetic field can be faithfully reproduced with a model that does not include free parameters or unknown sources or sinks.

Detailed study of solar and stellar dynamos is still very much in its youth. The results from this dissertation show that we are now beginning to understand the role that surface flux transport plays in these dynamos. However, we are far from having a complete picture. While models, such as the surface flux transport model used here, can help unravel these details, more observations (with which to feed these models) are very much needed. While the Sun provides great detail, it only

represents one dynamo configuration. It is only by combining the detailed observations of the Sun and the statistics provided by observations of activity cycles on other stars, that we may be able to close this gap in our understanding.

BIBLIOGRAPHY

Babcock, H. D. & Livingston, W. C. 1958, Science, 127, 1058

Babcock, H. W. 1953, ApJ, 118, 387

—. 1961, ApJ, 133, 572

Babcock, H. W. & Babcock, H. D. 1952, Publications of the Astronomical Society of the Pacific, 64, 282

Baliunas, S. L., Donahue, R. A., Soon, W. H., Horne, J. H., Frazer, J., Woodard-Eklund, L., Bradford, M., Rao, L. M., Wilson, O. C., Zhang, Q., Bennett, W., Briggs, J., Carroll, S. M., Duncan, D. K., Figueroa, D., Lanning, H. H., Misch, T., Mueller, J., Noyes, R. W., Poppe, D., Porter, A. C., Robinson, C. R., Russell, J., Shelton, J. C., Soyumer, T., Vaughan, A. H., & Whitney, J. H. 1995, ApJ, 438, 269

Basu, S. & Antia, H. M. 2003, ApJ, 585, 553

—. 2010, ApJ, 717, 488

Beck, J. G., Duvall, T. L., & Scherrer, P. H. 1998, Nature, 394, 653

Beck, J. G. & Giles, P. 2005, ApJ, 621, L153

Bullard, E. C. 1949, Royal Society of London Proceedings Series A, 197, 433

Carrington, R. C. 1859, MNRAS, 19, 81

Chandrasekhar, S. 1961, Hydrodynamic and hydromagnetic stability

Charbonneau, P. 2010, Living Reviews in Solar Physics, 7, 3

Choudhuri, A. R., Chatterjee, P., & Jiang, J. 2007, Phys. Rev. Lett., 98, 131103

Cowling, T. G. 1933, MNRAS, 94, 39

de Toma, G. 2011, Sol. Phys., 274, 195

DeVore, C. R., Boris, J. P., & Sheeley, Jr., N. R. 1984, Sol. Phys., 92, 1

Dikpati, M. & Charbonneau, P. 1999, ApJ, 518, 508

Dikpati, M., de Toma, G., & Gilman, P. A. 2006, Geophys. Res. Lett., 33, 5102

Dikpati, M., Gilman, P. A., de Toma, G., & Ulrich, R. K. 2010, Geophys. Res. Lett., 37, 14107

Elsasser, W. M. 1946, Phys. Rev., 69, 106

Ferreira, S. E. S. & Potgieter, M. S. 2004, ApJ, 603, 744

Frazier, E. N. 1970, Sol. Phys., 14, 89

Gilman, P. A. 1979, ApJ, 231, 284

Golub, L. & Pasachoff, J. M. 1997, The Solar Corona

—. 2001, Nearest star : the surprising science of our sun

González Hernández, I., Howe, R., Komm, R., & Hill, F. 2010, ApJ, 713, L16

Hagenaar, H. J., Schrijver, C. J., Title, A. M., & Shine, R. A. 1999, ApJ, 511, 932

Hale, G. E. 1908, ApJ, 28, 315

—. 1913, ApJ, 38, 27

Hale, G. E., Ellerman, F., Nicholson, S. B., & Joy, A. H. 1919, ApJ, 49, 153

Hart, A. B. 1954, MNRAS, 114, 17

Hathaway, D. H. 1996, ApJ, 460, 1027

—. 2010, Living Reviews in Solar Physics, 7, 1

—. 2012a, ApJ, 749, L13

—. 2012b, ApJ, 760, 84

Hathaway, D. H., Beck, J. G., Bogart, R. S., Bachmann, K. T., Khatri, G., Petitto, J. M., Han, S., & Raymond, J. 2000, Sol. Phys., 193, 299

Hathaway, D. H., Gilman, P. A., Harvey, J. W., Hill, F., Howard, R. F., Jones, H. P., Kasher, J. C., Leibacher, J. W., Pintar, J. A., & Simon, G. W. 1996, Science, 272, 1306

Hathaway, D. H. & Rightmire, L. 2010, Science, 327, 1350

—. 2011, ApJ, 729, 80

Hathaway, D. H., Upton, L., & Colegrove, O. 2013, Science, 342, 1217

Hathaway, D. H., Williams, P. E., Dela Rosa, K., & Cuntz, M. 2010, ApJ, 725, 1082

Hathaway, D. H. & Wilson, R. M. 1990, ApJ, 357, 271

Howard, R., Boyden, J. E., & Labonte, B. J. 1980, Sol. Phys., 66, 167

Howard, R. & Gilman, P. A. 1986, ApJ, 307, 389

Howard, R., Gilman, P. I., & Gilman, P. A. 1984, ApJ, 283, 373

Howard, R. & Labonte, B. J. 1980, ApJ, 239, L33

Howard, R. F. 1991, Sol. Phys., 132, 49

Howe, R., Christensen-Dalsgaard, J., Hill, F., Komm, R., Schou, J., & Thompson, M. J. 2009, ApJ, 701, L87

Howe, R., Christensen-Dalsgaard, J., Hill, F., Komm, R. W., Larsen, R. M., Schou, J., Thompson, M. J., & Toomre, J. 2000, ApJ, 533, L163

Hoyt, D. V. & Schatten, K. H. 1992, The Astrophysical Journal Supplement Series, 78, 301

Jin, C. L., Harvey, J. W., & Pietarila, A. 2013, ApJ, 765, 79

Komm, R. W., Howard, R. F., & Harvey, J. W. 1993a, Sol. Phys., 147, 207

—. 1993b, Sol. Phys., 145, 1

Korzennik, S. G., Rabello-Soares, M. C., & Schou, J. 2004, ApJ, 602, 481

Kutner, M. L. 2003, Astronomy: A Physical Perspective

Larmor, J. 1919, Rep. Brit. Assoc. Adv. Sci., 159

Latushko, S. 1994, Sol. Phys., 149, 231

Lean, J. L. & Rind, D. H. 2008, Geophys. Res. Lett., 35, 18701

Leighton, R. B. 1964, ApJ, 140, 1547

Leighton, R. B., Noyes, R. W., & Simon, G. W. 1962, ApJ, 135, 474

Liu, Y., Hoeksema, J. T., Scherrer, P. H., Schou, J., Couvidat, S., Bush, R. I., Duvall, T. L., Hayashi, K., Sun, X., & Zhao, X. 2012, Sol. Phys., 279, 295

Meunier, N. 1999, ApJ, 527, 967

Mosher, J. M. 1977, PhD thesis, California Institute of Technology, Pasadena.

Muñoz-Jaramillo, A., Balmaceda, L. A., & DeLuca, E. E. 2013, Physical Review Letters, 111, 041106

Muñoz-Jaramillo, A., Sheeley, N. R., Zhang, J., & DeLuca, E. E. 2012, ApJ, 753, 146

Newton, H. W. & Nunn, M. L. 1951, MNRAS, 111, 413

Norton, A. A. & Gallagher, J. C. 2010, Sol. Phys., 261, 193

Parker, E. N. 1955, ApJ, 122, 293

Phillips, K. J. H. 1992, Guide to the sun

Prialnik, D. 2009, An Introduction to the Theory of Stellar Structure and Evolution

Rightmire-Upton, L., Hathaway, D. H., & Kosak, K. 2012, ApJ, 761, L14

Roudier, T., Rieutord, M., Brito, D., Rincon, F., Malherbe, J. M., Meunier, N., Berger, T., & Frank, Z. 2009, A&A, 495, 945

Scherrer, P. H., Bogart, R. S., Bush, R. I., Hoeksema, J. T., Kosovichev, A. G., Schou, J., Rosenberg, W., Springer, L., Tarbell, T. D., Title, A., Wolfson, C. J., Zayer, I., & MDI Engineering Team. 1995, Sol. Phys., 162, 129

Scherrer, P. H., Schou, J., Bush, R. I., Kosovichev, A. G., Bogart, R. S., Hoeksema, J. T., Liu, Y., Duvall, T. L., Zhao, J., Title, A. M., Schrijver, C. J., Tarbell, T. D., & Tomczyk, S. 2012, Sol. Phys., 275, 207

Schou, J., Antia, H. M., Basu, S., Bogart, R. S., Bush, R. I., Chitre, S. M., Christensen-Dalsgaard, J., di Mauro, M. P., Dziembowski, W. A., Eff-Darwich, A., Gough, D. O., Haber, D. A., Hoeksema, J. T., Howe, R., Korzennik, S. G., Kosovichev, A. G., Larsen, R. M., Pijpers, F. P., Scherrer, P. H., Sekii, T., Tarbell, T. D., Title, A. M., Thompson, M. J., & Toomre, J. 1998, ApJ, 505, 390

Schou, J. & Bogart, R. S. 1998, ApJ, 504, L131

Schrijver, C. J. & Title, A. M. 2001, ApJ, 551, 1099

Schwarzschild, K. 1906, Nachrichten von der Königlichen Gesellschaft der Wissenschaften zu Göttingen. Math.-phys. Klasse, 195, p. 41-53, 195, 41

Sheeley, Jr., N. R. 1966, ApJ, 144, 723

Sheeley, Jr., N. R., DeVore, C. R., & Boris, J. P. 1985, Sol. Phys., 98, 219

Shiota, D., Tsuneta, S., Shimojo, M., Sako, N., Orozco Suárez, D., & Ishikawa, R. 2012, ApJ, 753, 157

Simon, G. W. & Leighton, R. B. 1964, ApJ, 140, 1120

Simon, G. W., Title, A. M., Topka, K. P., Tarbell, T. D., Shine, R. A., Ferguson, S. H., Zirin, H., & SOUP Team. 1988, ApJ, 327, 964

Simon, G. W. & Weiss, N. O. 1968, Zeitschrift fur Astrophysik, 69, 435

Skumanich, A. 1972, ApJ, 171, 565

Snodgrass, H. B. 1983, ApJ, 270, 288

—. 1984, Sol. Phys., 94, 13

Snodgrass, H. B. & Dailey, S. B. 1996, Sol. Phys., 163, 21

Spruit, H. C. 1979, Sol. Phys., 61, 363

—. 2003, Sol. Phys., 213, 1

Stenflo, J. O. 1973, Sol. Phys., 32, 41

Svalgaard, L., Cliver, E. W., & Kamide, Y. 2005, Geophys. Res. Lett., 32, 1104

Svalgaard, L., Duvall, Jr., T. L., & Scherrer, P. H. 1978, Sol. Phys., 58, 225

Svalgaard, L. & Kamide, Y. 2013, ApJ, 763, 23

Thompson, M. J., Toomre, J., Anderson, E. R., Antia, H. M., Berthomieu, G., Burtonclay, D., Chitre, S. M., Christensen-Dalsgaard, J., Corbard, T., De Rosa, M., Genovese, C. R., Gough, D. O., Haber, D. A., Harvey, J. W., Hill, F., Howe, R., Korzennik, S. G., Kosovichev, A. G., Leibacher, J. W., Pijpers, F. P., Provost, J., Rhodes, Jr., E. J., Schou, J., Sekii, T., Stark, P. B., & Wilson, P. R. 1996, Science, 272, 1300

Topka, K., Moore, R., Labonte, B. J., & Howard, R. 1982, Sol. Phys., 79, 231

Tuominen, J. & Kyrolainen, J. 1982, Sol. Phys., 79, 161

Ulrich, R. K. 1970, ApJ, 162, 993

—. 2010, ApJ, 725, 658

Ulrich, R. K., Boyden, J. E., Webster, L., Padilla, S. P., & Snodgrass, H. B. 1988, Sol. Phys., 117, 291

Ulrich, R. K. & Tran, T. 2013, ApJ, 768, 189

Upton, L. & Hathaway, D. H. 2014, ApJ, 780, 5

van Ballegooijen, A. A., Cartledge, N. P., & Priest, E. R. 1998, ApJ, 501, 866

Vandenbussche, F. C. 1999, ESA Bulletin, 97, 39

Vögler, A., Shelyag, S., Schüssler, M., Cattaneo, F., Emonet, T., & Linde, T. 2005, A&A, 429, 335

Wang, Y.-M., Nash, A. G., & Sheeley, Jr., N. R. 1989, ApJ, 347, 529

Wang, Y.-M., Robbrecht, E., & Sheeley, Jr., N. R. 2009, ApJ, 707, 1372

Wilson, O. C. 1978, ApJ, 226, 379

Zhao, J., Bogart, R. S., Kosovichev, A. G., Duvall, Jr., T. L., & Hartlep, T. 2013, ApJ, 774, L29

Zhao, J., Nagashima, K., Bogart, R. S., Kosovichev, A. G., & Duvall, Jr., T. L. 2012, ApJ, 749, L5